$2(P)$

PRINCETON UNIVERSITY

DEPARTMENT OF
AEROSPACE AND MECHANICAL SCIENCES

SPECTROSCOPIC STUDIES OF THE EXHAUST PLUME OF A QUASI-STEADY MPD ACCELERATOR

A. P. Bruckner and R. G. Jahn

Report 1041*

Prepared by _____
Adam P. Bruckner

Approved by _____
R. G. Jahn
Dean, School of Engineering

*This report is a reproduction in entirety of the Ph.D. dissertation of Mr. Adam P. Bruckner. It is submitted to the sponsor and to the distribution list in this form both as a presentation of the technical material, and as an indication of the academic program supported by this Grant.

May 1972

School of Engineering and Applied Science
Department of Aerospace and Mechanical Sciences
Guggenheim Aerospace Propulsion Laboratories
PRINCETON UNIVERSITY
Princeton, New Jersey

ABSTRACT

Spectroscopic and photographic investigations reveal
a complex azimuthal species structure in the exhaust plume
of a quasi-steady argon MPD accelerator. Over a wide range
of operating conditions the injected argon remains col-
limated in discrete jets which are azimuthally in line with
the six propellant injector orifices. The regions between
these argon jets, including the central core of the exhaust
flow, are occupied by impurities such as carbon, hydrogen
and oxygen ablated from the Plexiglas back plate of the arc
chamber. The features of this plume structure are found
to be dependent on the arc current and mass flow rate. Time-
resolved spectroscopic velocity measurements, obtained by
a scanning Fabry-Perot spectrometer system at a current of
16 kA and a mass flow of 6 g/sec indicate argon ion jet
velocities of 16,500 m/sec, which considerably exceeds the
Alfvén critical speed of argon. It is found that nearly
half the observed velocity is attained in an acceleration
region well downstream of the region of significant electro-
magnetic interaction. Temperature measurements suggest that
simple gasdynamic expansion processes in the argon jets can-
not fully explain the observed acceleration. Recombination
calculations show that the ionization energy is essentially
frozen. It is possible that a transfer of momentum from
the core flow of ablation products to the argon jets may
contribute to the high argon velocities.

TABLE OF CONTENTS

LIST OF ILLUSTRATIONS

LIST OF ILLUSTRATIONS (Cont'd)

LIST OF ILLUSTRATIONS (Cont'd)

CHAPTER 1

INTRODUCTION

Electromagnetic plasma accelerators have received con-
siderable attention in recent years as potential candidates
for prime propulsion on advanced deep space missions.[1-4]
The advantage of this class of thrusters over other elec-
tric propulsion devices, such as electrostatic ion engines
or thermal arc jets, lies in their ability to combine high
levels of thrust density ($\approx 10^4$ N/m^2) with very attractive
levels of specific impulse (2-5 x 10^3 sec).

Of particular promise is the magnetoplasmadynamic (MPD)
accelerator in which arc currents typically greater than
10^{3}A interact with their self-induced magnetic fields to
exert intense body forces on an injected propellant
stream.[1-4] A typical MPD accelerator is shown in
schematic form in Fig. 1-1. Under suitable conditions current
flows between the conical cathode and the coaxial anode in
a diffuse axisymmetric arc. The interaction of the radial
component of arc current with the self-induced azimuthal
magnetic field produces an axial acceleration, which results
in a "blowing" component of thrust. The axial component of
the arc current interacts with the magnetic field to produce
a radial gradient in the plasma pressure which provides a re-
action force on the cathode surface, giving rise to a "pumping"
component of thrust. An electrothermal thrust contribution
also exists, resulting from the unbalanced gasdynamic pressure
of the resistively heated plasma on the chamber walls.

Operation of the arc at the highest possible current
levels is encouraged by the dependence of the electromagnetic
thrust on the square of the discharge current.[1] However,
electrode heat transfer problems limit steady-state operation
to a maximum of about 3 x 10^{3}A. These limitations can be cir-
cumvented by operating the arc in the so-called quasi-steady

FIGURE 1-1
AP25·4736

2
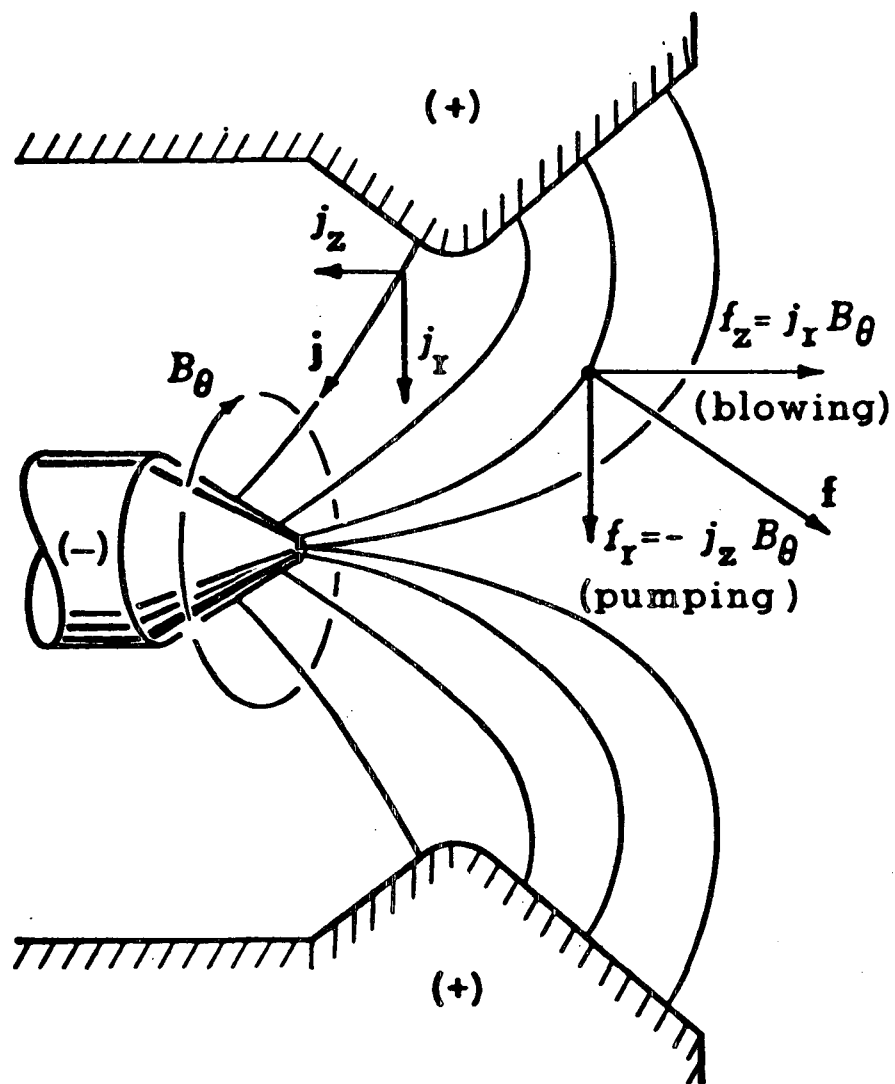
mode[4,5] in which the electrical power is supplied in the
form of repetitive high current pulses of sufficient dura-
tion that steady acceleration processes prevail over most
of each pulse, but which are short enough that the inte-
grated heat load to the electrodes is tolerable.

Quasi-steady operation offers additional advantages.
For example, the MPD operation can be extended to multi-
megawatt power levels which are completely inaccessible
to steady-state accelerators and power supplies. Such high
power operation is of basic interest because it has been
observed that the overall efficiency of the thruster im-
proves as the power level is increased.[4,6] This mode
of operation also greatly facilitates laboratory study of
MPD accelerators. The high currents permit the arc cham-
ber dimensions to be scaled up while maintaining the arc
intensity in the larger volume, thus considerably easing
interior access. At the same time, the short duration of
each current pulse limits energy transfer to modest levels,
even at the higher discharge powers involved, allowing
small uncooled diagnostic probes to survive the hostile en-
vironment in the arc chamber and exhaust plume, and thus
making possible the difficult task of mapping in detail
the various plasmadynamic properties over the full interior
of the discharge.

Recent experimental investigations of the discharge
region and exhaust plume of quasi-steady MPD accelerators
have contributed significantly to the understanding of the
complex physical processes occurring in this class of thrus-
ters. Clark,[4,5] Oberth[6,7] and Turchi[8,9] have measured
the detailed structure of the electric and magnetic fields
in the acceleration region of the MPD arc at Princeton, and
established the nature of the current conduction patterns,
plasma potential profiles and electrode losses. On the same
device Cory[10] has successfully measured exhaust momentum
flux profiles and chamber pressures, and has determined the

magnitudes of the electromagnetic and electrothermal components of total thrust. Working with a parallel-plate self-field accelerator which retains the essential features of the coaxial MPD thruster without flow expansion downstream of the acceleration region, Di Capua[13] has studied the ratio of energy deposition into kinetic and thermal modes and has established that the discharge imparts more energy to the flow by resistive heating than by direct body force acceleration. His results suggest that electrothermal conversion via the downstream expansion permitted by the coaxial geometry of conventional MPD arcs may play a significant role in the acceleration process.

One of the most important indicators of the nature of the acceleration mechanisms and of the overall thruster performance is the exhaust velocity pattern. Consequently much effort has been applied to its measurement.[2,11-13,30] Malliaris et al[12,30] have measured exhaust velocities by spectroscopic techniques and have examined the effects of arc current and propellant mass flow on the specific impulse of an MPD accelerator similar to the one investigated here. The results are instructive but contradictory. In the earlier work[12] argon exhaust velocities of about 1.8×10^4 m/sec are reported, with the arc operating in the so-called "matched" condition. The more recent studies,[30] on the other hand, indicate a limiting exhaust velocity equal to the so-called Alfvén critical speed[2,12,30] — 8.7×10^3 m/sec for argon — which has been proposed by some as a fundamental limit for MPD accelerators. Using electrostatic time-of-flight probes Jahn and Clark,[11] have observed an exhaust velocity of the order of 2.5×10^4 m/sec, which substantially exceeds both the Alfvén critical speed of argon and that computed from the electromagnetic thrust relation.[1] A potential shortcoming of the time-of-flight method, however, is that it may not record the true streaming flow velocity because it cannot distinguish between convective and wave velocity components. If wave propagation

components are superimposed on the true convective veloc-
ity of the flow, the time-of-flight technique will record
the combined streaming and wave velocities. For the par-
ticular environment downstream of the accelerator, where
the magnetic fields are small, the only relevant wave
system would be the ion-acoustic mode, an electrostatical-
ly coupled longitudinal oscillation which propagates dis-
turbances at a hybrid velocity determined by both ion and
electron temperatures.[14] In some regions of the ex-
haust, where temperatures of the order of 2 eV may exist,
the wave speed may be commensurate with the true streaming
velocity, leading to serious overestimates by the time-of-
flight method.

These problems, and the lack of general agreement on
the exhaust velocities produced by MPD accelerators opera-
ted on argon, clearly point out the urgent need to carry
out accurate and definitive measurements of velocity by
means of a technique which neither disturbs the flow nor
is affected by possible wave propagation phenomena. It
is the primary purpose of this dissertation to contribute
to this task.

To measure the pure streaming velocity components in
the MPD exhaust it is possible to use spectroscopic Doppler-
shift techniques. Accordingly, a sophisticated scanning
Fabry-Perot spectrometer system has been developed, capable
of recording spectral line shifts and widths on a time scale
more than an order of magnitude shorter than the length of the
discharge current pulse. Although this system affords time-
resolved measurements of both velocity and temperature, with-
out disturbing the exhaust flow or being subject to wave propa-
gation effects, it, like any optical technique which relies
on the self-luminosity of the working medium, is unable to
provide direct local measurements. This is because observed
line profiles and shifts result from the integrated effect
of all emitters along the line of sight and are consequently

distorted by spatial distributions of emitter number density, temperature and velocity. However, if the exhaust plume is azimuthally uniform, local values of velocity and temperature can in principle be obtained by the application of suitable mathematical unfolding procedures.[16]

Previous diagnostic measurements of magnetic fields, potential profiles, and impact pressure profiles[4-10] have indicated a complete cylindrical symmetry of these parameters, and consequently it has been generally assumed that the discharge radiance profiles are azimuthally uniform also.[4-10,15] However, early experiments with the new Fabry-Perot spectrometer suggested otherwise,[17] indicating the existence of a complex but regular azimuthal and radial structure in the distribution of the argon propellant in the exhaust. The serious implications of this apparent lack of azimuthal uniformity immediately motivated a thorough photographic and spectroscopic investigation of the nature and origins of the species structure of the exhaust plume of the MPD accelerator. The results of this study, which has brought to light a number of important new features of arc behaviour, are reported in Chapter 3 of this dissertation.

The bulk of the present work is devoted to the measurement of the exhaust velocities and temperatures of singly ionized argon, the dominant spectroscopic specie of the propellant,[15] and to the interpretation of the results. The experimental measurements are described in detail in Chapter 4, while the various acceleration processes which may be responsible for the observed velocities are discussed in Chapter 5. Appendices covering ablation phenomena in the discharge chamber and reviewing the principles of the Fabry-Perot spectrometer are included at the end of the dissertation. The new information gained in the investigations described here is significant, providing not only an increased understanding of MPD arc processes but also establishing important new criteria in the search for optimum thruster design.

CHAPTER 2

THE MPD ACCELERATOR FACILITY

2-1 INTRODUCTION

The quasi-steady MPD accelerator facility used in the
present investigation is composed of an arc chamber, a mass
injection system, a power source, a gas-triggered discharge
switch, and a large dielectric vacuum tank. A schematic of
the entire system is shown in Fig. 2-1. In this chapter
each component is briefly described. Additional details
are available in the references.[4,13,15,18]

2-2 THE ARC CHAMBER

The 12.7 cm diam x 5.1 cm deep cylindrical arc chamber,
shown in Figs. 2-1 and 2-2, has a conical tungsten cathode
1.9 cm diam x 2.1 cm long and an aluminum anode with a 10.2
cm diam exhaust orifice. The inner walls of the chamber
consist of a Pyrex glass insulator ring and a Plexiglas end-
plate. Argon propellant enters the chamber at the end wall
through six nylon injector tubes which are arranged in a
hexagonal pattern at a radius of 2.54 cm and extend 6 mm
axially beyond the Plexiglas end wall. The choice of plas-
tics for the injectors and the end wall is based on their
ease of fabrication, excellent electrical insulation proper-
ties, and low initial cost.

2-3 THE MASS INJECTION SYSTEM

The propellant mass injection system used in the
present investigation is one based on valve control, which
allows operation of the accelerator over a wide range of
mass flow rates.[18] The gas-handling system is shown in
Fig. 2-1. Fast-acting solenoid valves driven by voltages up
to 10 times their rated values feed propellant gas pulses to

CAPACITOR LINE

GAS SWITCH

HIGH PRESSURE GAS

VALVE

(+)

(−)

ANODE

PLEXIGLAS END PLATE

HIGH PRESSURE GAS

VALVE

CATHODE

INJECTORS

PYREX CHAMBER WALL

POWER SUPPLY

ARC CHAMBER

PLEXIGLAS VACUUM TANK
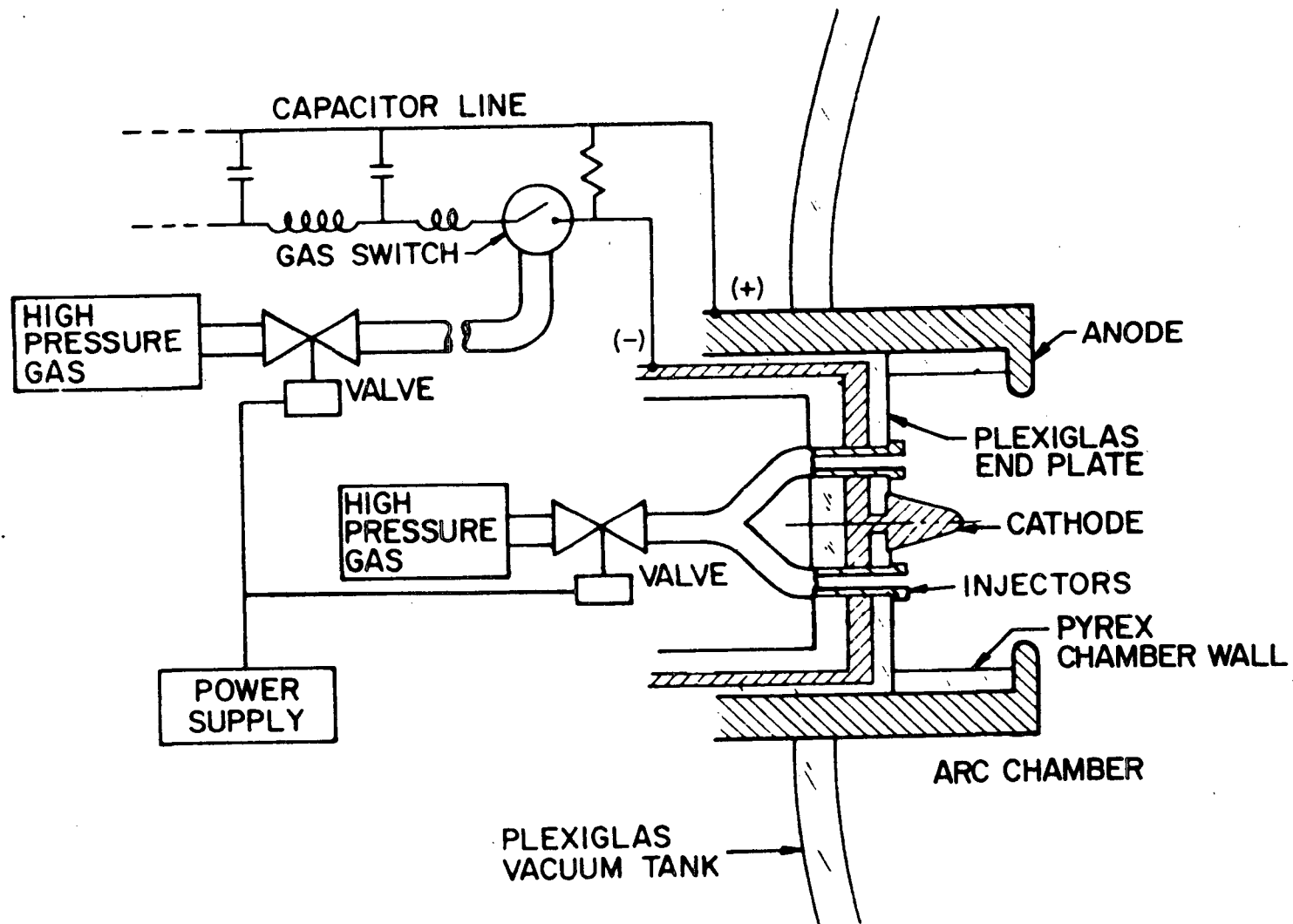
ACCELERATOR SCHEMATIC

FIGURE 2-1
AP 25 R 4681 71

8
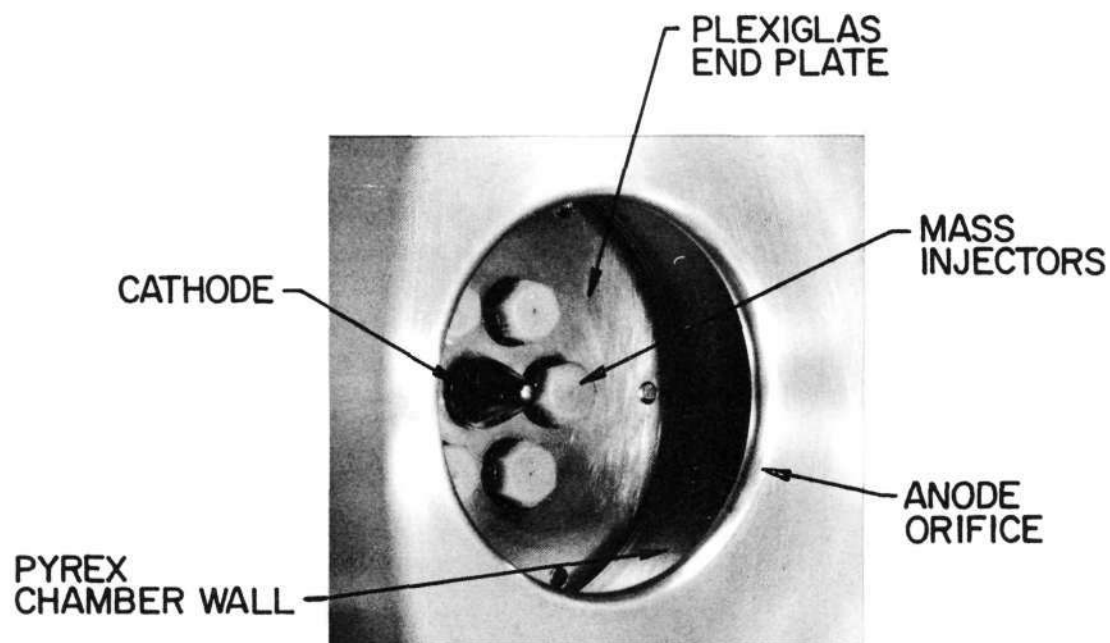
PERSPECTIVE VIEW OF ARC CHAMBER

FIGURE 2-2

AP25·P·458

the arc chamber and the discharge switch. Mass flow is controlled by the propellant reservoir pressure and by calibrated orifices in the valves. For a given orifice the propellant feed rate can be varied over nearly an order of magnitude. The gas pulse to the switch is delayed through a tube whose length is adjusted to synchronize switch breakdown with the achievement of steady cold gas flow in the arc chamber.

2-4 THE POWER SOURCE

The 160 kilojoule power source, which provides a nearly square nonreversing current pulse to the arc, consists of an L-C ladder network of 3300 μfd total capacity deployed in 120 stations.[13] (Fig. 2-3) These are assembled in four lines of 30 identical sections, which can be cross-connected in various series-parallel combinations. For example, the full series connection can drive currents up to 26 kA through a matched load for 1 msec at a maximum charge voltage of 8 kV while the full parallel connection of the four lines can provide 100 kA for 0.25 msec.

Each capacitor is nested in a plywood pigeonhole in the structural frame, which also serves to protect adjacent units in case of a capacitor failure. One of the capacitor terminals is connected directly to ground, and the other to the inductor via a 10 cm length of #16 AWG tinned copper wire enclosed in a small bore nylon tube which serves as a fuse for that section. Each inductor is a three-turn portion of a continuous solenoid, 10 cm I.D. x 6.4 cm pitch, wound from a 3.8 cm x 0.32 cm copper strip.

The network is matched to the arc load by an appropriate ballast resistor connected in series with the accelerator. To accommodate the large energy dissipation this resistor is actually an electrolytic cell, consisting of copper plates immersed in a cupric sulfate solution.

CABLE CONNECTIONS

POWER SUPPLY

BALLAST RESISTORS

BLEEDER RESISTOR

30 SECTION "LC LADDER" NETWORK

FIGURE 2-3
AP25 P 419
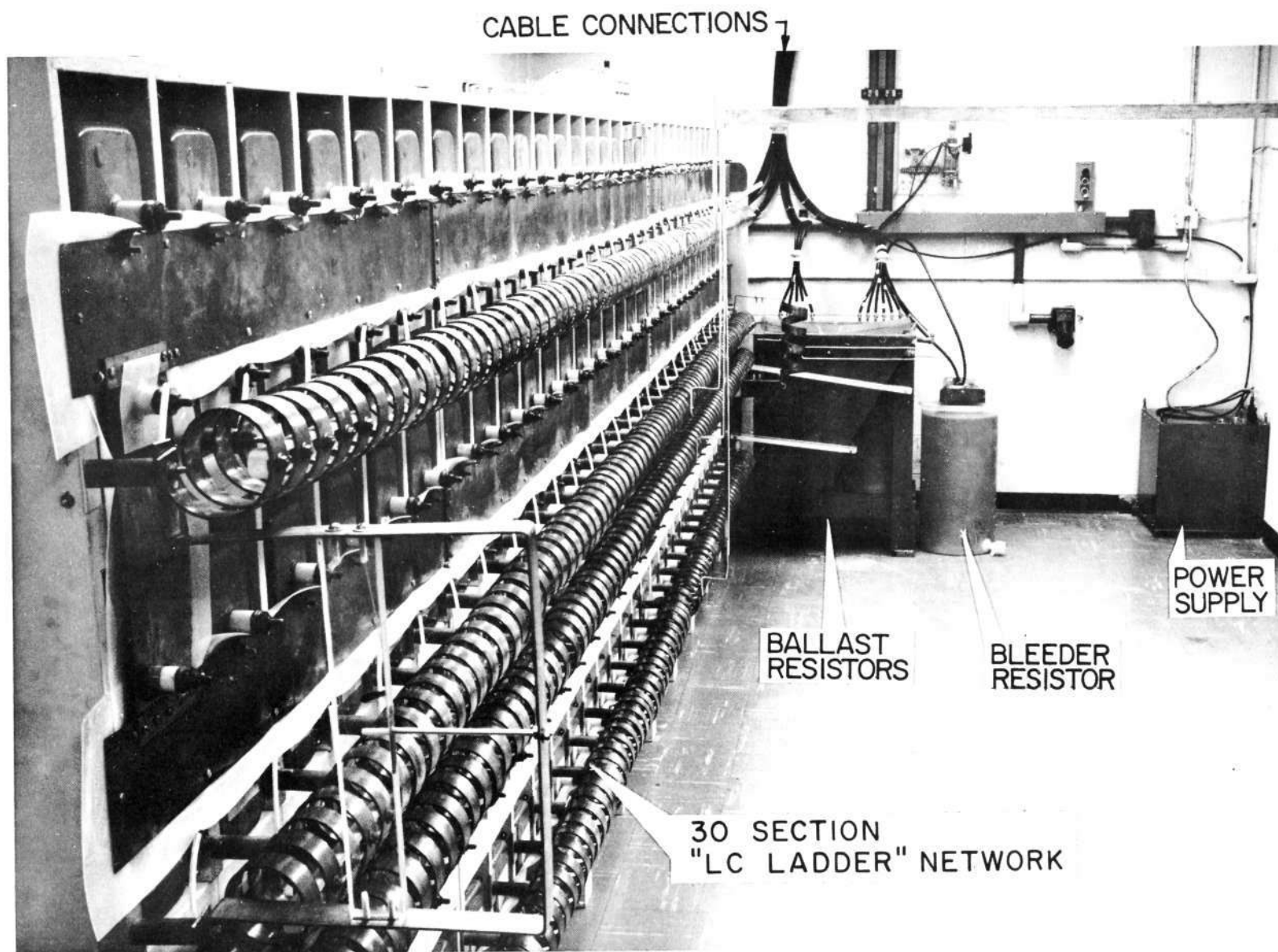
VIEW OF POWER SOURCE

Each of the four network segments can be equipped with its own electrolytic resistor, all four of which are needed to match the full parallel line configuration. A typical current waveform delivered by the power source in full series configuration, charged to 4 kV, is shown in Fig. 2-6a.

2-5   THE GAS-TRIGGERED SWITCH

The power source is connected to the accelerator through a gas-triggered discharge switch,[19] shown schematically in Fig. 2-4. It consists essentially of a pair of 13.8 cm diam stainless steel disk electrodes separated by a Plexiglas insulator ring 12.5 cm I.D. x 5.1 cm long. In operation the switch is evacuated and the electrode gap sustains the full bank voltage until a gas pulse is introduced through the central manifold. When the pressure reaches the Paschen limit at the applied voltage, the switch breaks down, closing the circuit to the arc chamber. The pressure developed in the switch during the current pulse is relieved by an outlet to an evacuated dump tank.

2-6   THE VACUUM FACILITY

The accelerator proper is mounted at one end of a 92 cm I.D. x 183 cm long Plexiglas vacuum tank, shown in Fig. 2-5.[20] The dielectric nature of this vessel precludes perturbation of the exhaust plume by currents which might otherwise flow from it to metallic tank walls. The tank is equipped with nine 15.2 cm diam access windows which can be used for optical diagnostic experiments, and with an internal adjustable platform which can support a variety of diagnostic probes. A 10^{-5} torr background pressure environment is maintained by a 15.2 cm oil diffusion pump backed by two mechanical pumps.

2-7   TYPICAL ARC CHARACTERISTICS

Figure 2-6a displays typical voltage and current characteristics of the arc for a 16 kA x 1 msec current pulse and

TO ACCELERATOR

RETURN CONDUCTOR

FROM POWER SOURCE

ELECTRODES (STAINLESS STEEL)

GAS INLET

TO DUMP TANK AND VACUUM PUMP

INSULATOR (PLEXIGLAS)

COAXIAL CABLE
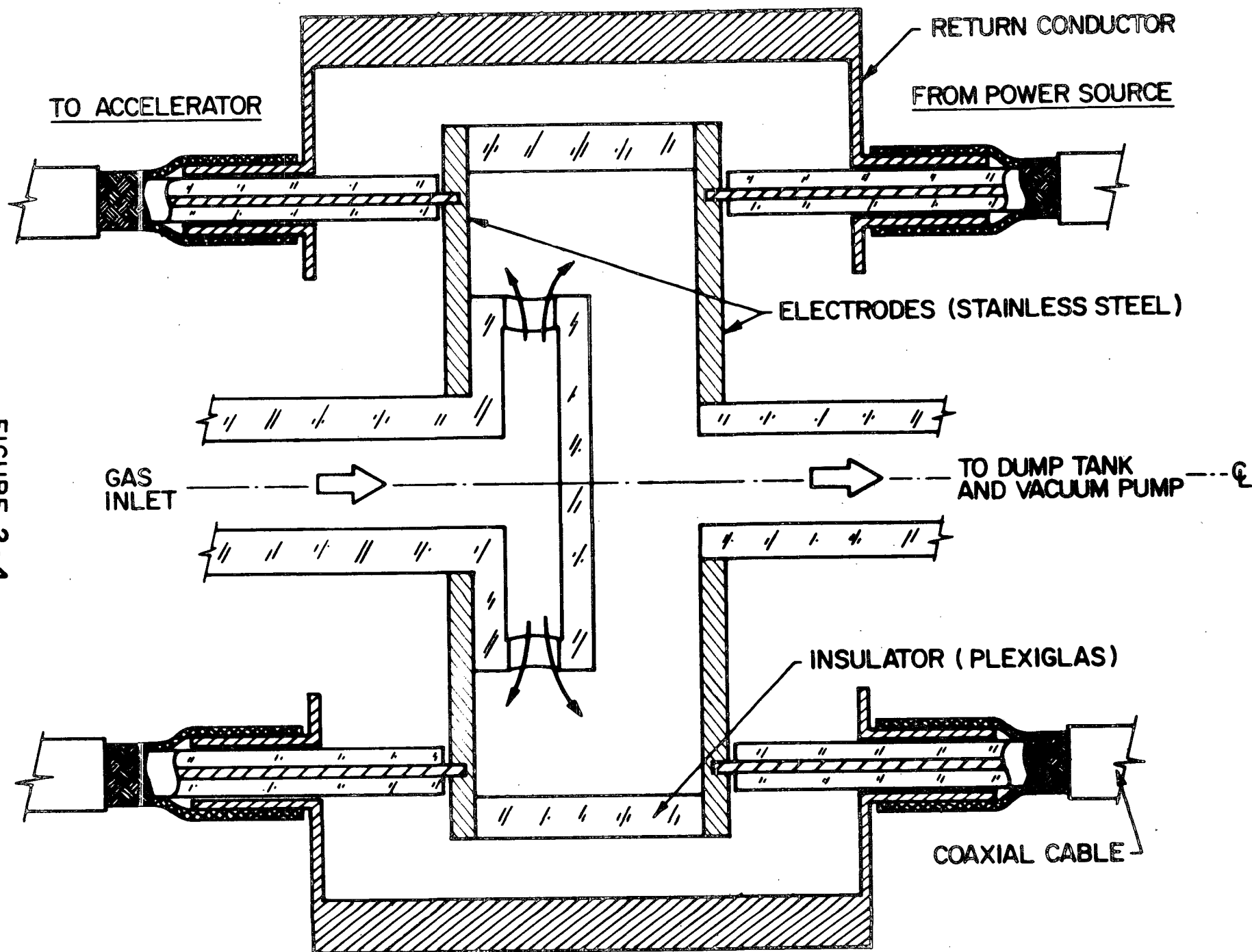
FIGURE 2-4
AP25 4770

SCHEMATIC OF SWITCH

13

FIGURE 2-5
AP 25·P·459

14
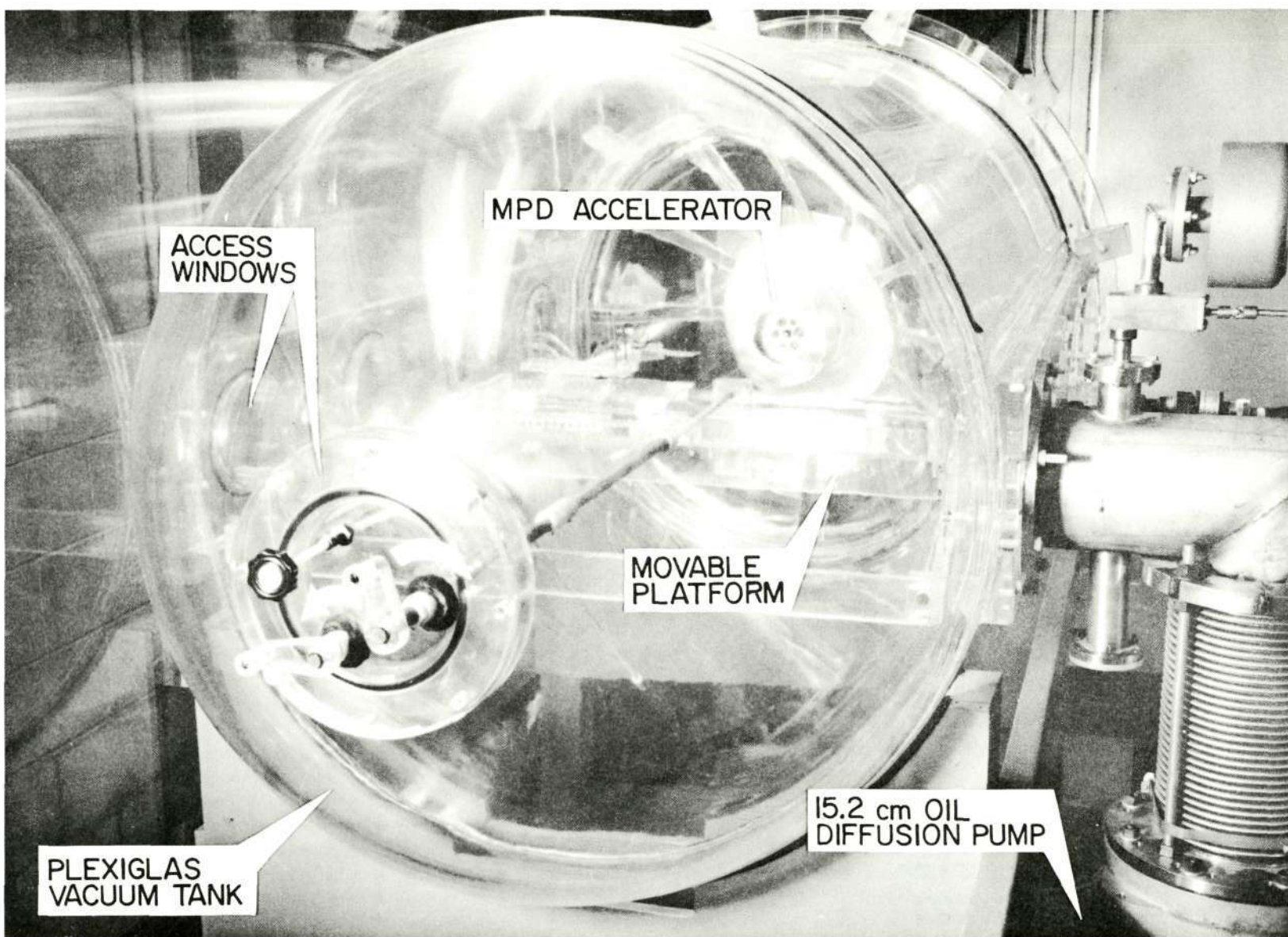
VACUUM SYSTEM CONTAINING MPD ACCELERATOR

I 7474 b

VOLTAGE 170 V

CURRENT 16 kA

→| |←200 μsec/DIV
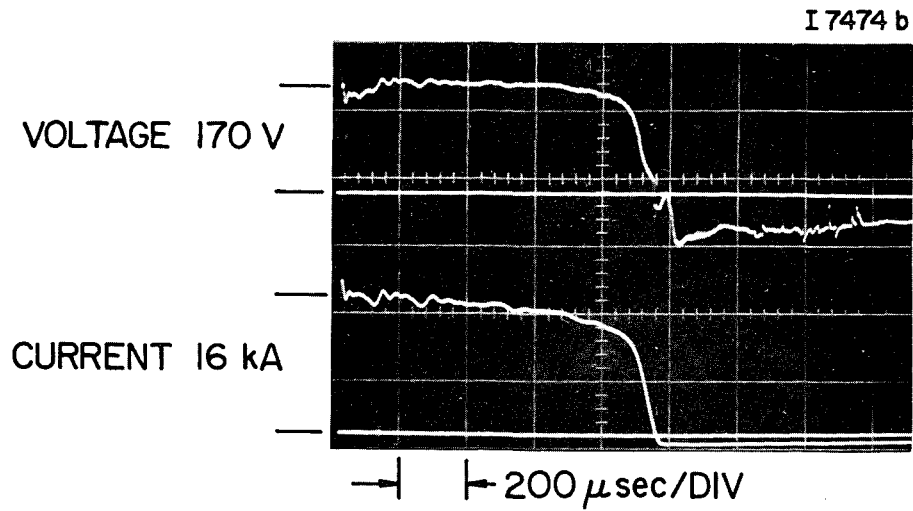
a) VOLTAGE AND CURRENT SIGNATURES

(+)

$\frac{J}{J_{TOT}} = .05$

.75 .50 .25 .10

(−)
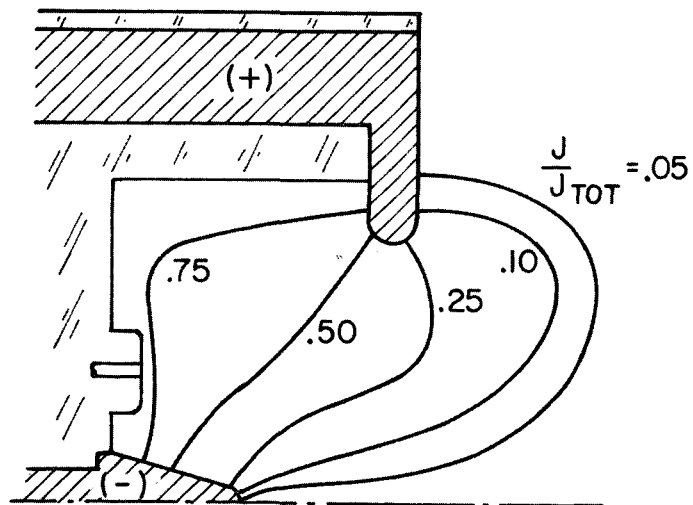
b) ENCLOSED CURRENT CONTOURS

MPD DISCHARGE CHARACTERISTICS
J = 16 kA , ṁ = 6 g/sec

FIGURE 2-6
AP25·P·460

an argon mass flow of 6 g/sec. After an initial transient
of about 150 μsec the arc voltage reaches a steady-state
value of 170V, which it maintains until the current ceases.
Figure 2-6b displays the quasi-steady current distribution
at these operating conditions, in the form of enclosed cur-
rent contours plotted on a cross section of the arc chamber.
These contours, which represent the fraction of the total
arc current lying downstream of a given location, were de-
rived from time integrated magnetic probe signals through-
out the arc chamber.[4,5] The current distribution, as well
as floating potential profiles[6,7] and impact pressure
profiles[10] show no evidence of current spoking, and ap-
pear to be azimuthally uniform.

CHAPTER 3

SPECIES STRUCTURE OF THE EXHAUST

3-1 INTRODUCTION

One of the most widely used diagnostic tools in the study of MPD thrusters has been the visual or photographic observation of the exhaust plume.[2,4,8,15] This is not surprising since virtually all types of MPD arcs display striking patterns of intense visible luminosity in their arc chambers and exhaust plumes. Depending on the propellant material and flow rate, the prevailing magnetic field pattern, and the arc power level, a variety of regions of characteristic colors and dimensions are usually found to appear with rather sharp definition. Studies of these luminous features have played an important role in the development of theoretical models of certain types of MPD arcs.[2,8]

The quasi-steady MPD discharges under investigation here have been extensively photographed with a Kerr-cell camera and the observed luminous patterns reported in considerable detail.[8,15] Figure 3-1 displays a Kerr-cell photograph[8] of the chamber interior at 150 μsec into the current pulse, by which time the discharge has achieved full quasi-steady operation. A portion of the arc chamber side wall is removed, as shown in Fig. 3-1a, allowing the entire discharge region to be viewed through the glass insulator. The shutter remains open for 5 μsec. Color slides corresponding to the black and white photograph shown here reveal several interesting luminous features: 1) a bright green layer apparently covering the gas injector ports and most of the surface of the Plexiglas insulator, extending about one cathode length into the arc chamber; 2) an intense blue-white conical region between the cathode and the anode, with a sharp upstream leading edge and two horizontal dark reddish
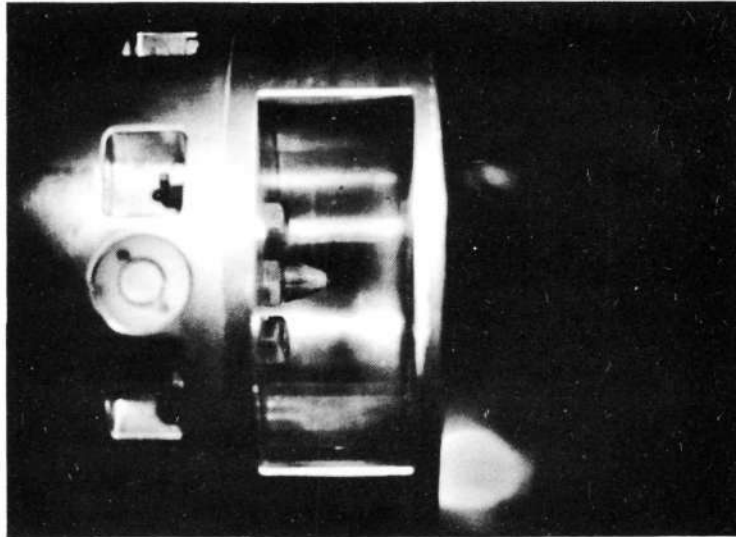
a) ARC CHAMBER THROUGH SIDEWALL WINDOW
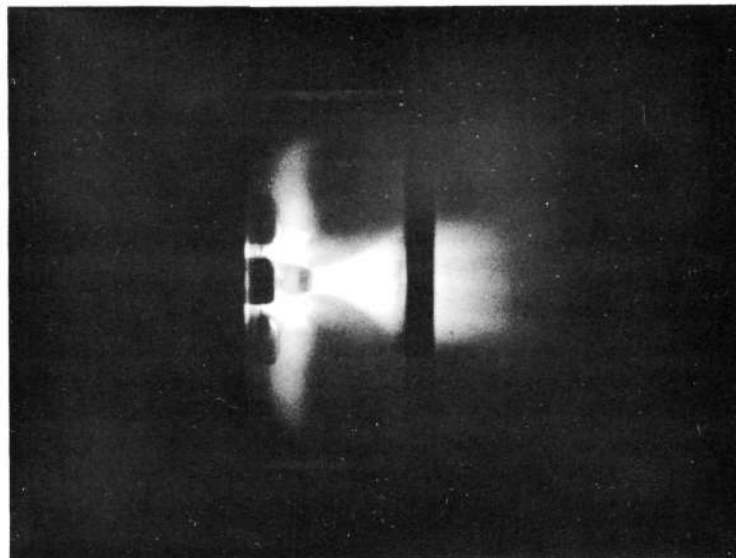
b) QUASI-STEADY OPERATION, $t = 150\ \mu$ sec
   $J = 16\,kA$, $\dot{m} = 6\ g/sec$

VIEW OF DISCHARGE INSIDE ARC CHAMBER

FIGURE 3-1
AP25·P·461

bands; and 3) a predominantly bluish plume downstream of the anode, exhibiting an interesting radial structure of three blue "jets" separated by two dark reddish bands which are extensions of the ones in the conical region.

Based on the azimuthal uniformity of current,[4,5] potential[6,7] and impact pressure profiles[10] it has generally been assumed that the luminous patterns are also azimuthally uniform.[4,5,8,9,15] However, close inspection of color photographs of the discharge makes it apparent that the striated structure of the luminous cone and exhaust plume cannot be produced by any reasonable cylindrically symmetric distribution of gas emissivities. This seeming lack of cylindrical uniformity has profound implications for the spectroscopic velocity and temperature measurements, and warrants further investigation of the plume structure by more detailed spectroscopic and photographic techniques.

3-2 SPECTROSCOPIC OBSERVATIONS

The highly nonequilibrium conditions usually found in all MPD arcs make quantitative spectroscopic studies of the plasma properties in these devices very difficult. As a result spectroscopic investigations have been used chiefly to identify the various molecular, atomic, and ionic species participating in the discharge.[15] Although the information obtained is primarily of a qualitative nature, considerable understanding of the structure of the exhaust plume can be gained.

The spectroscopic studies described here were carried out using a three-prism Steinheil G. H. glass spectrograph having a linear dispersion of 5.4 to 40 $\overset{\circ}{A}$/mm over the range from 4300 $\overset{\circ}{A}$ to 6600 $\overset{\circ}{A}$, and an effective speed of f/10.* To obtain satisfactory exposures of the plates it was necessary to expose the film for the entire duration of the discharge,

---

and the recorded spectra are consequently time integrated.[15]
However, based on two pieces of evidence of the quasi-steady
nature of the discharge it can be argued that the lack of
time-resolution is not a serious drawback: 1) the patterns
and intensity levels of discharge luminosity recorded in
Kerr-cell photographs of the discharge remain constant for
almost the entire duration of the current pulse,[15] and
2) the time-resolved light intensity along any line of sight
through the discharge is found to be essentially constant
over more than 70% of the current pulse. The latter is il-
lustrated in Fig. 3-2 which shows the development of in-
tensity with time of the 4879.9 Å AII spectral line on a
line of sight perpendicular to the discharge axis 4.6 cm
downstream of the chamber exit. (This record was obtained
photoelectrically using the apparatus described in Chapter
4.)

The discharge spectra were recorded with a slit width
of 2.5×10^{-2} mm on Kodak Royal-X Pan sheet film at several
locations in the arc chamber and exhaust plume (Fig. 3-3)
at the nominal operating condition of 16 kA, 6 g/sec. The
discharge was imaged on the spectrograph with a 19 cm focal
length, 5.0 cm diam achromatic lens such that the vertical
image slit extends to a radius of 7.5 cm on both sides of
the centerline.

The resulting spectra, covering the range from 4300 Å
to 6600 Å are shown in Figs. 3-4 and 3-5. For clarity only
the more prominent lines have been labeled. The following
radiating species have been identified: AII, C_2, CII, CIII,
HI, NII, OII and WI. All of these constituents are con-
tained in the propellant or materials of which the dis-
charge chamber is constructed. Interestingly, no lines of
neutral argon could be identified, indicating essentially
complete ionization of the propellant. However, within
the arc chamber the radiation from neutral argon may be ob-
scured by the abundance of lines of other species, particular-
ly those of C_2 in the same region of the spectrum. In fact

CURRENT 16 kA

4880 Å LINE
INTENSITY
(ARBITRARY
UNITS)

$\vdash$ 100 μ sec/DIV
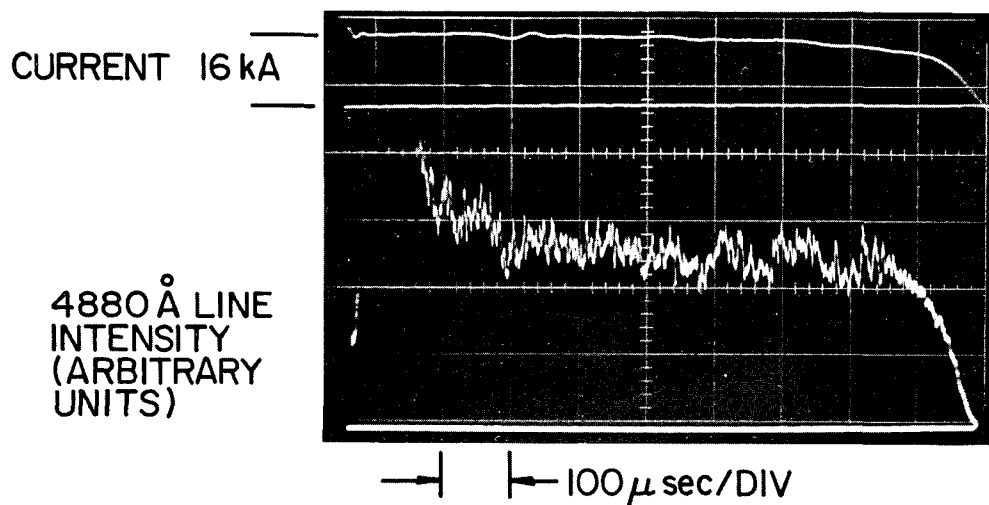
4880 Å AII LINE INTENSITY 4.6 cm
FROM CHAMBER EXIT

FIGURE 3-2
AP25·P·462

RADIAL EXTENT OF SPECTROGRAMS

RADIAL DISTANCE Y, cm

AXIAL DISTANCE X, cm

FIGURE 3-3
AP 25· 4843

22
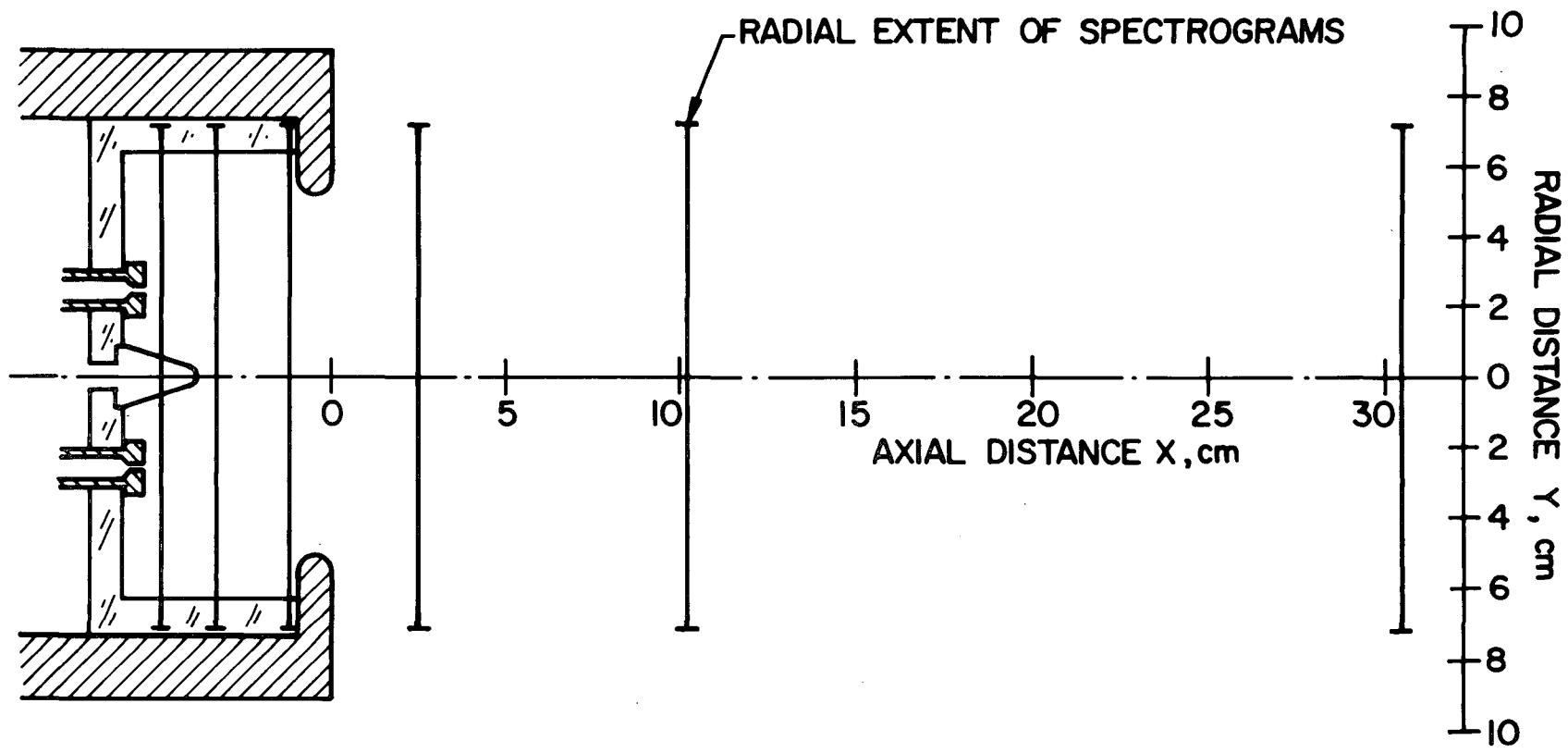
SCHEMATIC OF LOCATIONS EXAMINED WITH SPECTROGRAPH

DISCHARGE SPECTRA
J = 16 kA, ṁ = 6 g/sec

FIGURE 3-4
AP25·P·463

23

I·5999

I·5997

WAVELENGTHS
IN Å

b)

a)

4348.41 AⅡ

4426.01 AⅡ
4430.18 AⅡ

4609.60 AⅡ
4649.15 OⅡ

4726.91 AⅡ
4735.93 AⅡ

4806.07 AⅡ
4847.90 AⅡ
4861.33 Hβ
4879.90 AⅡ

5889.97/91.65 CⅡ

4331.25/2.06 AⅡ
4340.29/1.94 OⅡ
4370.76/1.36 AⅡ
4379.67 AⅡ
4400.09/1.02
4414.89/16.97 OⅡ
4448.88 AⅡ

4481.81 AⅡ

4545.08 AⅡ
4563.78/4.43 AⅡ
4579.39 AⅡ
4589.93 AⅡ
4638.87/41.83 OⅡ
4657.94 AⅡ

4764.83 AⅡ

4933.24 AⅡ
4965.12 AⅡ
5009.35 AⅡ
5062.07 AⅡ
5119.55 CⅡ
5145.36 AⅡ

6151.85 W/0.98 Th

X = 30.5 cm

5   O r,cm   5

X = 10.2 cm

5   O r,cm   5

DISCHARGE SPECTRA
J=16kA, ṁ=6 g/sec

FIGURE 3-5
AP25·464

24

recent spectra obtained in the near infrared have revealed lines of AI in the vicinity of the injector orifices.[21] The only neutral components detected in the visible light spectrograms appear to be HI and C_2, the latter found exclusively within the arc chamber, as will be shown later. Recently, near-ultraviolet spectroscopy[22] has revealed the presence of AIII in the luminous trumpet-shaped region between the cathode and anode and in the exhaust, within one anode orifice diameter of the chamber exit. In most of the exhaust plume, however, AII appears to be the dominant propellant specie.

Ideally, when the arc is properly operated, only the argon spectrum should be visible. In fact this is not the case, and the abundance of impurity lines of carbon, hydrogen and nitrogen indicates that a significant amount of material from the Plexiglas* end wall and the nylon** injectors is being ingested by the discharge. As will be seen, this has profound effects on the structure of the arc. (A detailed discussion of ablation phenomena is presented in Appendix A.)

The spectrogram in Fig. 3-4b taken at a point 3 mm in front of the cathode tip exhibits a narrow region of intense continuum radiation over the entire visible spectrum, a feature not observed elsewhere. This is believed to be bremmstrahlung radiation generated within a small region of very

---

*Plexiglas is a polymer of methyl-methacrylate:[23]

$$\left[\begin{array}{cc} H & CH_3 \\ | & | \\ -C- & C- \\ | & | \\ H & C-OCH_3 \\ & \| \\ & O \end{array} \right]_n$$
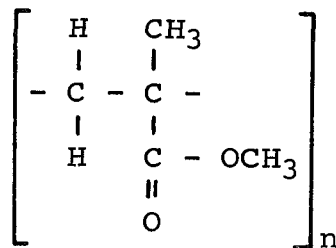
**Nylon 66 is a polyamide:[23]

$$\left[\begin{array}{cccccc} O & & & O & H & & H \\ \| & & & \| & | & & | \\ -C- & (CH_2)_4 & - & C- & N- & (CH_2)_6 & -N- \end{array} \right]_n$$
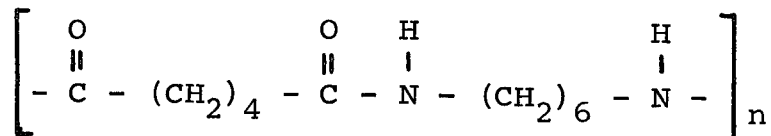
high particle density and temperature which exists off the cathode tip.[15]

The spectrograms in Fig. 3-4c and 3-4d, taken 1.25 cm upstream and 2.5 cm downstream of the chamber exit plane respectively, exhibit an interesting radial intensity profile in the spectral lines, which is central to the understanding of the structure of the exhaust. This is better illustrated in Fig. 3-6 which displays an enlarged section of the spectrogram of Fig. 3-4d in the 4600 $\overset{o}{A}$ region. The lines of AII exhibit three relative maxima of intensity, one on the centerline and one on either side at a radius of about 1.5 cm. The lines of CII, OII, and NII, on the other hand, display two off-center maxima at radii which correspond to the minima in the argon lines. At the centerline the impurity lines exhibit a shallow relative minimum. Furthermore, the impurity lines appear to have a smaller radial extent than those of argon, indicating a concentration of the impurities in the central core of the exhaust. This interesting species inhomogeneity, which can be identified with the striated structure of the exhaust luminosity in Fig. 3-1 is detectable as far as three anode orifice diameters ($\sim$30 cm) downstream of the chamber exit. (Fig. 3-5)

3-3   FILTER PHOTOGRAPHY

Although the spectrograph is capable of yielding information about all the radiating species simultaneously, it is severely limited in spatial resolution, allowing examination of only one dimension at a time. A further step in exposing the species structure is to photograph the entire discharge through narrow spectral filters selected to isolate certain lines or groups of lines of the various radiating species. By using a number of different lines of sight it is possible to obtain a fairly accurate assessment of the three dimensional distribution of each radiating constituent.

Ideally, the filter photography should be done with a Kerr-cell shutter to obtain time-resolved information, however this is not possible because narrow band filters

ARGON LINE INTENSITY

4530.57Å
4535.51
4537.67
4545.08
4563.78/4.43
4579.39
4589.93
4598.77
4609.60
4637.25
4657.94

A II LINES

OII 4596.23
OII 4602.08
CII 4618.85
CII 4630.52/NII 0.55
OII 4638.87
OII 4641.83
CIII 4647.40
OII 4649.15
OII 4650.85
OII 4661.65
OII 4676.25

IMPURITY LINES

I·5996

IMPURITY LINE INTENSITY

5   5 r, cm

Ç

FIGURE 3·6
AP 25·P·452

27
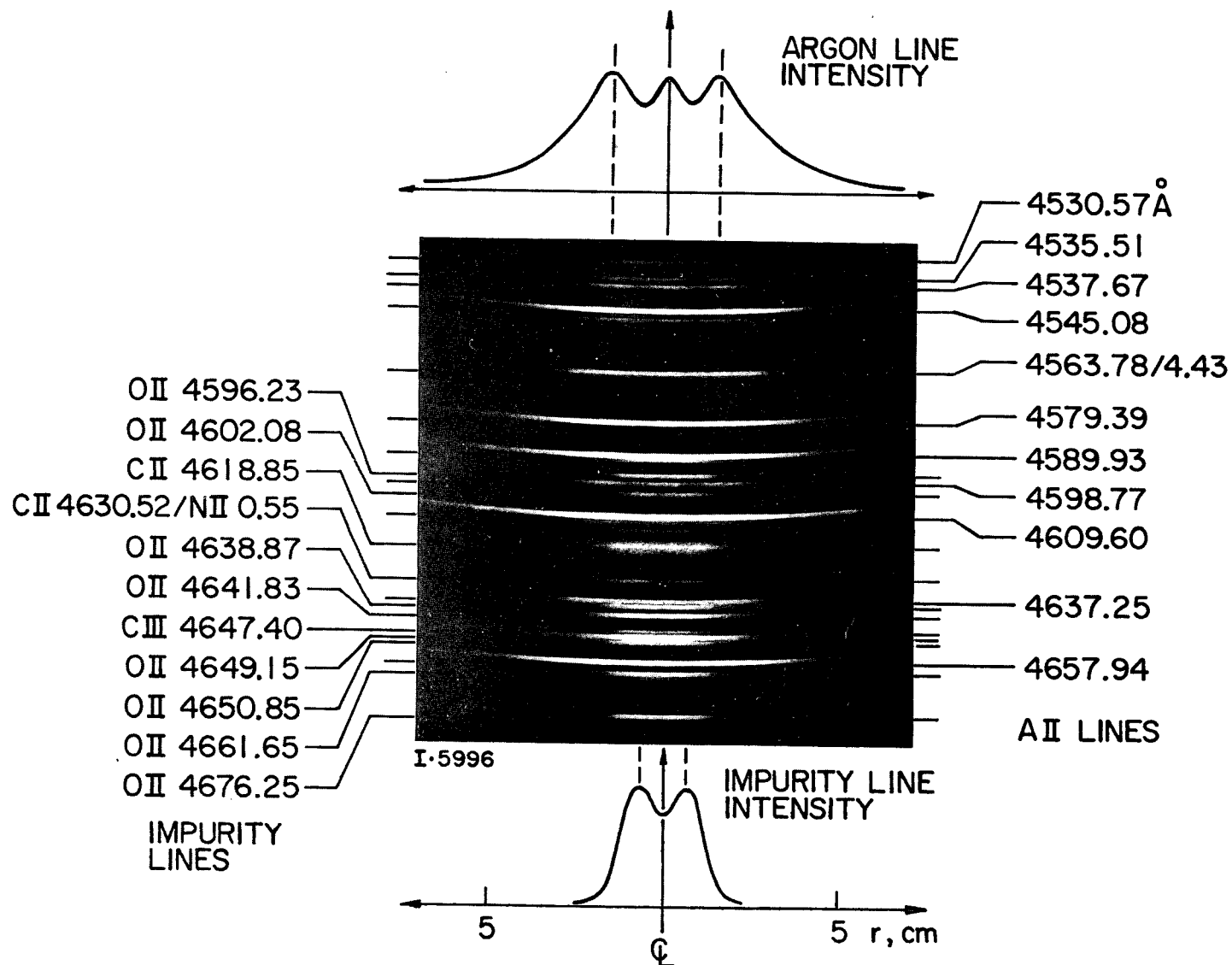
ENLARGED SECTION OF DISCHARGE
SPECTRUM X= 2.5 cm , J=16 kA , ṁ = 6 g/sec

transmit only a small fraction of the entire visible radiant energy (typically 1%), precluding good exposures on available low grain films at microsecond exposure times. However, because of the quasi-steady nature of the discharge over most of the current pulse, the same arguments which are used to justify time-integrated spectroscopy are applicable to time-integrated photography. The photographs are recorded by simply leaving the camera shutter open for the duration of the current pulse.

The spectral transmission curves of the five optical filters used in this investigation are shown in Fig. 3-7. All are narrow-band interference filters ranging in half-width from 10 $\overset{o}{A}$ to 90 $\overset{o}{A}$. The prominent spectral lines of the discharge which are transmitted by each filter are also shown. The 4880 $\overset{o}{A}$ and 4486 $\overset{o}{A}$ filters are used to observe AII emission, the 5910 $\overset{o}{A}$ and 5510 $\overset{o}{A}$ filters CII and C_2 emission, and the 6580 $\overset{o}{A}$ filter HI and CII emission.

With each of the filters the discharge was photographed at five different lines of sight, three in the horizontal plane containing the discharge axis, giving side, perspective and end views of the exhaust plume and discharge chamber, and two in a plane inclined 30° above the horizontal, also containing the axis, giving side and perspective views. Figure 3-8 displays photographs of the discharge chamber as recorded along these lines of sight. Two cameras were used in the study. Black and white photographs on Type 55 P/N Polaroid positive-negative film (ASA 50) were obtained by means of a 4 x 5 Graflex Speed Graphic camera with an f/4.7 lens. Color slides on High Speed Ektachrome (Daylight, ASA160) were obtained with a Nikon F 35mm single lens reflex camera equipped with either a 55mm Micro Nikkor Auto f/3.5 lens or a 200 mm Nikkor Auto f/4 lens. The photographs shown in this dissertation are enlargements made from the Polaroid negatives.
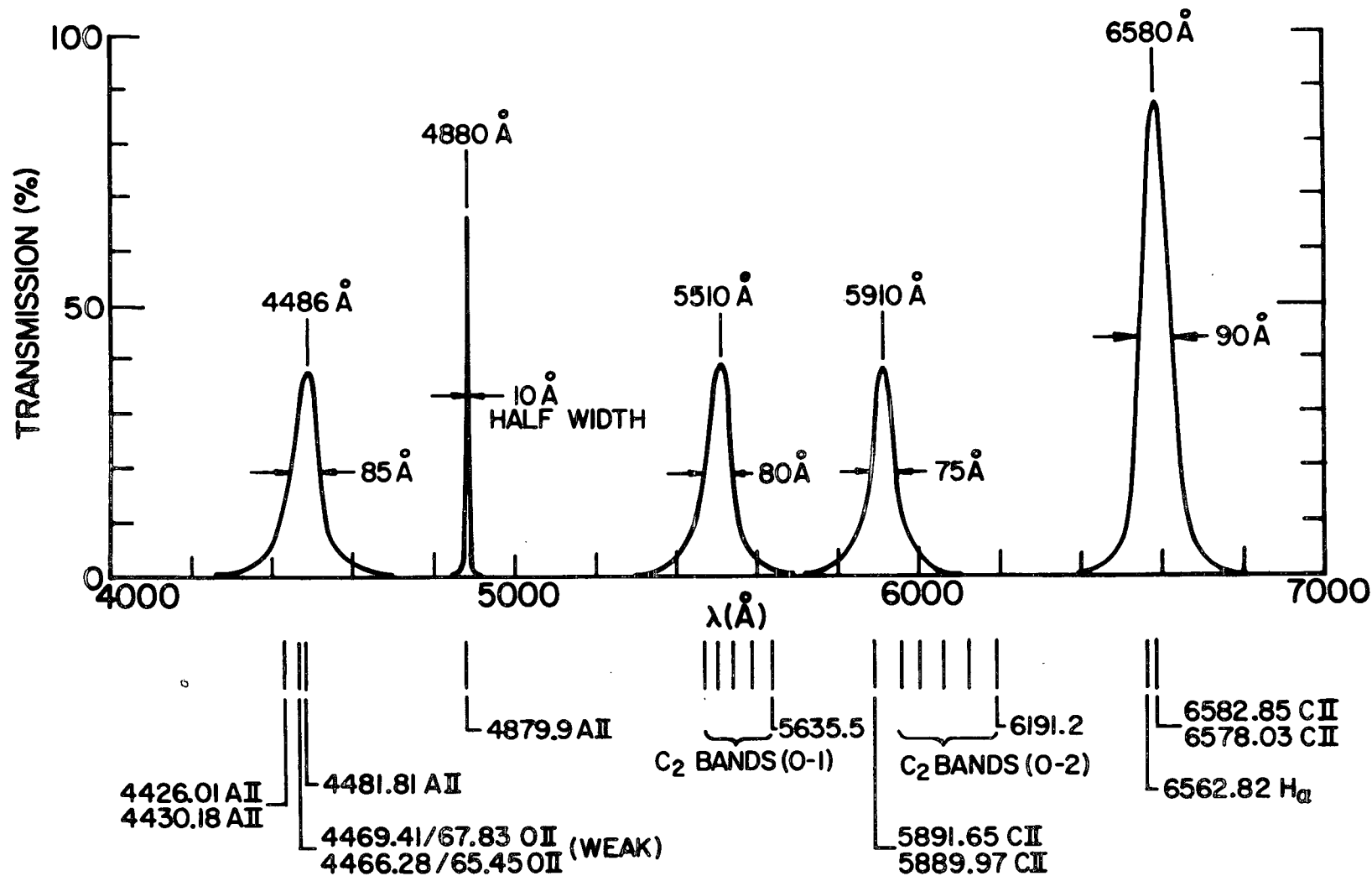
TRANSMISSION CURVES OF SPECTRAL FILTERS

FIGURE 3-7
AP 25 · 4844

29

a) SIDE

b) PERSPECTIVE

c) 30° END

d)

e)

f)
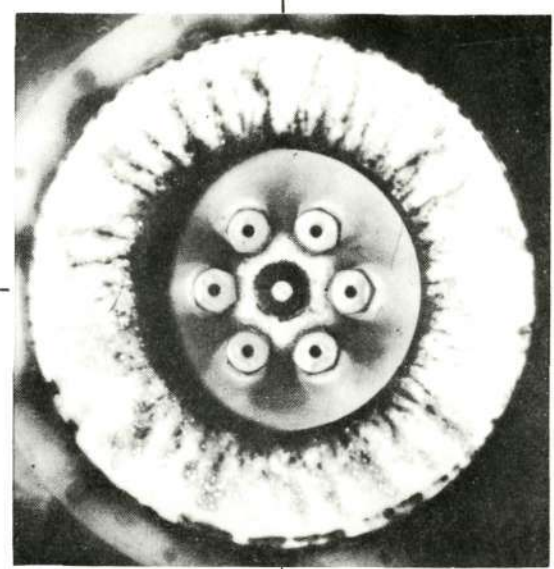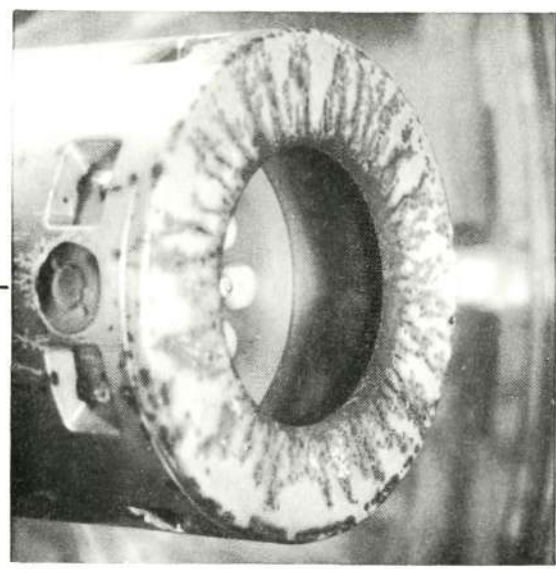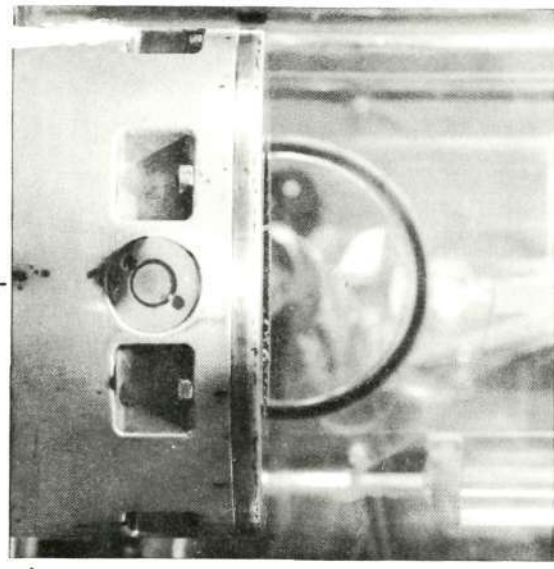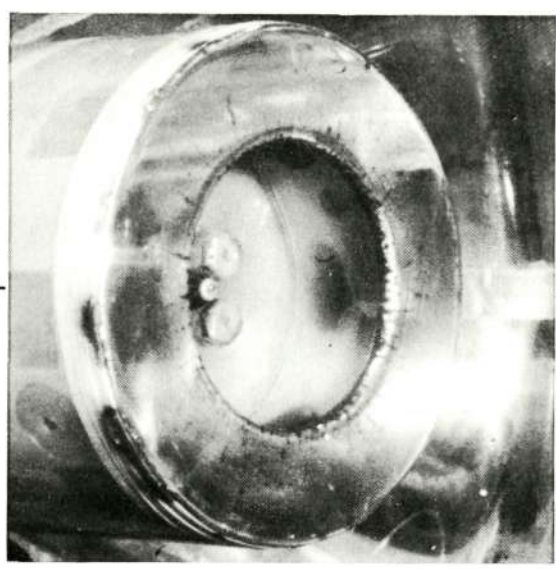
VIEWS OF ARC CHAMBER
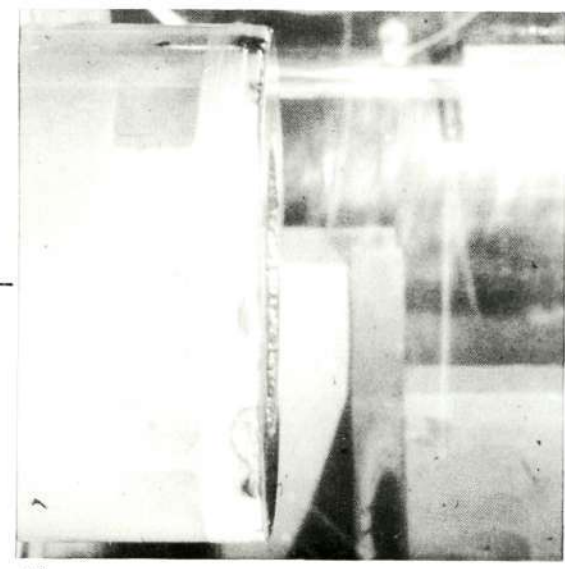
FIGURE 3-8
AP25·P·465

3-4 ARGON DISTRIBUTION

Photographs of the discharge taken through the 4880 $\overset{o}{A}$ AII filter at the nominal operating condition of 16 kA and 6 g/sec argon flow are shown in Fig.3-9. It is evident that the distribution of AII exhibits a complex azimuthal structure related to the location of the mass injectors (which can be seen faintly in the end views). Downstream of the cathode the ionized argon appears collimated in six discrete jets which maintain their identity well downstream of the arc chamber exit. (The abrupt transverse cutoff in the luminosity about an anode orifice diameter downstream of the exit in these photographs is a result of the narrow bandpass (10 $\overset{o}{A}$) of the 4880 $\overset{o}{A}$ filter. The bandpass of an interference filter shifts towards shorter wavelengths as the angle of the incident light deviates from the filter normal.[24] If the bandpass is narrow the filter will have a narrow acceptance angle and thus a limited field of view.)

The side and perspective views in the 30° plane (Figs. 3-9d and 3-9e) show a complete absence of AII radiation along the axis of the plume suggesting the lack of argon in that region. The central luminous spot visible in the end view, Fig. 3-9c, corresponds to the previously mentioned region of intense continuum emission immediately in front of the cathode tip. The discrete jet structure observed in the photographs of Fig. 3-9 explains the curious radial intensity structure of the spectral lines of AII in Figs. 3-4c - 3-6, which were recorded on a line of sight perpendicular to the discharge axis in the horizontal plane. The three maxima of the spectral lines correspond to the three luminous jets visible in Figs. 3-9a.

Great care must be exercised in interpreting the luminous jets to be regions of argon concentration. The emissivity of a given radiating specie for a particular spectral transition is not only a function of its number density, but also a strong function of the prevailing electron temperature.[25,26] Thus the observed patterns of luminosity could

a) I·8957

b) I·8960

c) I·7618

d) I·8777

e) I·8763

f) I·7618

SIDE VIEW

PERSPECTIVE VIEW

30°

END VIEW

FIGURE 3 - 9
AP25·P·466

32
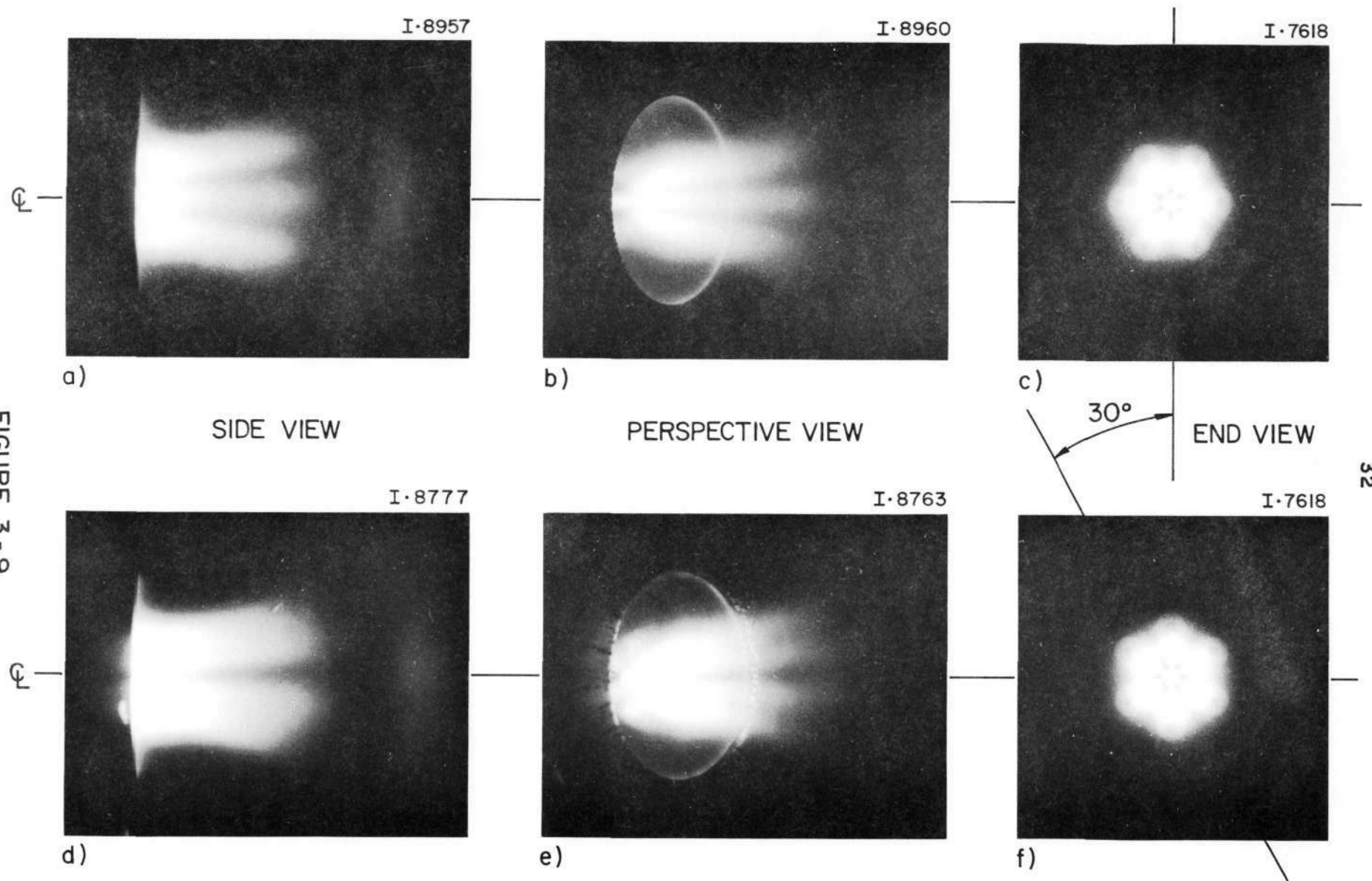
DISCHARGE AT 4880 Å SHOWING DISTRIBUTION OF A II. J = 16 kA, ṁ = 6 g/sec

conceivably be a convolution of the electron temperature
field and the species density distribution. Fortunately,
measurements of electron temperature[8,9] indicate that it
has a uniform value of about 1.5 eV throughout the
entire arc chamber and the near exhaust. Furthermore, in
the exhaust plume there appears to be only a gentle nega-
tive axial gradient in electron temperature, as will be dis-
cussed in Chap. 4. Consequently, it can be assumed that
the observed luminous patterns correspond to maps of species
density.

Photographs through the 4486 $\overset{o}{A}$ filter (Fig. 3-10) reveal
a luminous structure virtually identical to that observed at
4880 $\overset{o}{A}$, a result which is consistent with the similarity of
the radial intensity profiles of all the spectral lines of
AII. The 4486 $\overset{o}{A}$ filter is broader than the 4880 $\overset{o}{A}$ filter
(90 $\overset{o}{A}$ vs. 10 $\overset{o}{A}$) and thus transmits more continuum light and
a few impurity lines (OII) causing a slight loss of definition
of the jets.

Recent spectroscopic investigations in the near-ultra-
violet[22] reveal a distribution of AIII similar to that of
AII, providing compelling additional evidence that the AII
jets do actually define regions of argon concentration. With
the apparent complete absence of AI from the exhaust plume
it must be concluded that there is in fact very little or no
argon between the jets and in the central core of the exhaust.

Flow Visualization

It is important for the velocity measurements discussed
in Chap. 4 to determine whether the observed argon jet struc-
ture is bounded by flow streamlines, _i.e_: whether the flow
direction is along the luminous jets. A simple test is to
place a spherical body in one of the argon jets and note the
direction of the resulting bow shock* To a first approxima-
tion this will reveal the local flow direction. Figure 3-11

---

*It is known from a previous series of wedge flow studies[11]
that the flow in the exhaust plume is everywhere supersonic.
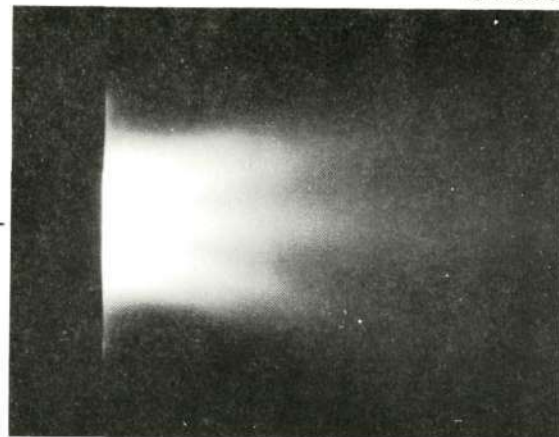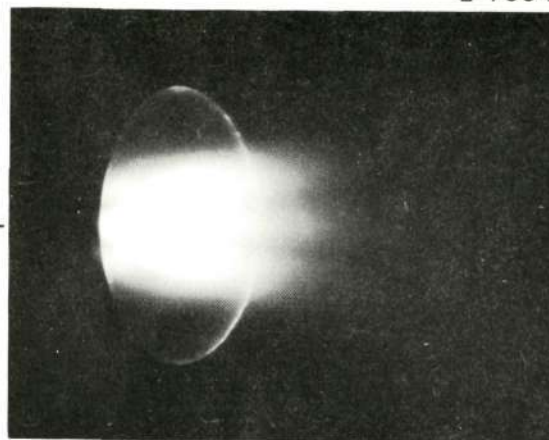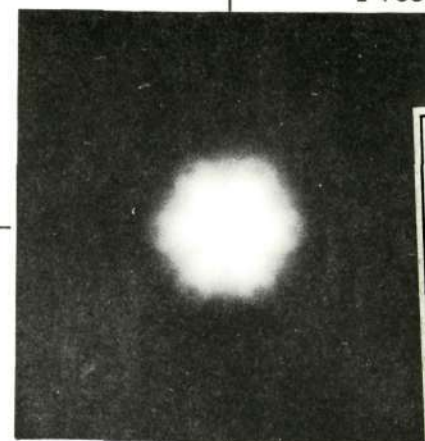
34

SIDE VIEW

PERSPECTIVE VIEW

30°

END VIEW
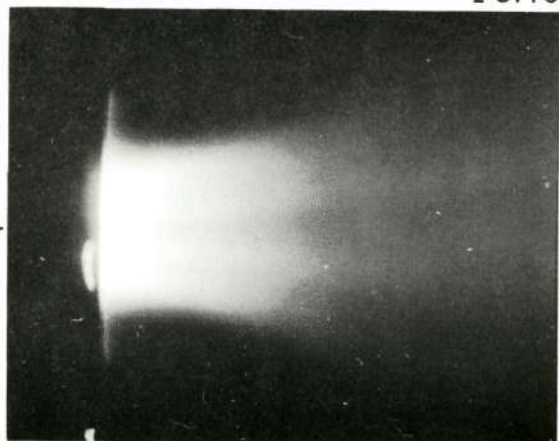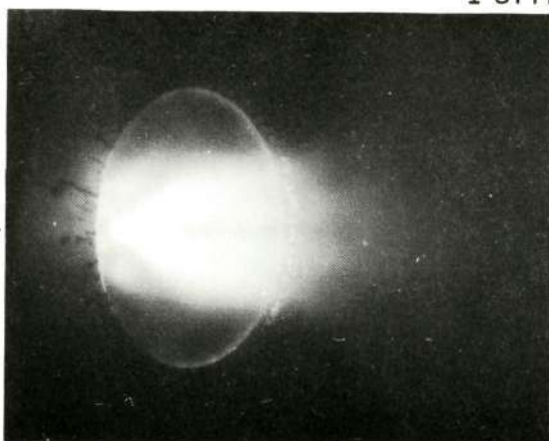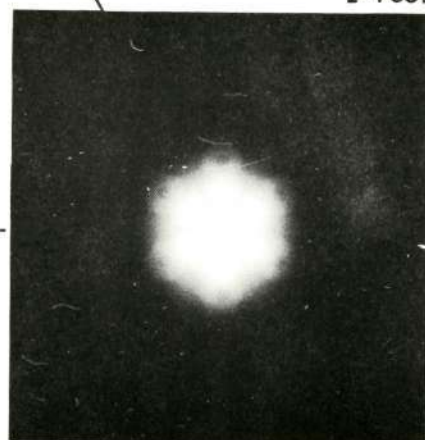
FIGURE 3-10
AP25·P·467

DISCHARGE AT 4486 Å SHOWING DISTRIBUTION OF AII. J = 16kA, ṁ = 6 g/sec

FIGURE 3-11
AP 25·P·468
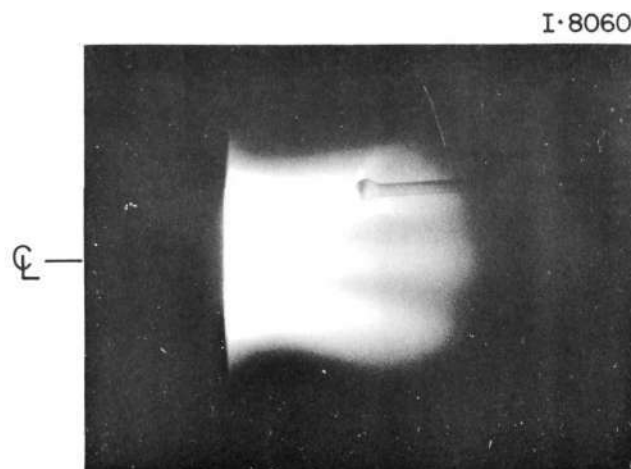
I·8060

a) PROBE IN UPPER NEAR
ARGON JET
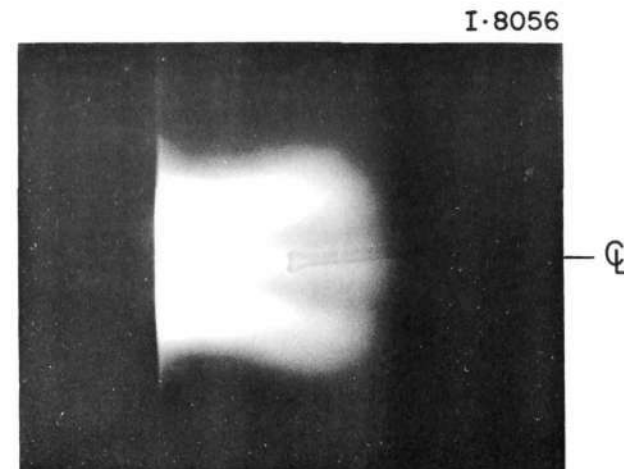
I·8056

c) PROBE ON PLUME AXIS

0   5
L_L_L_L_L_L
SCALE (cm)
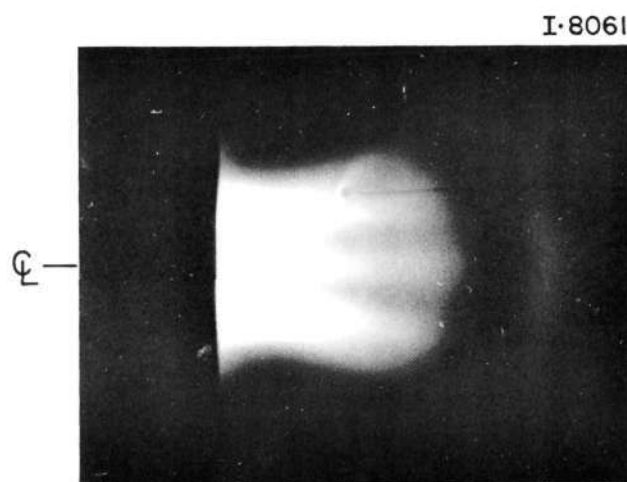
I·8061

b) PROBE IN UPPER FAR
ARGON JET

I·8057
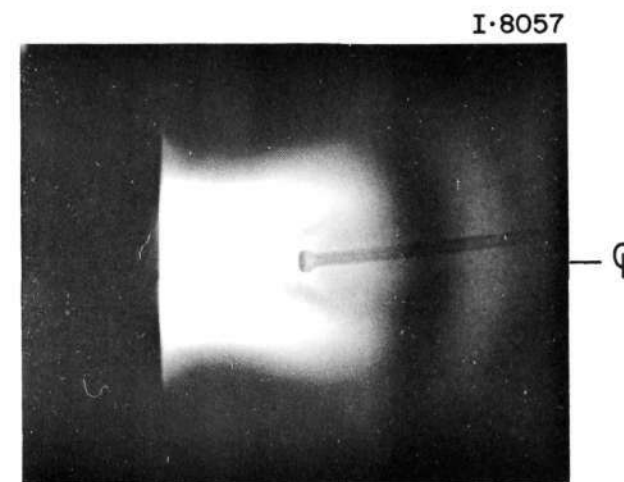
d) PROBE IN NEAR MIDDLE
ARGON JET

A II FLOW VISUALIZATION WITH SPHERICAL PROBE. (4880 Å FILTER)
$J = 16$ kA, $\dot{m} = 6$ g/sec

displays the results of such an experiment, photographed at 4880 Å. An 8 mm O.D. spherical bulb blown on the end of a 5 mm O.D. pyrex glass tube is immersed in the upper near argon jet in Fig. 3-11a producing a distinct bow shock. The axis of symmetry of the shock appears to be parallel to the luminosity, indicating that the local flow direction is along the luminous jet. Figure 3-11b shows the probe in the upper far jet, with similar results. If the probe is placed on the exhaust centerline, Fig. 3-11c, no shock is visible through the argon filter, attesting to the lack of argon in the core of the exhaust. When the probe is moved horizontally into the middle near jet, Fig. 3-11d, the bow shock reappears. Since the axis of symmetry of the shock wave is in this case parallel to the discharge axis, it implies that there is no rotational component of velocity in the exhaust plume.

It is interesting to note, at this point, that at the chamber exit the radius which encloses the six luminous argon jets also encloses virtually all of the flow momentum exiting from the chamber.[10] It is not clear whether all the injected argon is also contained within this radius. It has been suggested by Cory[10] that as much as 40% of the injected propellant may be leaking out of the chamber at low velocity through the annular region between the luminous plume and the anode orifice. That no significant argon radiation from any level of ionization can be detected spectroscopically in this region would tend to cast some doubt on this contention.

3-5 DISTRIBUTION OF IMPURITIES

In Fig. 3-6 it can be seen clearly that the lines of CII, OII, and NII have a smaller radial extent than those of AII and exhibit maxima where the lines of AII exhibit minima. It can be concluded from this that the regions devoid of argon must be occupied by these impurities which are produced by the ablation of the Plexiglas end wall of the arc chamber. Again, by photography through suitable filters, the distribution of the ablated material in the exhaust can be determined.

Distribution of Carbon

Figure 3-12 displays photographs taken through the
5910 $\overset{o}{A}$, 75 $\overset{o}{A}$ bandwidth interference filter at the 16 kA,
6 /sec operating condition. Prominent in this spectral band
are the 5889.97 $\overset{o}{A}$ and 5891.65 $\overset{o}{A}$ lines of CII and the tail of
the C_2 0-2 Swan band system whose head is at 6191.2 $\overset{o}{A}$. It
can be seen, by comparison with the photographs in Fig. 3-9
and 3-10 that these constituents are found precisely in those
regions of the chamber and exhaust where argon is absent and
vice-versa. The luminous patterns inside the chamber are
generated by both C_2 and CII, while those outside in the ex-
haust plume are generated by CII alone, as will be shown
later. The side and perspective views exhibit clearly the
expected concentration of the CII near the exhaust centerline.
The slight decrease in luminosity at the centerline visible
in Figs. 3-12a and 3-12b was noted previously on the spectral
lines of CII and other impurities. When viewed along the 30°
inclined plane, which cuts between injectors, the CII plume
shows a distinct increase in luminosity at the centerline.
These interesting features are a result of looking at the
star-shaped cross section of the CII plume on edge from the
two different sets of viewing angles. If the plume is viewed
along the horizontal plane the line of sight across the axis
sees a smaller thickness of CII than on either side. On the
other hand, at an angle 30° to the horizontal the line of sight
across the axis passes through two diametrically opposed arms
of the star shaped cross section of the CII flow and the center-
line appears brighter.

Flow visualization (Fig. 3-13) by means of the spherical
probe technique used in the study of the argon jets helps
confirm some of the conclusions drawn above. Figure 3-13b,
photographed at 5910 $\overset{o}{A}$, shows the 8 mm spherical probe im-
mersed in the carbon plume on the centerline of the exhaust,
4.6 cm from the anode plane. A very strong bow shock is
produced by the flow over the probe, confirming the
presence of carbon in the core of the exhaust. (The shock

SIDE VIEW   PERSPECTIVE VIEW   END VIEW

30°

FIGURE 3-12
AP25·P 456
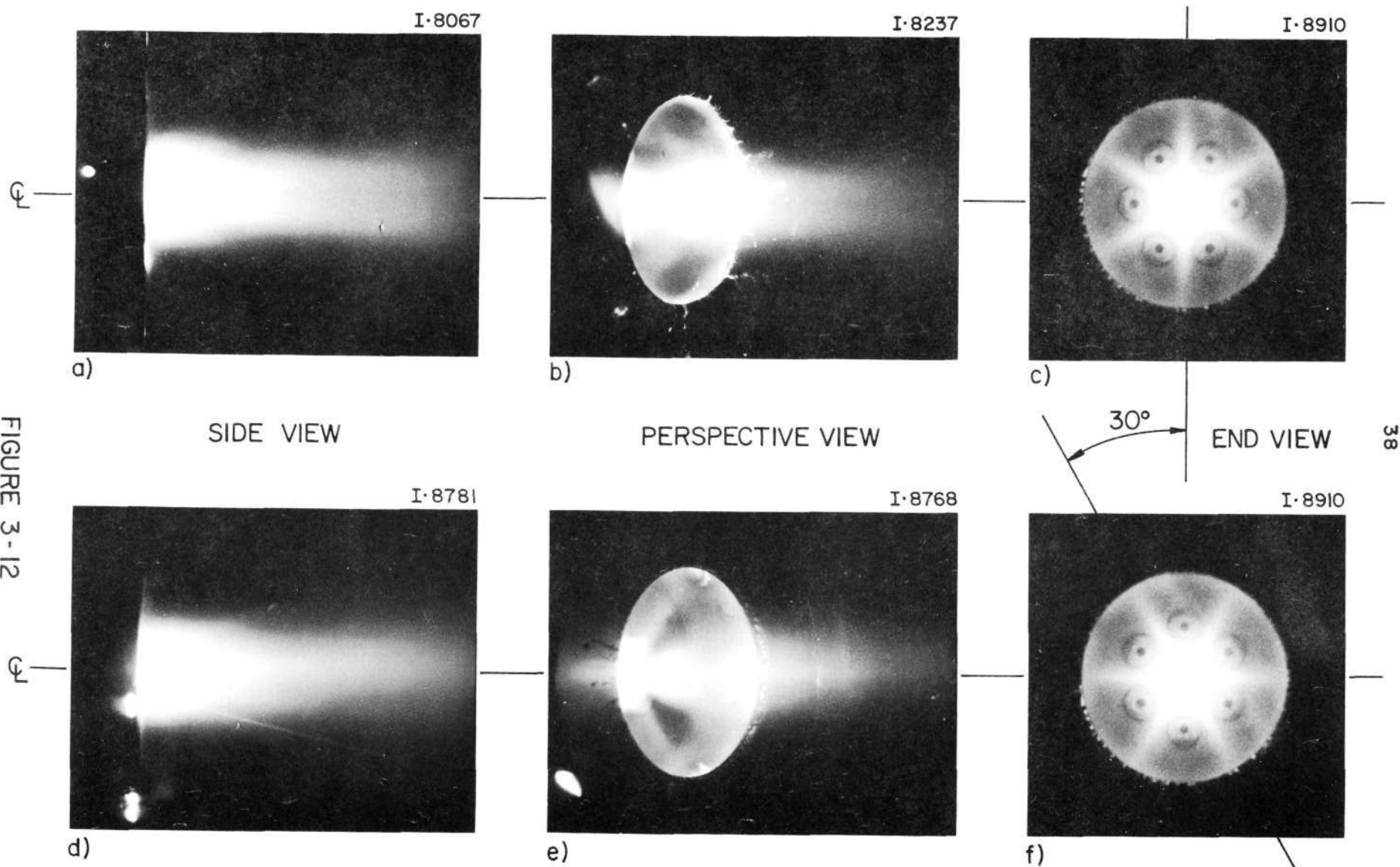
DISCHARGE AT 5910 Å SHOWING DISTRIBUTION OF CII AND C_2. $J = 16\,kA$, $\dot{m} = 6$ g/sec

I·8229
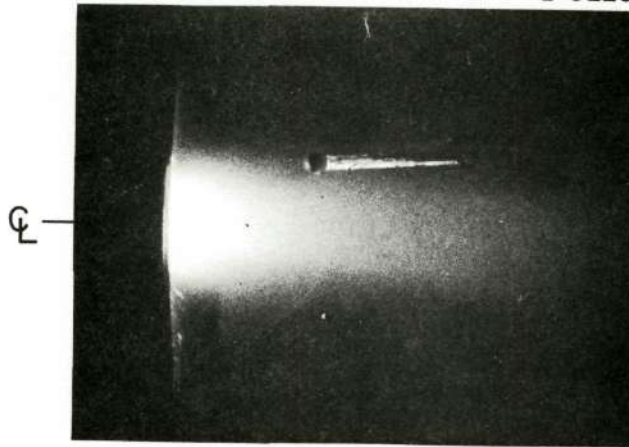
a) PROBE IN UPPER NEAR
ARGON JET

I·8066
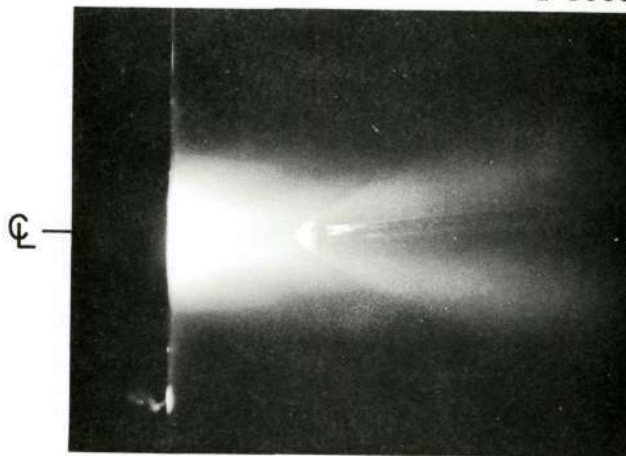
b) PROBE ON PLUME AXIS

C II FLOW VISUALIZATION WITH SPHERICAL PROBE
(5910 Å FILTER) J = 16 kA , $\dot{m}$ = 6 g/sec

FIGURE 3-13
AP25·P·469

angle corresponds roughly to a flow Mach number of 2.2 .
If it is assumed that the exhaust flow can be approximated
by a source flow model the flow Mach number is estimated
to be about 6 where the shock reaches the visible boundary
of the carbon jet.) When the probe is located in one
of the argon jets, as shown in Fig. 3-13a, no shock is
visible at 5910 $\overset{\text{o}}{\text{A}}$, indicating the absence of carbon there.

The star-shaped luminous pattern visible inside the
chamber in the end view of the discharge clearly indicates
where ablation of the Plexiglas back plate occurs. The
ablation pattern etched on its surface can be easily dis-
cerned in the end view of the chamber in Fig. 3-8. In the
perspective views in Fig. 3-12 it can be seen that a luminous
star-shaped layer extends about a cathode length into the
chamber from the back plate. This immediately identifies
it with the luminous layer along the end wall visible in the
side-on Kerr-cell photograph of Fig. 3-1. The products of
ablation generated at the insulator surface over this star-
shaped region retain this geometry as they are accelerated
downstream and are thus responsible for the six-jet struc-
ture of the argon in the plume.

In Fig. 3-14 are shown three enlarged sections of the
spectrograms of Figs. 3-4a, c and d in the range of 5300 $\overset{\text{o}}{\text{A}}$ -
5900 $\overset{\text{o}}{\text{A}}$, which contains the 0-1 Swan band system of C_2. The
first spectrogram, obtained 1.1 cm in front of the Plexiglas
back plate of the arc chamber, i.e: within the luminous star-
shaped layer at the plate, shows that the lines of C_2, CII, and
CIII have similar radial intensity profiles, which indicate
that these three species have similar spatial distributions
there. No lines of neutral carbon could be identified, a
consequence of the relatively small number of lines of CI in
the visible spectrum and the presence of many other lines
which make unambiguous identification very difficult. It seems

I·5993

C̶L̶

a) 1.1 cm DOWNSTREAM
OF PLEXIGLAS
END WALL

5470.3 C₂
5501.9 C₂
5540.7 C₂
5585.5 C₂
5635.5 C₂
5696.0 CⅢ
5889.97 CⅡ
5891.65 CⅡ

I·5995

C̶L̶

b) 1.25 cm UPSTREAM
OF EXIT PLANE

5397.60 AⅡ
5402.69 AⅡ
5407.44 AⅡ
5454.41 AⅡ
5648.50 CⅡ
5648.08 CⅡ
5662.51 CⅡ
5679.56 CⅡ

I·5996

C̶L̶

c) 2.5 cm DOWNSTREAM
OF EXIT PLANE
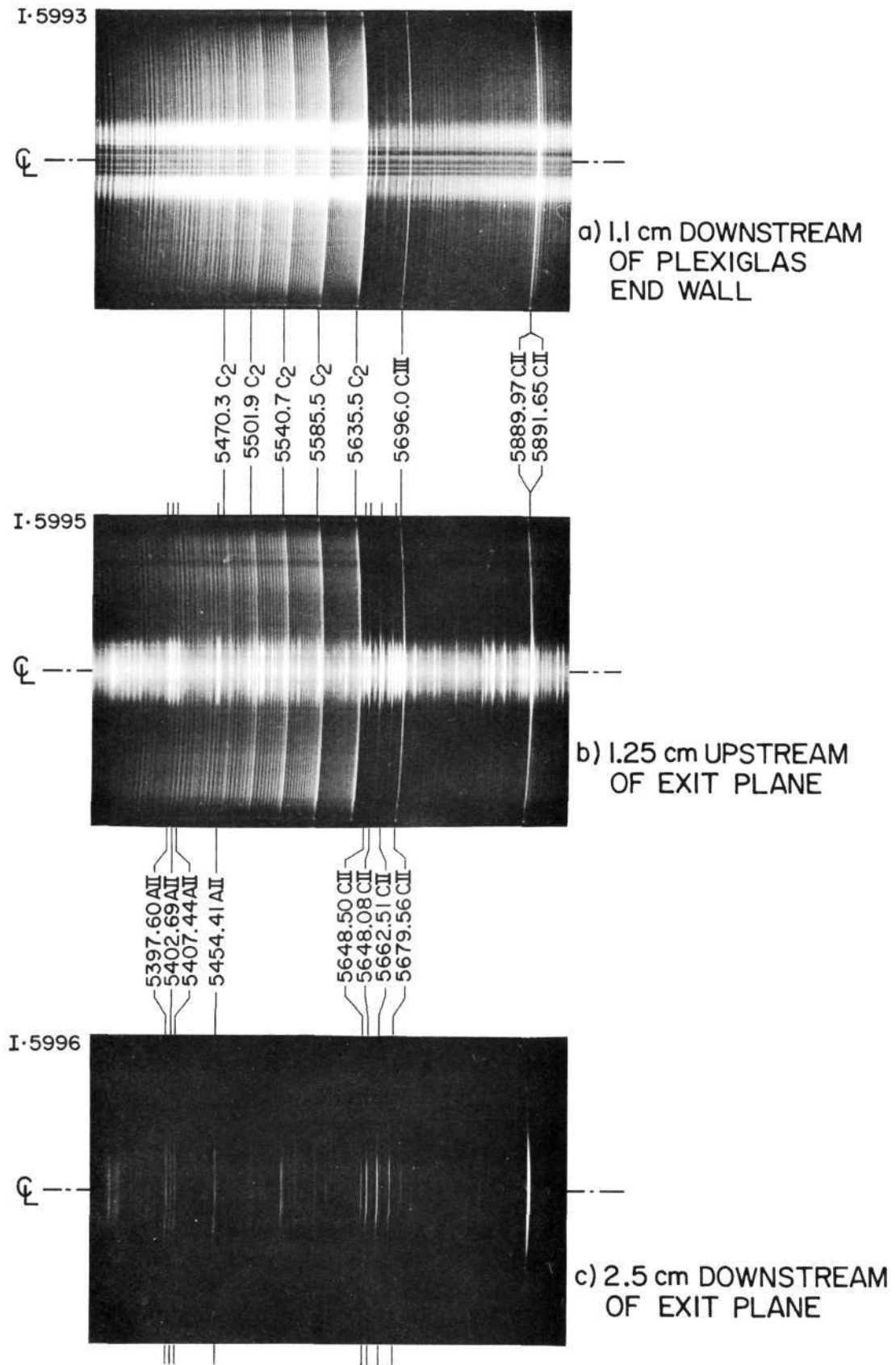
ENLARGED SECTIONS OF DISCHARGE SPECTRA

FIGURE 3 - 14
AP 25 · P · 470

reasonable however, that neutral atomic carbon must be present in any region that contains both the molecular and singly ionized specie.

The rather abrupt termination of the luminosity of the layer at the Plexiglas wall about one cathode length from the wall is thought to be due to the rapid disappearance of C_2 through dissociation. Except for a thin layer along the surface of the circular pyrex wall there appears to be no molecular carbon present downstream of the cathode. In part this can be seen in Fig. 3-15 which shows two perspective views and one end view of the chamber interior through the 5510 $\overset{\text{o}}{\text{A}}$, 80 $\overset{\text{o}}{\text{A}}$ wide interference filter, which transmits part of the 0-1 band system. Only a short plume extending from the cathode to the plane of the anode is visible. This short plume does not itself contain any C_2 as can be ascertained from the spectrogram in Fig. 3-14b, obtained 1.25 cm upstream of the exit plane. All the spectral lines except those of C_2 show a marked increase in intensity near the centerline. The intensity of the C_2 bands remains nearly constant across the chamber diameter indicating that the C_2 radiation originates either behind or in front of the plume, most likely at the cold chamber walls where carbon deposits have been found. The short plume in Figs. 3-15a and 3-15b must therefore consist of other species which radiate within the bandpass of the 5510 $\overset{\text{o}}{\text{A}}$ filter. None of these constituents have been positively identified but they are believed to be impurities in the higher stages of ionization. The spectrogram of Fig. 3-14c shows a complete absence of molecular carbon bands 2.5 cm outside the chamber. The 5696.0 $\overset{\text{o}}{\text{A}}$ line of CIII is also absent, while the 5889.97 $\overset{\text{o}}{\text{A}}$ and 5891.65 $\overset{\text{o}}{\text{A}}$ lines of CII are prominent. Spectrograms farther downstream (Fig. 3-5) exhibit only the singly ionized specie of carbon.

Distribution of Oxygen and Nitrogen

No photographs were taken to directly reveal the distribution of OII or NII because virtually all of their line radiation is emitted too close to lines of CII or AII. This would
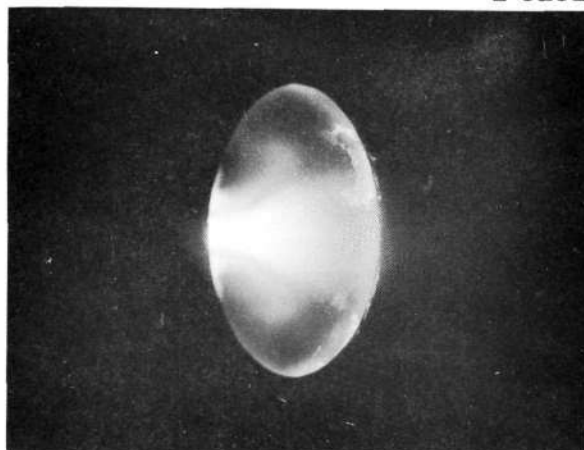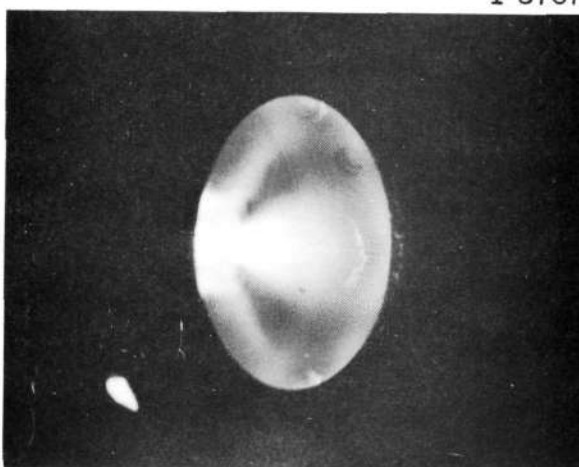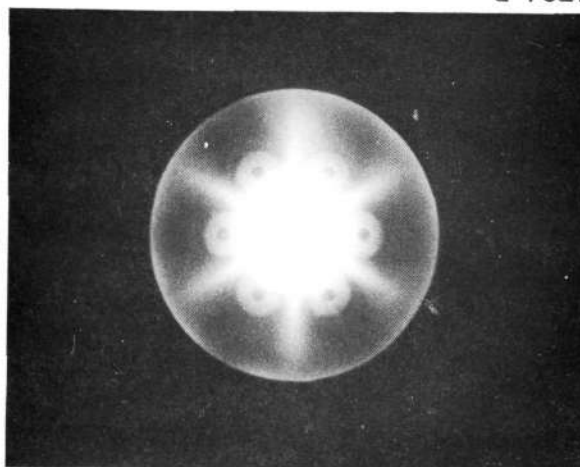
DISCHARGE AT 5510 Å SHOWING DISTRIBUTION OF C_2
$J = 16$ kA , $\dot{m} = 6$ g/sec

FIGURE 3-15
AP25·P·454

require the use of very narrow bandwidth filters (< 2 Å) which would severely limit the field of view due to the very small angle of acceptance of such filters. However, OII and NII are expected to have concentration profiles similar to CII because their spectral lines exhibit the same radial intensity features. (Fig. 3-6)

Distribution of Hydrogen

In all the spectrograms of the discharge (Figs. 3-4 and 3-5) the 4861.33 Å H_β line of atomic hydrogen is conspicuous. The H_α line at 6565.82 Å falls near the limits of the spectral sensitivity of the Royal-X Pan emulsion in the red and is thus poorly exposed. The H_γ line at 4340 Å is intrinsically fainter than the other two lines[27] and apparently so broad that it is not easily recorded either. Figure 3-16 shows photographs of the discharge taken through the 6580 Å, 90 Å half-width interference filter which transmits the 6562.82 Å H_α line and the 6578.03 Å and 6582.85 Å lines of CII (Fig. 3-8). Arc current and propellant mass flow are 16 kA and 6 g/sec respectively. It has already been demonstrated that CII is found predominantly in the core of the exhaust flow. Thus in Fig. 3-16 the high luminosity of the core of the exhaust is due in large part to the CII radiation. The fainter but more extended part of the plume is due to H_α radiation exclusively. The hydrogen appears to be present throughout the entire exhaust plume, even within the argon jets, and is found at radii beyond the visible outer boundaries of the argon and carbon flows. Furthermore, inside the arc chamber the distribution of hydrogen appears to be more uniform than that of carbon. This is probably a result of the greater mobility of hydrogen due to its very low atomic weight.

Since ionized hydrogen does not have a line spectrum, its presence must be inferred from that of the neutral specie and the fact that the other constituents of the exhaust (all of which have approximately the same ionization potential as hydrogen) are present in only singly or doubly ionized form.

a)

b)
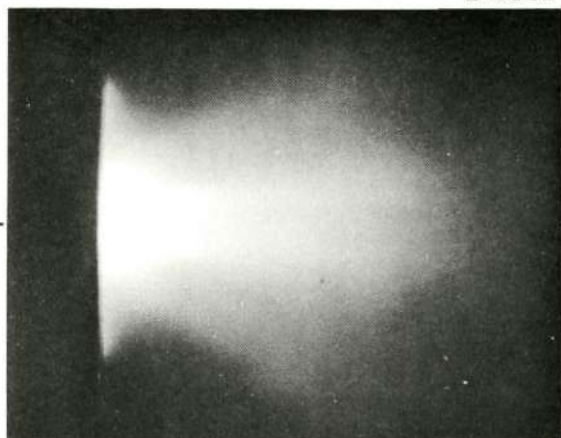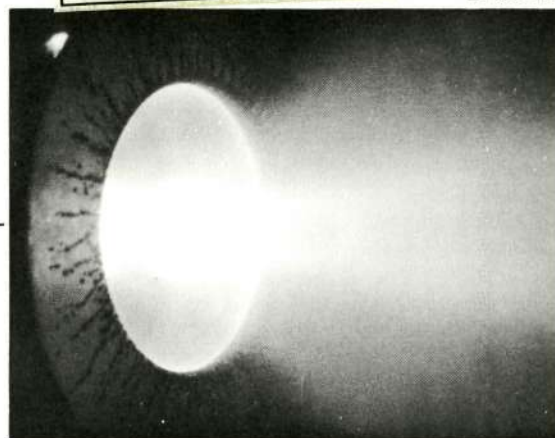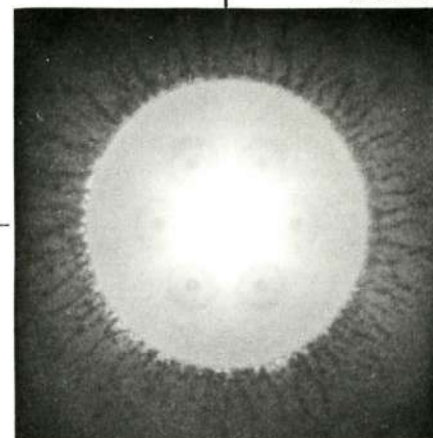
c)

SIDE VIEW

PERSPECTIVE VIEW

END VIEW

d)

e)

f)
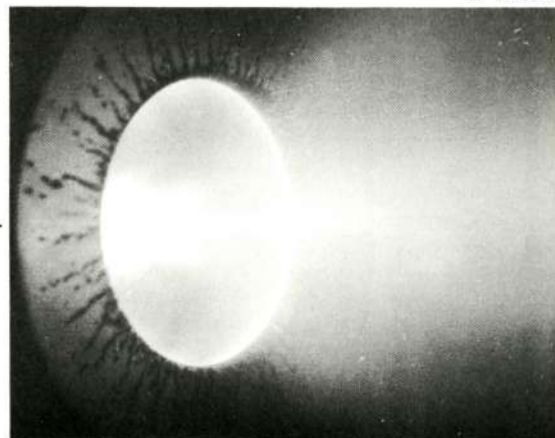
FIGURE 3-16
AP25·P·455
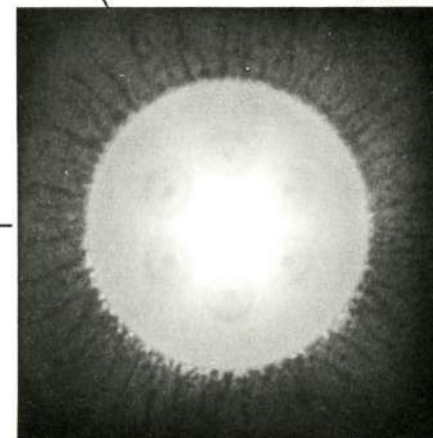
DISCHARGE AT 6580 Å SHOWING DISTRIBUTION OF HI AND CII. J=16 kA, ṁ=6 g/sec

The fact that neutral atomic hydrogen is detectable, whereas other neutral atomic species are not is most likely a consequence of the intrinsically greater strength of the atomic hydrogen spectral lines.[27] Very small concentrations of neutral hydrogen can give rise to the observed intensities. The pervasive presence of this impurity is on one hand useful, since it allows determination of electron densities in the chamber and exhaust through measurements of the Stark broadening of its spectral lines. A typical contour map of electron density obtained in this fashion is shown in Fig. 3-17.[15] It is interesting to note that the sharp upstream edge of the conical plume between cathode and anode visible in all the discharge photographs lies approximately parallel to the local electron density contours, lending evidence to the hypothesis of Turchi[8,9] that a trailing shock off the cathode tip may be responsible for the sharp upstream plume boundary

A disadvantage of the hydrogen contamination is that even relatively small concentrations of the ionized specie can significantly affect every process that involves the diffusion of positive charges in the plasma. For example, measurements of flow velocity by means of biased double electrostatic probes aligned parallel and perpendicular to the flow are sensitive to the concentration and atomic weight of the ions impinging on the probe surfaces.[28] If the probes are immersed in a flowing mixture of ions of different mass it is necessary to know their relative concentrations to enable reduction of the observed ion saturation currents to flow velocities. Another effect of the presence of light ions such as hydrogen is a significant increase in the ion acoustic velocity,[29] which would increase the possible error in time of flight velocity measurements[11] if wave propagation effects are present.

APPROXIMATE LOCATION
OF ARGON JET

$n_e = 1.0 \times 10^{15} \text{ cm}^{-3}$

0.5

1.5

1.0

2

3

3

30 20 10 6

r, cm

5

0

X, cm

ELECTRON DENSITY CONTOURS
J = 16 kA, $\dot{m}$ = 6 g/sec

FIGURE 3-17
AP 25·4845

47
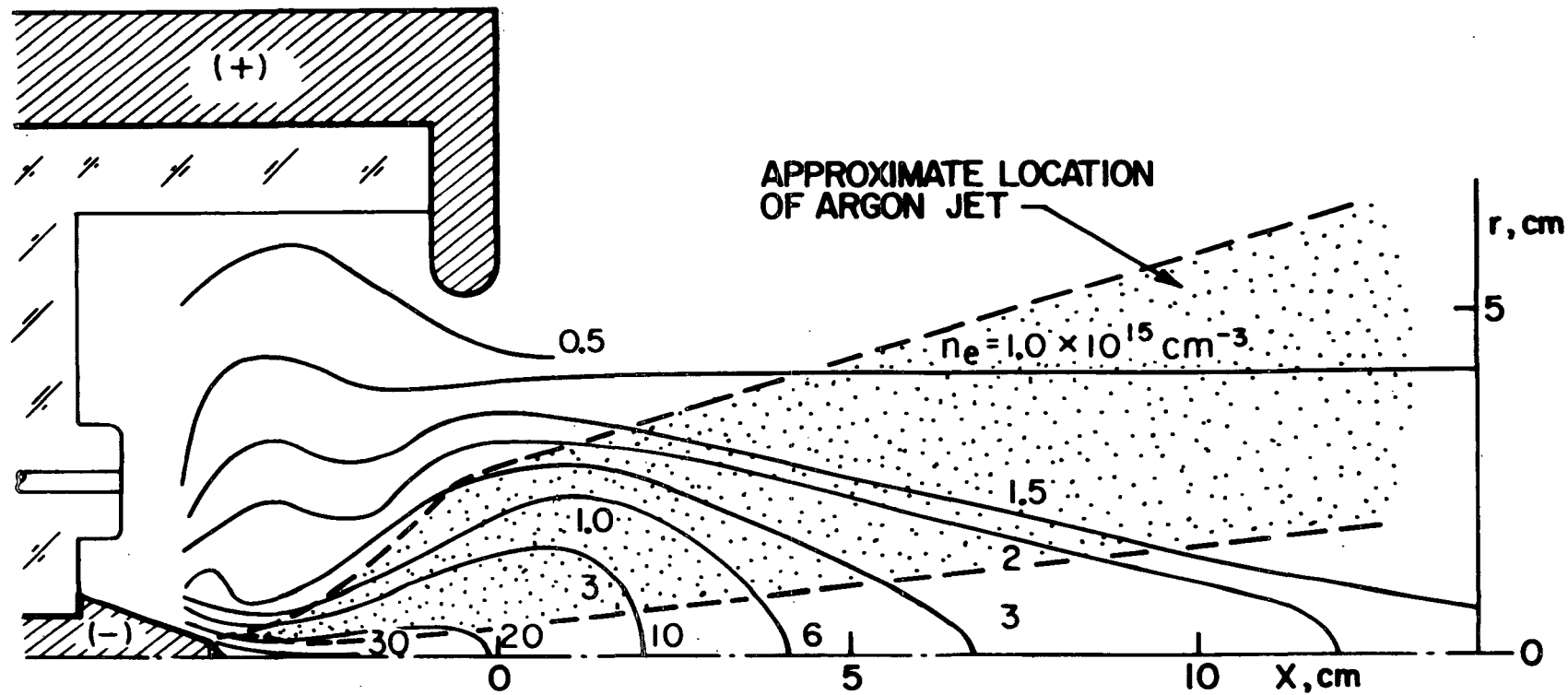
3-6 OPERATION AT OTHER CONDITIONS

Various investigators have examined the behaviour of the quasi-steady MPD accelerator over wide ranges of input mass flow, $\dot{m}$, and arc current, J.[4-7,10-13,30] Results suggest that a number of physical processes and terminal properties are functions of the parameter $J^2/\dot{m}$, rather than J and $\dot{m}$ separately. Malliaris et al,[30] have identified the so-called "matched" operating condition, $J^2/\dot{m} \approx 40$ kA^{2}sec/g, at which thruster performance is optimized. (The data presented so far in this dissertation were obtained at this condition.) Their results indicate that for the "starved" operating condition, $J^2/\dot{m} > 40$, insulator and electrode erosion is a problem, while at the "overfed" condition, $J^2/\dot{m} < 40$, some of the input mass bypasses the acceleration region. It seems reasonable, then, to expect the species structure of the exhaust plume to be dependent on the operating condition and be characterized by the quantity $J^2/\dot{m}$. To explore this possibility the arc was operated over a broad range of current and mass flow, and the resulting argon and ablated carbon exhaust flows photographed through the appropriate spectral filters. A strong effect on the species distribution has been confirmed. Some of the results are presented in Figs. 3-18 - 3-21 in the form of perspective and end views, at five different operating conditions: $J^2/\dot{m} \approx 10, 20, 40, 80, 160$. The matched condition, $J^2/\dot{m} \approx 40$ is included for reference. Figures 3-18 and 3-19 show that if the arc is overfed the argon jet structure becomes less distinct, each jet spreading azimuthally and towards the plume axis. At the most overfed condition shown (Fig. 3-18a and 3-19a) the discrete jet structure is no longer detectable, and the argon distribution is much more uniform than at the other conditions. When the discharge is starved the argon jet structure is clearly retained. At the most underfed condition shown (Figs. 3-18e and 3-19e) there appears to be some loss of definition of the jets, possible due to an increase in the continuum emission throughout the exhaust plume.

OVERFED

I·8961

10

a) 8 kA , 6 g/sec

I·8962

20
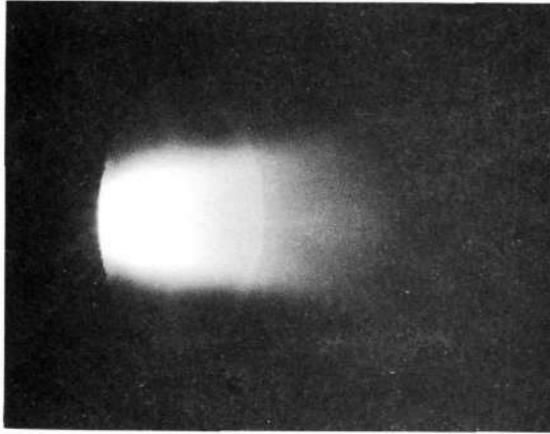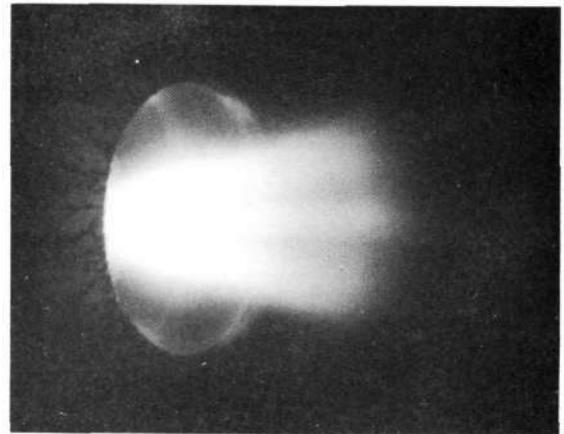
b) 16 kA , 12 g/sec

I·8960

MATCHED
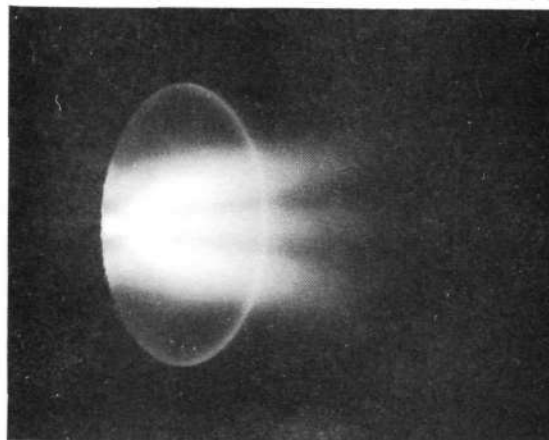
$J^2/\dot{m} = 40$

c) 16 kA , 6 g/sec
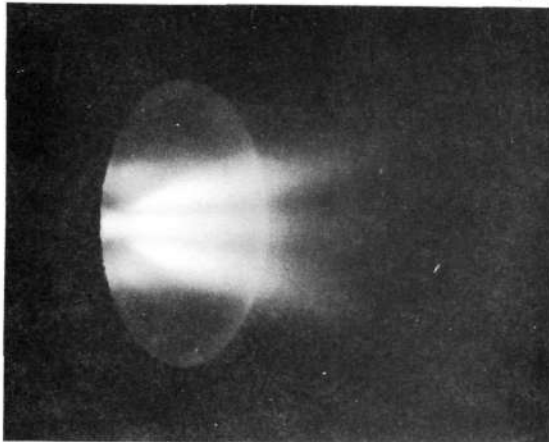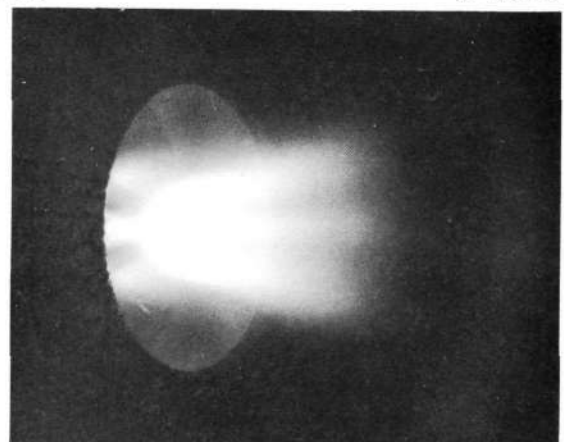
UNDERFED

I·8963

80

·d) 16 kA , 3 g/sec

I·8964

160

e) 32 kA , 6 g/sec

DISTRIBUTION OF AII AT VARIOUS OPERATING CONDITIONS.
PERSPECTIVE VIEW, 4880Å FILTER

FIGURE 3-18
AP 25·P 432

OVERFED

I·7785

I·7788

10

20

a) 8 kA , 6 g/sec

b) 16 kA , 12 g/sec

I·7783

MATCHED

$J^2/\dot{m} = 40$

c) 16 kA , 6 g/sec

UNDERFED

I·7789

I·7792

80

160

d) 16 kA , 3 g/sec

e) 32 kA , 6 g/sec
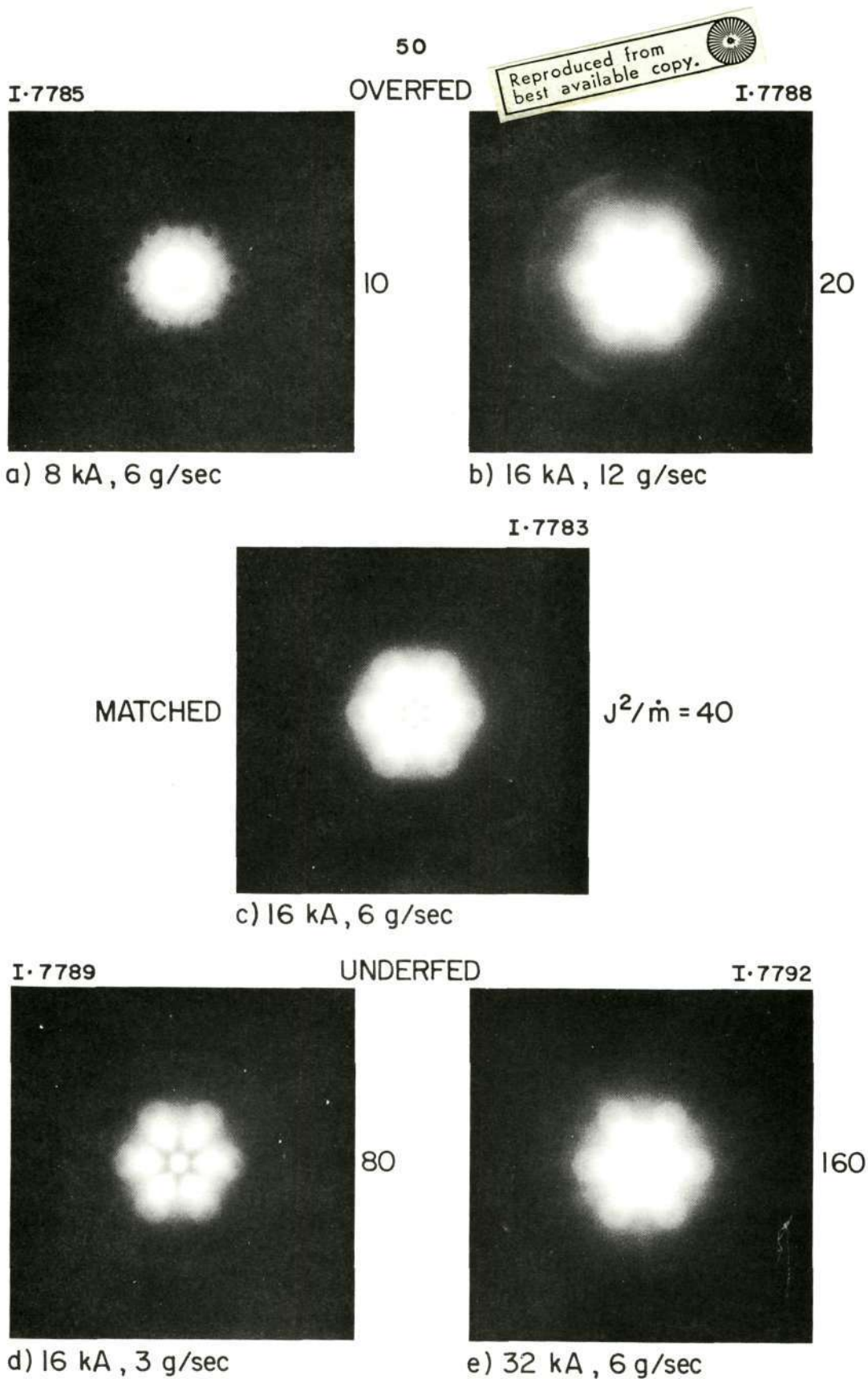
DISTRIBUTION OF AII AT VARIOUS OPERATING CONDITIONS.
END VIEW, 4880 Å FILTER

FIGURE 3-19

AP25·P433

The photographs at 5910 $\overset{o}{A}$, of ablated carbon in the discharge (Figs. 3-20 and 3-21), show complementary changes. Operation at overfed conditions decreases the amount of carbon in the exhaust indicating a reduction in the ablation rate. At starved conditions ablation is severe and carbon is found in abundance throughout the flow field. At any condition ablation appears most severe in the annular region between the cathode and the injectors. Bright narrow streaks visible in some of the perspective views are due to glowing particles ejected from the cathode.

In general, based on these and numerous other photographs, it can be said that under all but highly overfed conditions, i.e: for $J^2/\dot{m} > 10$, the exhaust plume of the MPD arc exhibits varying degrees of species separation. The tendency is for the species structure to be most sharply defined at matched or somewhat starved conditions. The occurrence of localized ablation of the Plexiglas back plate under even overfed conditions indicates that the overall operation of the arc cannot be strictly labeled "overfed", "matched", or "starved". Under a wide range of conditions the arc is apparently always starved in the regions between the injectors and between the cathode and the injectors. In addition, it does not appear possible to characterize all features of the plume structure solely by $J^2/\dot{m}$ over the entire possible range of this parameter. For example, the distribution of ablation products appears to be a weaker function of $\dot{m}$ at constant J than might be expected from a $J^2/\dot{m}$ scaling relationship. At highly overfed ($J^2/\dot{m} < 10$) and highly underfed ($J^2/\dot{m} > 160$) conditions the input mass flow appears to have no detectable effect on the rate of ablation or the impurity distribution in the exhaust. A further discussion of ablation phenomena is presented in Appendix A.

OVERFED

I·8246

I·8243

10
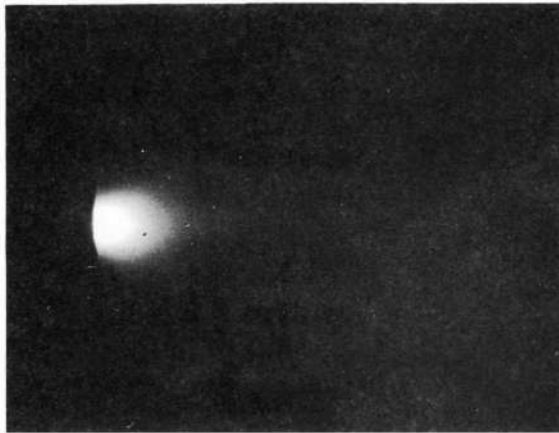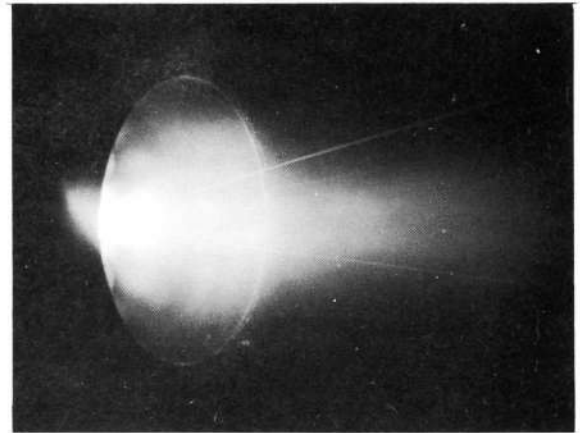
a) 8 kA , 6 g/sec

b) 16 kA , 12 g/sec

I·8237

MATCHED
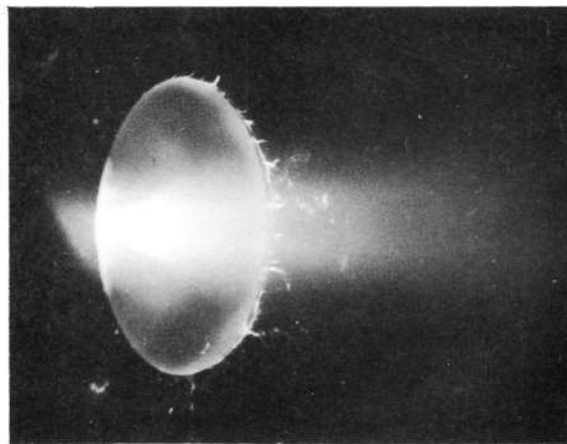
$J^2/\dot{m} = 40$

c) 16 kA , 6 g/sec

UNDERFED

I·8244

I·8247

80

160
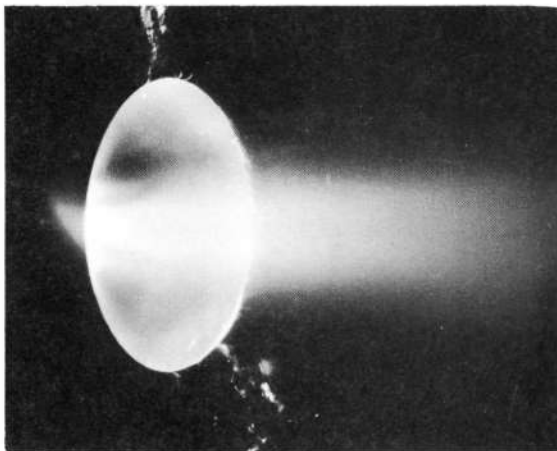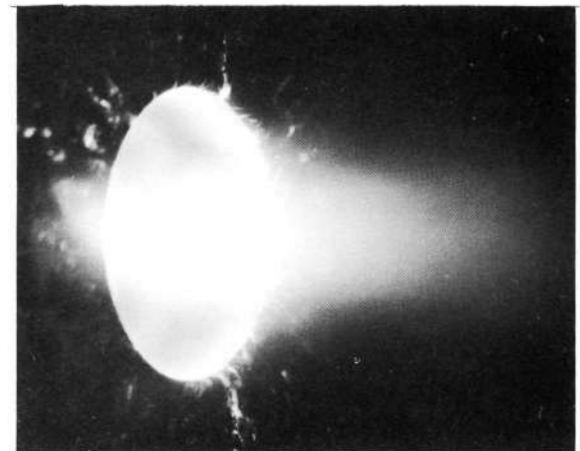
d) 16 kA , 3 g/sec

e) 32 kA , 6 g/sec

DISTRIBUTION OF CII AT VARIOUS OPERATING CONDITIONS.
PERSPECTIVE VIEW, 5910 Å FILTER

FIGURE 3-20

AP 25·P 434

OVERFED

I·8912

I·8913

10

20
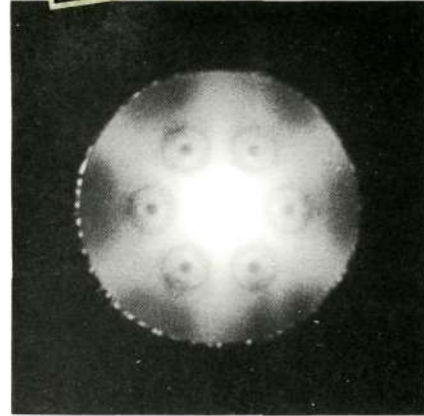
a) 8 kA , 6 g/sec

b) 16 kA , 12 g/sec

I·8910

MATCHED

$J^2/\dot{m} = 40$

c) 16 kA , 6 g/sec

UNDERFED

I·8915

I·8920

80

160
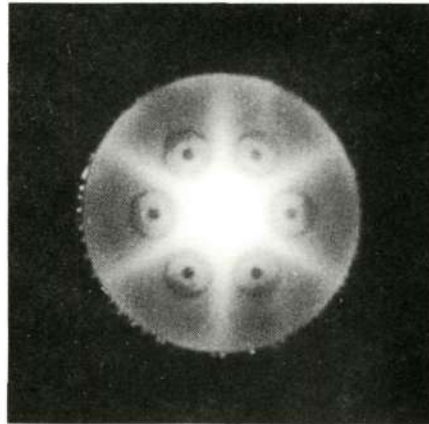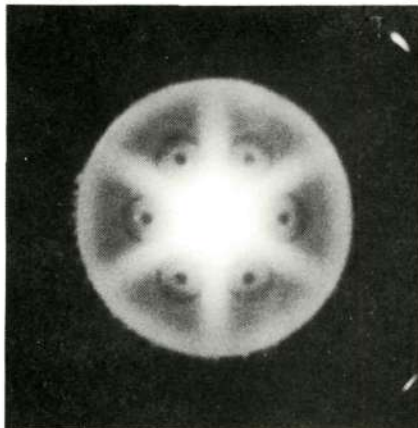
d) 16 kA , 3 g/sec
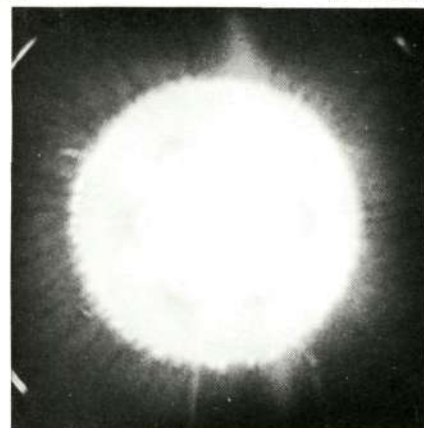
e) 32 kA , 6 g/sec

DISTRIBUTION OF CII & C_2 AT VARIOUS OPERATING CONDITIONS.
END VIEW, 5910 Å FILTER

FIGURE 3-21

AP 25·P 435

CHAPTER 4

VELOCITY AND TEMPERATURE MEASUREMENTS

4-1 INTRODUCTION

The complex radial and azimuthal species structure of
the exhaust flow of the MPD arc gives rise to difficulties
in the interpretation of velocity measurements obtained by
any of the usual probe techniques. In particular, it raises
additional questions about the previously published time-of-
flight velocity measurements[11] where it was assumed that
only argon existed in the exhaust so that velocities measured
along the plume axis could be ascribed to this specie. As
was shown in the previous chapter for all but very highly
overfed conditions (which are not of propulsion interest)
there is no argon on the plume axis, and consequently the
reported time-of-flight centerline velocities correspond
to the velocities of the ablation products, rather than of
the propellant. Additional complications in the interpre-
tation of time-of-flight velocity data arise if ion acous-
tic wave propagation effects are important. The species
inhomogeneity would lead to radial profiles of wave veloc-
ity which are sharply peaked on the centerline because of
the significantly lower atomic weight of the flow there.
Unfolding of wave and convective velocities would thus be
considerably complicated. These problems, typical of
measurement techniques which cannot distinguish between
atomic species, give added impetus to the application of
spectroscopic Doppler-shift techniques to measure propel-
lant velocities.

Spectroscopic methods have been used by a number of
other researchers in their investigation of various types
of steady self-field and applied field MPD arcs.[16,31-37]
Most of these devices were operated in low power regimes,

with propellants other than argon, and in certain cases[16,31] under relatively high environmental pressures. In all but two of these investigations[16,31] no attempt was made to reduce the spectroscopic data to local flow properties. The results of these studies, although interesting in their own right, are only of academic interest in the present context. Spectroscopic measurements on quasi-steady high power MPD arcs have also been made.[12,18,30] Of particular interest for comparison with the present work are the results of Malliaris et al,[12,30] obtained on an accelerator quite similar to the one investigated here.

This chapter is concerned with time-resolved spectroscopic velocity and temperature measurements of singly ionized argon, the dominant radiative propellant specie in the exhaust of the quasi-steady MPD arc. Unfortunately, the lack of cylindrical symmetry of the propellant in the exhaust flow precludes the reduction of Doppler-shift measurements to purely local values by Abel inversion techniques.[16,25,38] However, it will be seen that the rather sharp collimation of the argon jets does allow deduction of reliable values of average velocity and temperature as functions of axial distance within the individual argon jets.

4-2   EXPERIMENTAL APPARATUS

Constraints on Spectrometer Resolution

The resolving power of the spectrometer used in the velocity and temperature measurements must be sufficient to allow clear separation of Doppler shifted line components and also be such that the instrumental broadening is less than the expected Doppler line widths. The order of magnitude of the expected line shifts and widths is estimated below.

If an emitter of radiation moves with a velocity v relative to an observer, then a wavelength λ will be observed

such that[39]

$$\frac{\lambda}{\lambda_0} = \frac{\sqrt{1-\beta^2}}{1-\beta\cos\theta}$$

where $\beta = v/c$, c is the speed of light, θ is the angle between the velocity vector and the line of sight, and λ_0 is the wavelength which would be observed if the emitter were at rest. For non-relativistic velocities, i.e., if $\beta \ll 1$, the following approximation is valid:

$$\Delta\lambda = \frac{\lambda v}{c}\cos\theta$$

where $\Delta\lambda = \lambda_0 - \lambda \ll \lambda$ is the Doppler shift. Velocities of the order of 10^4 m/sec, which are characteristic of MPD devices, lead to Doppler shifts of about $0.1 - 0.2$ Å in the visible spectrum. The Doppler broadening, $\Delta\lambda_D$, of spectral lines due to the random thermal motions of the radiating particles is given by[40]

$$\Delta\lambda_D = 7.16 \times 10^{-7} \lambda \left(\frac{T}{M}\right)^{1/2}$$

where λ is the wavelength at line center of the spectral line, and T and M are respectively the temperature (°K) and molecular weight of the radiating particle. (A more detailed discussion of this relation is given in section 4-4.) Argon temperatures of the order of 10^4 °K ($\sim$ 1eV), which are usually found in plasma accelerators, lead to line widths of the order of 0.05 Å.

The high resolving power necessary to detect Doppler shifts and line widths of the magnitudes estimated above can be achieved with a Fabry-Perot interferometer.[24, 41-45] A review of the theory of this device and of the factors influencing its performance is presented in Appendix B for the benefit of the reader who may not be familiar with its principles. Additional details can be found in the literature.[24,41-45]

The Fabry-Perot interferometer is not only capable of much higher resolution than a prism or grating spectrograph, but also has a much higher luminosity. Furthermore, it is simple in principle, readily adaptable to time-resolved operation and is relatively inexpensive.

The Fabry-Perot Spectrometer System

The interferometer and supporting optics used in the present study are shown in schematic and photograph form in Figs. 4-1 - 4-3. The Fabry-Perot (henceforth denoted F.P.) is a commercial unit manufactured by Coherent Optics, Inc. with interferometer plates by Perkin-Elmer Corp. The plates, 38 mm diam x 9.5 mm thick are made of fused silica and are polished flat to λ /200 ($\lambda \approx 5000$ $\overset{O}{A}$). Their reflecting coatings, which consist of multilayer dielectric films, have a reflectivity of 95 $\pm$ 1% in the spectral range of 4600 - 5400 $\overset{O}{A}$. These coatings reduce the effective surface flatness to about $\lambda/100$.[46] (The reflectivity finesse F_R and the flatness limited finesse F_D (both defined in Appendix B, section B-3) are thus approximately equal ($F_R \approx F_D \approx 50$) so that the effective instrumental finesse F_e and transmission factor $\mathcal{T}_e$ are optimized with respect to each other.) One of the interferometer plates is fastened to one end of a hollow tubular piezoelectric transducer. Application of a linear ramp voltage to the transducer causes it to translate the plate perpendicular to its surface so that the spacing between the interferometer plates changes linearly with time. This effects a linear change in the transmission wavelength of the F.P. causing it to act as a tuneable wavelength filter which scans a region of the spectrum. (Appendix B, section B-2). The other stationary plate of the F.P. is held in a gimballed mount which can be adjusted by means of micrometer screws and piezoelectric transducers to render the plates parallel.

The use of the F.P. as a spectrometer requires supporting optical elements and electronic equipment to collimate light

FABRY-PEROT SPECTROMETER SYSTEM

LEGEND

M_1	Micrometer Adjusted Mirror
M_2 M_3	Adjustable Mirrors
L_1	Objective Lens (127 cm F.L.)
L_2 L_3	Beam Reducing Lenses
L_4	Fringe Projection Lens
L_5	Collimating Lens
L_6 L_7	Laser Beam Expanding Lenses
BS	Clear Glass Beam Splitter
FPI	Fabry-Perot Interferometer
P_H	Pinhole (0.08 cm Dia.)
P_L	Polarizer
P_R	Right Angle Prism
NDF	Neutral Density Filters
IF	Interference Filter 4880 Å (10 Å B.W.)
ID_1 ID_2 ID_3	Iris Diaphragms
P.M.	Photomultiplier Tube (RCA 1P28)
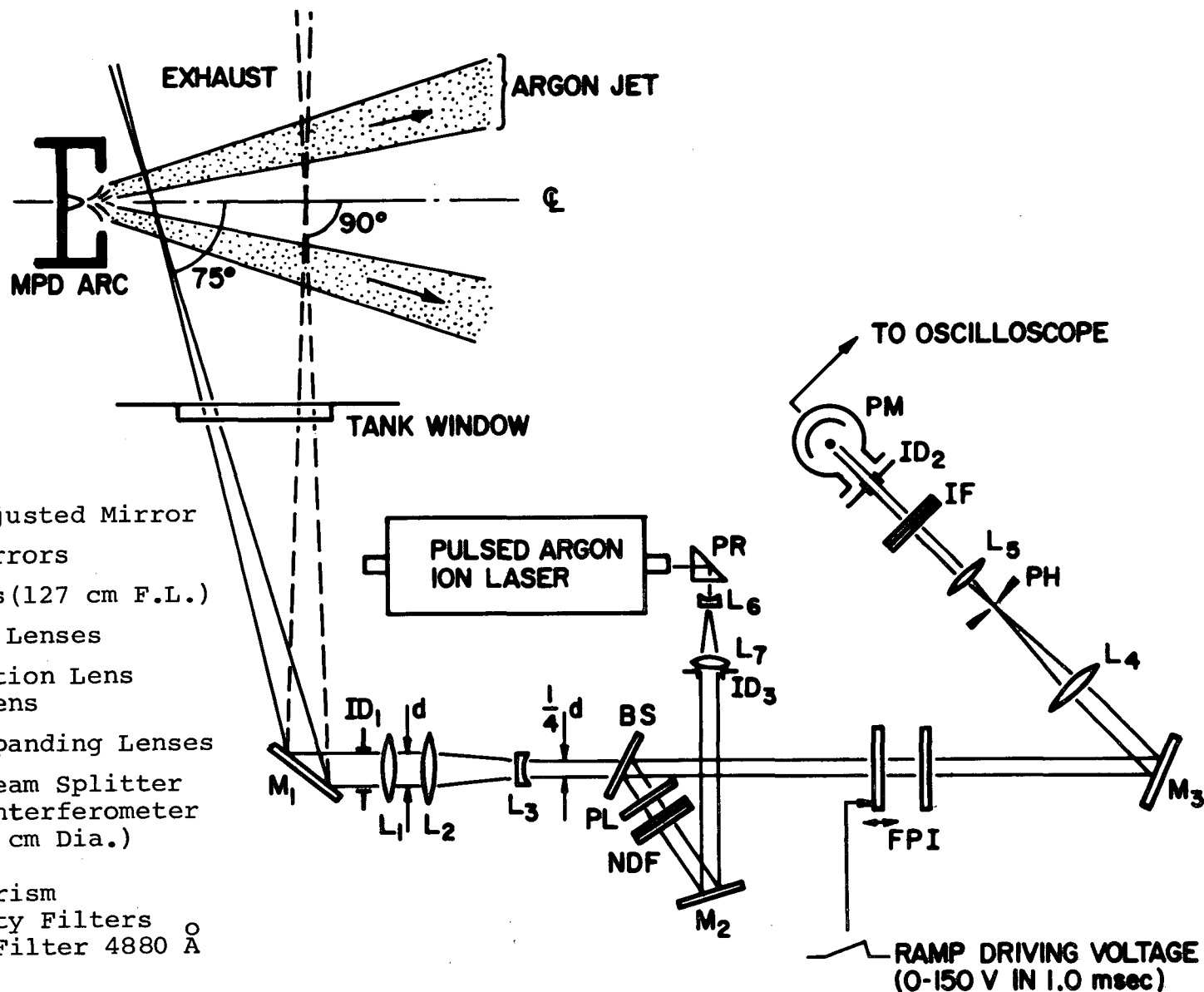
FIGURE 4-1
AP25.4805

58

FIGURE 4-2
AP25·P·471
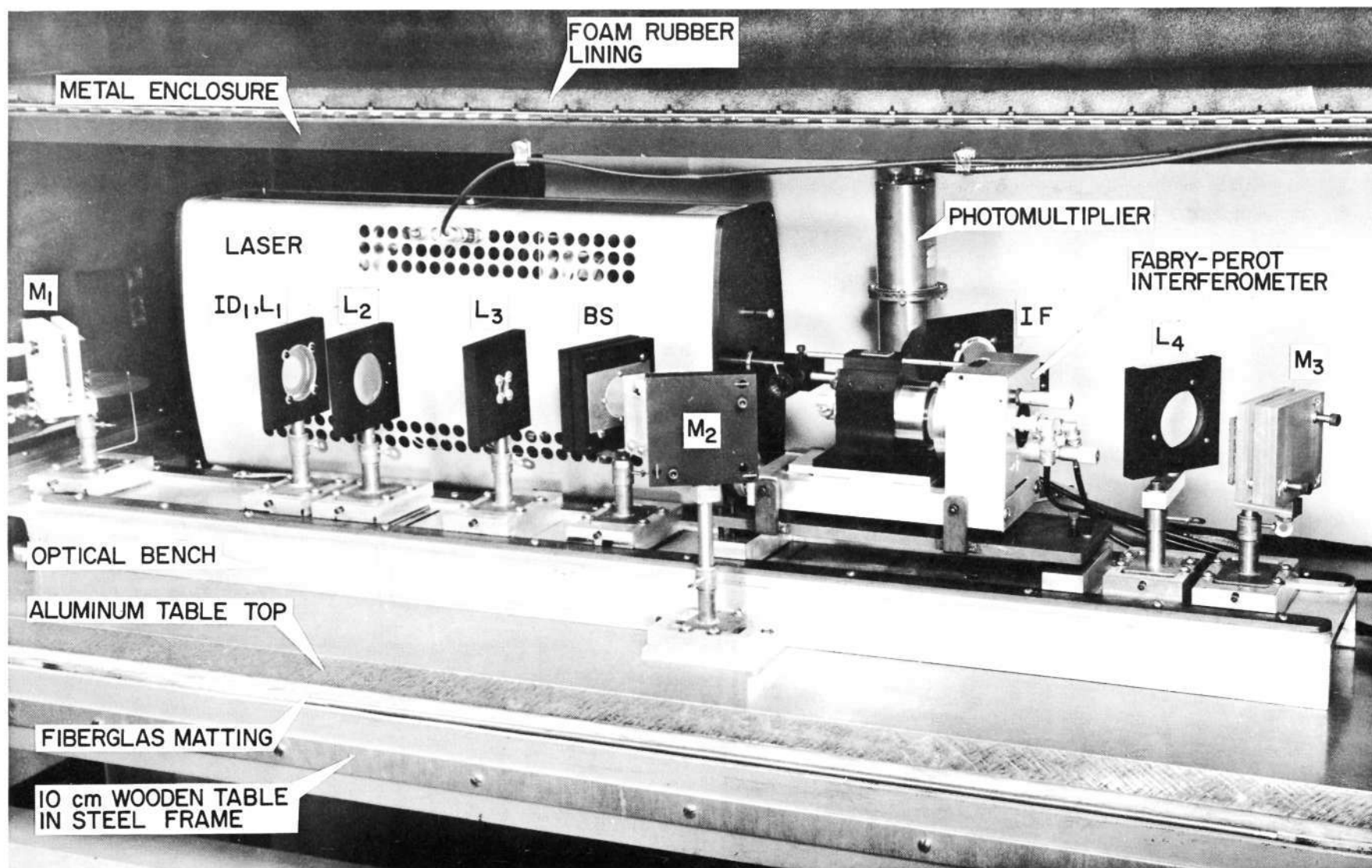
Labels in figure:

METAL ENCLOSURE

FOAM RUBBER LINING

LASER

PHOTOMULTIPLIER

FABRY-PEROT INTERFEROMETER

M_1

ID_1, L_1

L_2

L_3

BS

M_2

IF

L_4

M_3

OPTICAL BENCH

ALUMINUM TABLE TOP

FIBERGLAS MATTING

10 cm WOODEN TABLE IN STEEL FRAME

VIEW OF THE FABRY-PEROT SPECTROMETER SYSTEM

LASER

LASER BEAM EXPANDER
(L_6, L_7, ID_3)

L_3

BEAM SPLITTER

POLARIZER

NEUTRAL DENSITY FILTERS

PHOTOMULTIPLIER

INTERFERENCE FILTER

L_5

PINHOLE

M_2

FABRY-PEROT INTERFEROMETER

L_4

M_3

FIGURE 4-3
AP 25·P·472

60
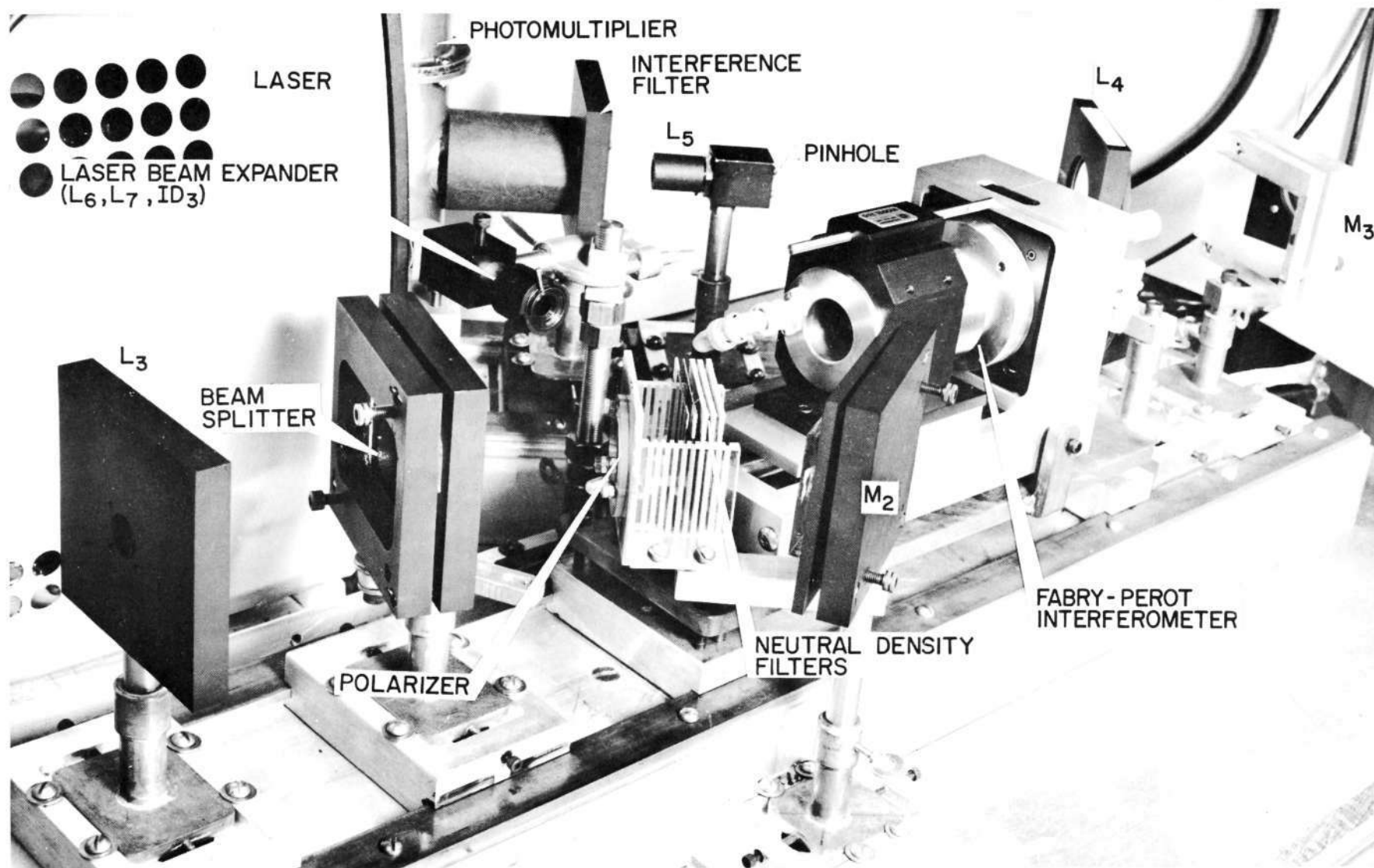
from the plasma under investigation and detect the F.P. output (Figs. 4-1 - 4-3). Light from the discharge is directed by the mirror M_1 through an adjustable diaphragm to the objective lens L_1 (50 mm diam x 1270 mm f.l.)whose focal point lies on the discharge axis. Mirror M_1 can be adjusted about both horizontal and vertical axes by means of micrometer screws to obtain the desired line-of-sight through the exhaust plume. Lenses L_2 (50 mm diam x 190 mm f.l.) and L_3 (18 mm diam x-47 mm f.l.) reduce the collimated incoming beam diameter by a factor of four so that only the central portion ($\sim$1 cm diam) of the F.P. plates is used. (This tends to minimize the effects of plate distortion caused by accelerations of the moving plate during a scan.) Mirror M_3 directs the output of the interferometer to the lens L_4 (50 mm diam x 172 mm f.l.) which focuses the center of the scanning fringe pattern on the 0.8 mm diam pinhole, PH. The size of this aperture is chosen so that its finesse F_P matches the plate flatness finesse F_D and the reflectivity finesse, F_R, as explained in Appendix B. Lens L_5 (12.5 mm diam x 65 mm f.l.) collimates the light from the pinhole for passage through a 4880 $\overset{o}{A}$, 10 $\overset{o}{A}$ bandwidth interference filter, IF, which selects the 4880 $\overset{o}{A}$ line of AII for investigation. An RCA 1P28 photomultiplier tube detects the scanned spectrum. A TRW Model 71-BR pulsed argon ion laser (pulse width: 40 μsec) provides the reference wavelength at 4879.9 $\overset{o}{A}$ against which Doppler shifts are measured. (The reference wavelength cannot be obtained from the discharge at right angles to the flow velocity, as is usually done, for reasons which will become clear later.) The laser output is expanded and collimated by lens system L_6-L_7 (5 mm diam x - 4 mm f.l. and 19 mm diam x 67 mm f.l.) and superimposed on the collimated discharge light by means of mirror M_2 and a clear flat glass beam splitter, BS. The expanded laser beam diameter is adjusted by means of an iris diaphragm, ID_3, to match the diameter of the discharge light beam. A set of polarizers and neutral density filters is used to control the laser intensity reaching the photodetector.

All the components of this system are mounted on an optical bench made from heavy aluminum channel stock which is securely bolted to a 2.5 cm thick x 152 cm long x 61 cm wide aluminum plate. The latter is placed atop a 10 cm thick plywood slab of the same length and width which is covered with a 12.5 mm thick layer of fiberglass vibration isolation matting. The wooden slab is cradled in a steel frame which in turn rests atop a heavy angle-steel framework. Leveling is accomplished by means of four large diameter screws which support the frame around the wood base. The entire assembly sits atop four 10 cm x 10 cm x 5 cm fiberglass vibration isolating pads, which are very effective in preventing floor vibrations from reaching the interferometer. The optical system atop this optical table is enclosed in a 1.5 mm thick aluminum box, lined with a 2.5 cm layer of black foam rubber, which keeps air currents, sound vibrations and extraneous light from the interferometer and other components.

Method of Operation

Proper synchronization of the F.P. scan and laser reference pulse with the discharge current pulse is a crucial element in the operation of the spectrometer system described above. A schematic of the electronic synchronization and recording system is shown in Fig. 4-4. The sequence of events is sketched in Fig. 4-5. Initiation of the discharge is sensed by a Rogowski coil [4] embedded in the anode return cylinder. The resulting signal, triggers time base A of the Tektronix 555 oscilloscope. This time base, which records the discharge current history, completes its sweep in 1 msec. The sawtooth voltage (0-150 V in 1 msec) used in the horizontal sweep of this time base is applied to the piezoelectric translator attached to the moving mirror of the F.P., which as a result moves a distance of about 1.7 μ towards the stationary mirror, for a scan of about three free spectral ranges in the middle of the visible spectrum. Ideally the moving mirror should travel at constant velocity from the beginning of the F.P. scan at discharge initiation to the end
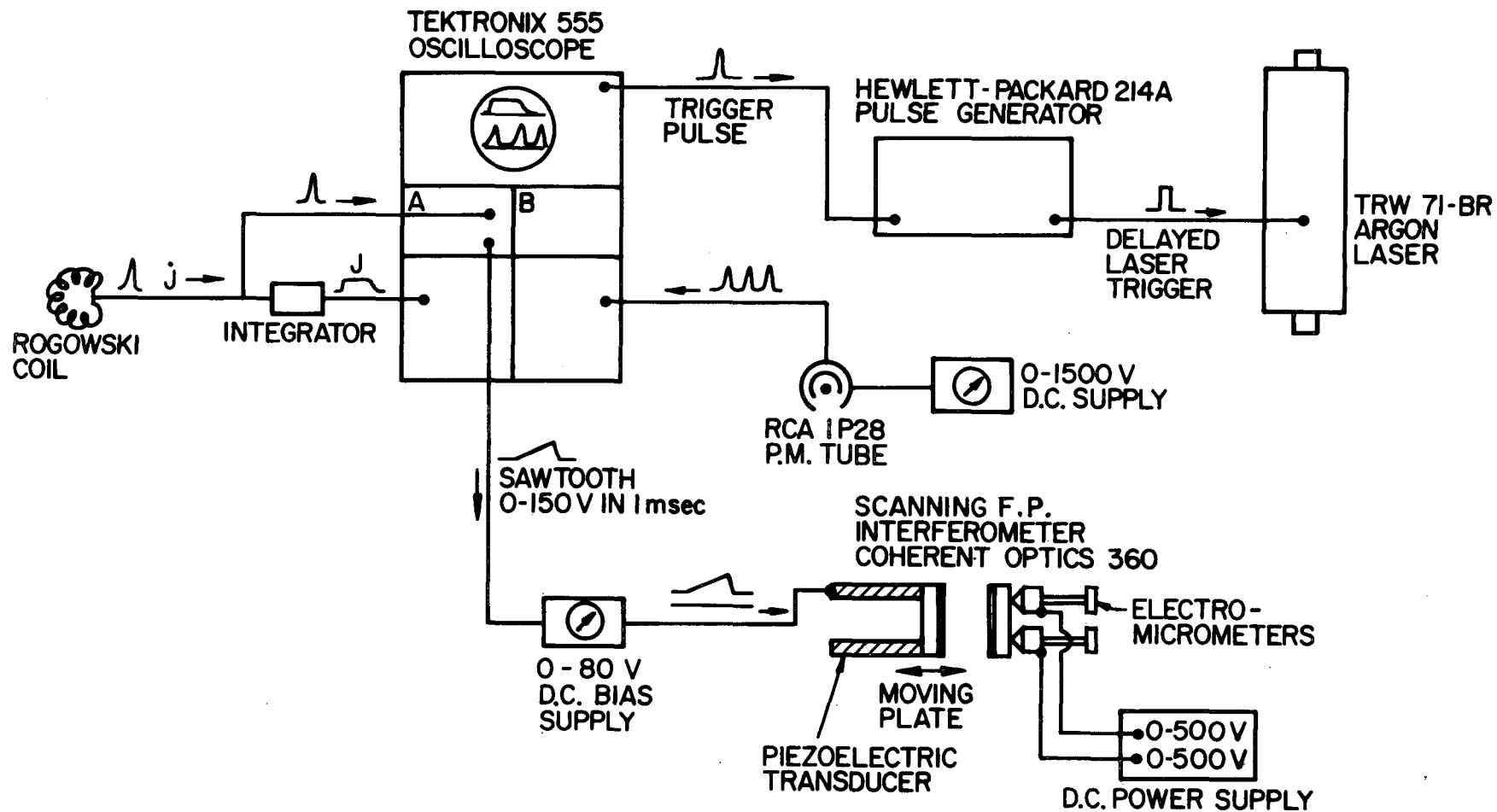
ELECTRICAL SCHEMATIC OF FABRY-PEROT SPECTROMETER SYSTEM

FIGURE 4-4
AP 25-4846

63

a) DISCHARGE CURRENT, J (kA)

b) RAMP VOLTAGE TO F.P. — 150 V — D.C. BIAS (VARIABLE)

c) F.P. PLATE MOTION |Δd| — --- IDEAL PLATE MOTION — ACTUAL PLATE MOTION

d) LASER PULSE — VARIABLE DELAY — 40 μsec

e) WAVELENGTH SCAN — Δλ — LASER LINE — LINE FROM DISCHARGE — FREE SPECTRAL RANGE — DISPLAYED ON OSCILLOSCOPE TIME BASE B — λ — t* = 0.45 msec
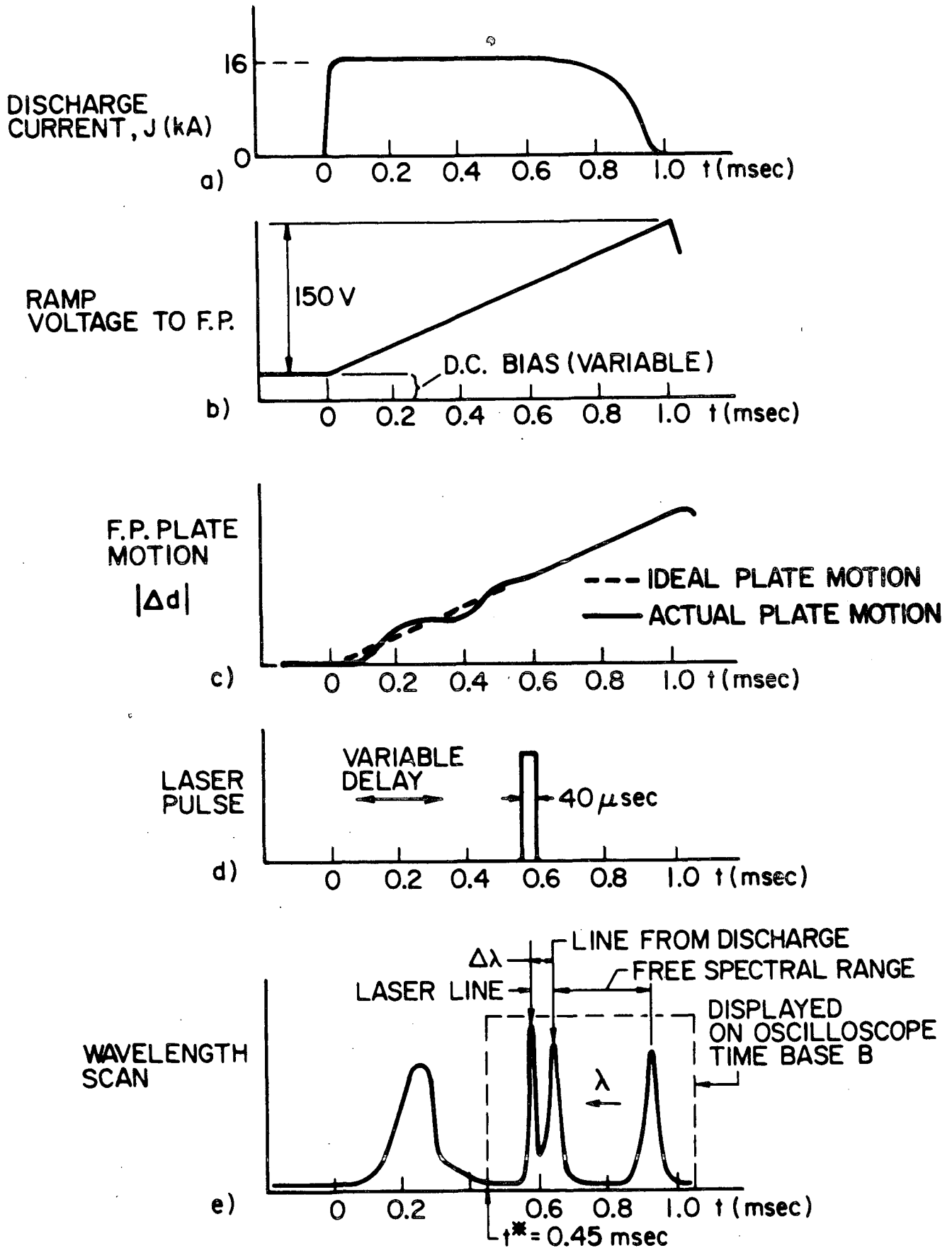
SEQUENCE OF EVENTS IN
FABRY-PEROT SCAN

FIGURE 4-5
AP25·4847

of the ramp voltage 1 msec later, so that the plate separation, and thus the transmitted wavelength is a linear function of time. However, the piezoelectric transducer and the moving plate have finite dimensions and mass so that the plate motion is not linear; rather it has superimposed on it an oscillatory component as shown in Fig. 4-5b. This is tantamount to a loss of effective F.P. finesse. Fortunately the oscillations damp out quickly, so that during the second half of the scan the plate motion is essentially linear in time. Another result of the initial acceleration is a bending or bowing of the moving plate which seriously degrades the plate flatness and thus the overall finesse of the F.P. during the first 100 μsec of the scan. Some bowing appears to exist throughout the scan, because the experimentally measured overall finesse is always somewhat less when the instrument is scanned at the present rate of 1 scan/msec, than if it is scanned one or two orders of magnitude more slowly. Results indicate that during the second half of the 1 msec scan the plate flatness is degraded to approximately $\lambda/90$ from the stationary value of $\lambda/100$, which is quite tolerable.

Superimposed on the ramp driving voltage is a variable D.C. bias obtained from a battery operated power supply. The purpose of this bias is to provide a fine adjustment of the initial F.P. plate separation and thus permit proper centering of the transmission peaks on the cathode ray tube of the oscilloscope. The wavelength scan detected by the photomultiplier tube is exhibited on time base B of the oscilloscope, swept at twice the rate of time base A (i.e: in 0.5 msec) but delayed with respect to it by 0.45 msec. In this manner only the second half of the F.P. scan is displayed. The D.C. bias to the F.P. is adjusted so that the spectral line is swept out twice in one sweep of time base B. (Fig. 4-5d). With the free spectral range of 0.78 $\overset{o}{A}$ used in the present work a time resolution of 0.003$\overset{o}{A}$/μsec at about 5000 $\overset{o}{A}$ results. As will be seen this corresponds to the scan of a typical spectral line in about 50 μsec.

The laser used as a wavelength reference can produce only a single pulse 40 μsec wide during the 1 msec scan of the interferometer: thus, it must be triggered at a suitable point in the scan such that the plate separation is correct for transmission of the laser wavelength (4879.9 $\overset{O}{A}$), as illustrated in Fig. 4-5d. Since only the second half of the F.P. scan is recorded, the laser pulse must be delayed at least 450 μsec with respect to discharge initiation. The proper delay is obtained by means of a Hewlett-Packard Model 214A pulse delay generator which is triggered by the initiation of the sweep of time base A on the oscilloscope.

The overall finesse of the Fabry-Perot spectrometer system, when operated as described above, has been measured to be $F_T = 25$. Stability of the instrument against external influences is very good, except when the room temperature is not constant. Before any data are recorded the various pieces of electronic equipment are allowed to warm up for at least two hours, or until the interferometer displays a drift stability of more than 5 minutes. On particularly good days stabilities as long as 30 min. have been observed. Clearly, a constant temperature enclosure for the interferometer would greatly increase its stability.

4-3 VELOCITY AND INTENSITY MEASUREMENTS

By proper choice of lines of sight through the exhaust plume of the MPD accelerator, a variety of quantitative measurements may be carried out by means of the system described in the previous section. The spatial location of the argon jets can be accurately mapped by recording line intensities as a function of distance both parallel and perpendicular to the discharge axis. Doppler-shift velocity measurements obtained at two sets of lines of sight at two different angles to the discharge axis can yield information not only on the development of average velocity along each jet, but also on the variation of average jet flow angle. Finally, argon ion temperatures can be obtained from the Doppler broadening of spectral lines. All measurements reported here are confined to the

"matched" operating condition of $J = 16kA$, and $\dot{m} = 6$ g/sec.

Surveys at 90° Lines of Sight

Extensive radial surveys were carried out at four axial positions in the exhaust plume: 4.6, 10.9, 15.9 and 30.6 cm from the anode exit plane, with the line of sight perpendicular to the discharge axis. Mirror M_1 was adjusted to raise or lower the line of sight by intervals of 0.4 cm at the plane of the plume axis. At each vertical position the scan of the 4880 Å AII spectral line was recorded from four to twelve times, each time during a separate discharge. The number of line scans recorded at a given position was dictated by the reproducibility of the observed line profile. In general, higher reproducibility was obtained at the locations closer to the anode and near the centerline.

A typical result, obtained with the line of sight level with the axis, 10.9 cm from the anode plane is shown in Fig. 4-6. The upper trace is the discharge current signature and the lower trace is the scan of the 4880 Å line of AII by the Fabry-Perot interferometer. (Two scans of the line during the second half of the current pulse are displayed, as discussed in section 4-2.) The spectral line exhibits the characteristic Doppler split resulting from the opposed radial velocity components of the two argon jets intersected by the line of sight. For clarity the laser reference line was not superimposed simultaneously, but was recorded separately immediately prior to the discharge. (It is the small peak midway between the two components from the discharge.) It was ascertained that the interferometer did not drift in the time between the two records. It can be seen that the two Doppler-shifted line components from the argon jets are symmetrical about the laser line, attesting to the equality of the radial components of velocity in the two jets. The second small laser line at the position of the next scan of the discharge line at the right of the oscillogram was recorded to serve as a relative calibration of the free spectral range of the interferometer.
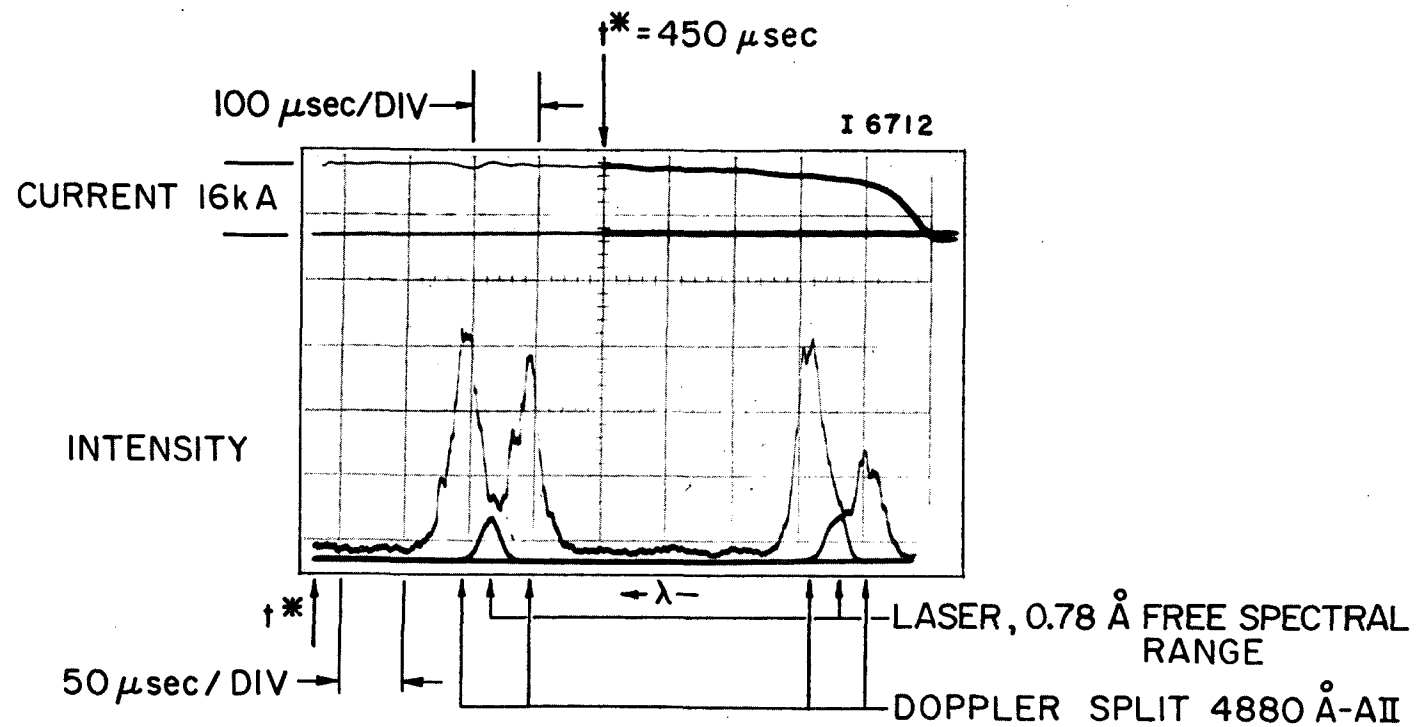
THE 4880 Å AII LINE AT 10.9 cm FROM ANODE

FIGURE 4-6
AP 25·P 395

(An absolute calibration of the free spectral range was carried out with the help of the Steinheil prism spectrograph and a high pressure mercury light source, according to a technique described by Born and Wolf[24]. The free spectral range was set to 0.78 Å for the bulk of the experiments described here. It could not be made smaller because of the constraints imposed by the 40 μsec duration of the laser pulse.)

Figure 4-7 shows a schematic of the exhaust plume with the location of the 90° lines of sight used in the survey and typical resulting line profiles. Note how the Doppler split increases with distance from the chamber exit plane, indicating accelerating radial flow in the argon jets. The blue-shifted components corresponding to the near jet appear always to have a smaller intensity than the red-shifted component. The cause for this was later found to be due to a slight azimuthal misalignment of the MPD accelerator in the vacuum tank, so that the two "central" argon jets were actually somewhat tilted out of the horizontal plane. The error in measured velocities resulting from this is insignificant. The radial velocity components of the argon jets are shown plotted against axial distance in Fig. 4-8. Each error bar contains the range of velocities obtained from observed Doppler splits of four to twelve spectral line scans at each horizontal line of sight. Because the widths of the spectral line components are narrow it can be assumed that the spread of radial velocity in each jet is small so that the curve shown is a good representation of the development of the average radial velocity components in each jet. It can be seen that the bulk of the acceleration occurs within about one and a half anode orifice diameters (15 cm) from the chamber exit plane.

Figure 4-9 displays the shape of the 4880 Å spectral line with increasing distance above the axis in the vertical plane 15.9 cm from the chamber exit. It can be seen that the two Doppler-split line components come closer together and eventually merge as the optical line of sight approaches the outer
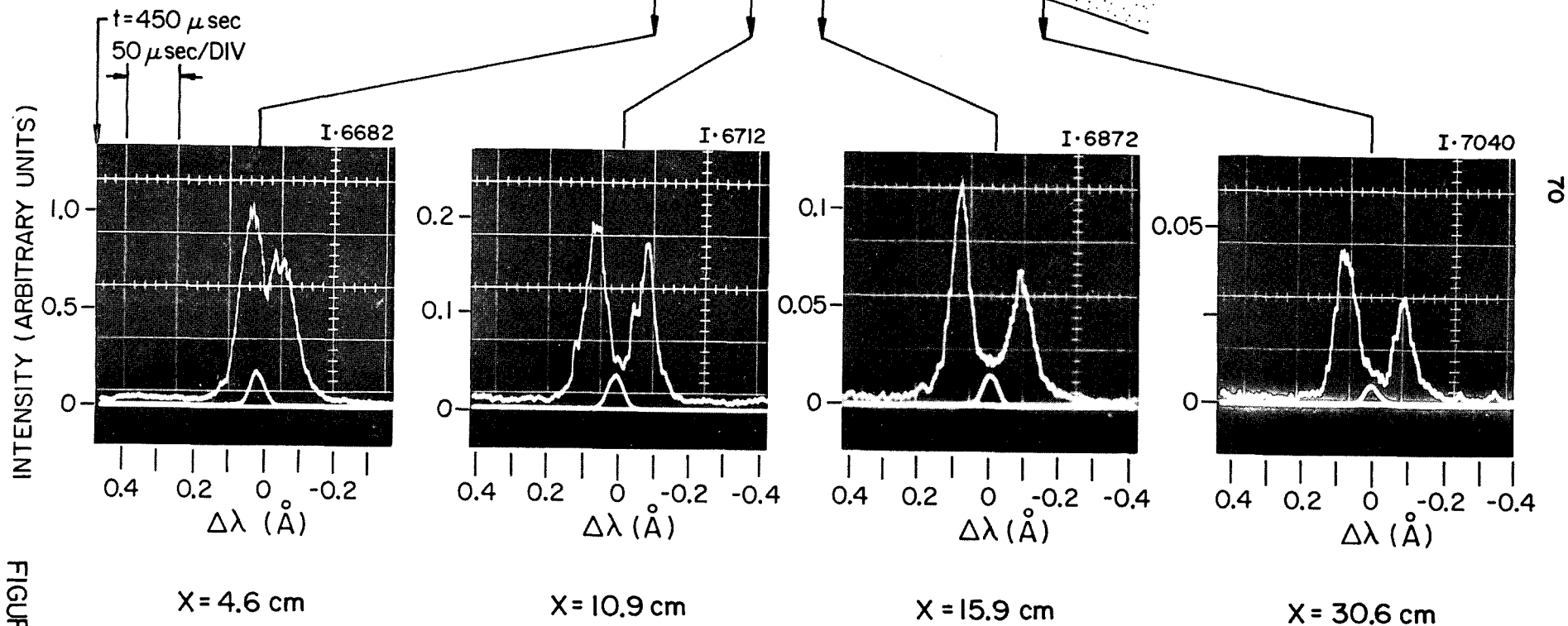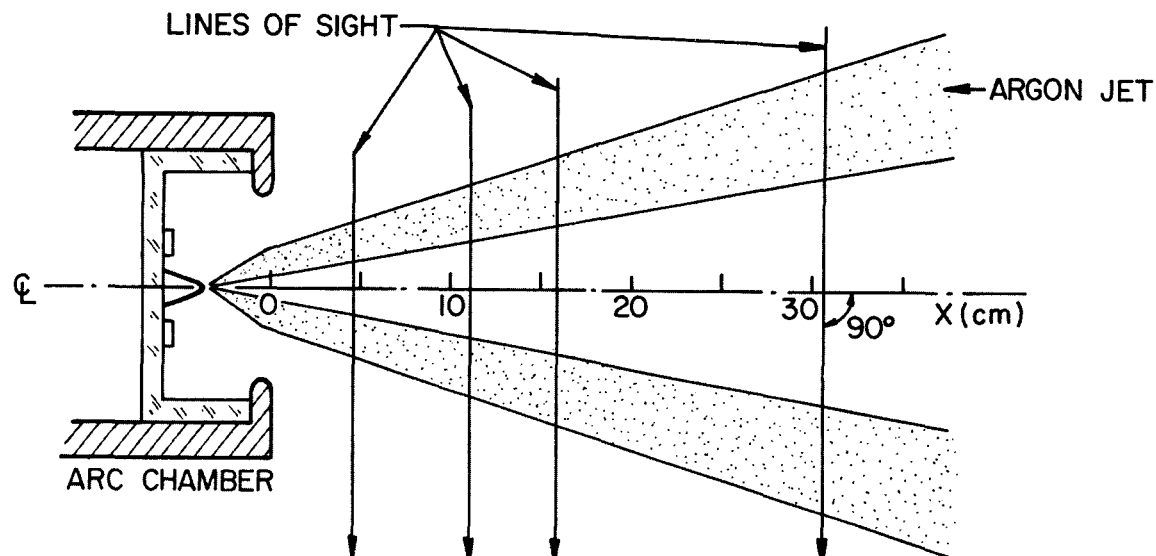
TYPICAL 4880Å LINE PROFILES AT VARIOUS AXIAL STATIONS

FIGURE 4-7
AP25·P·473

70
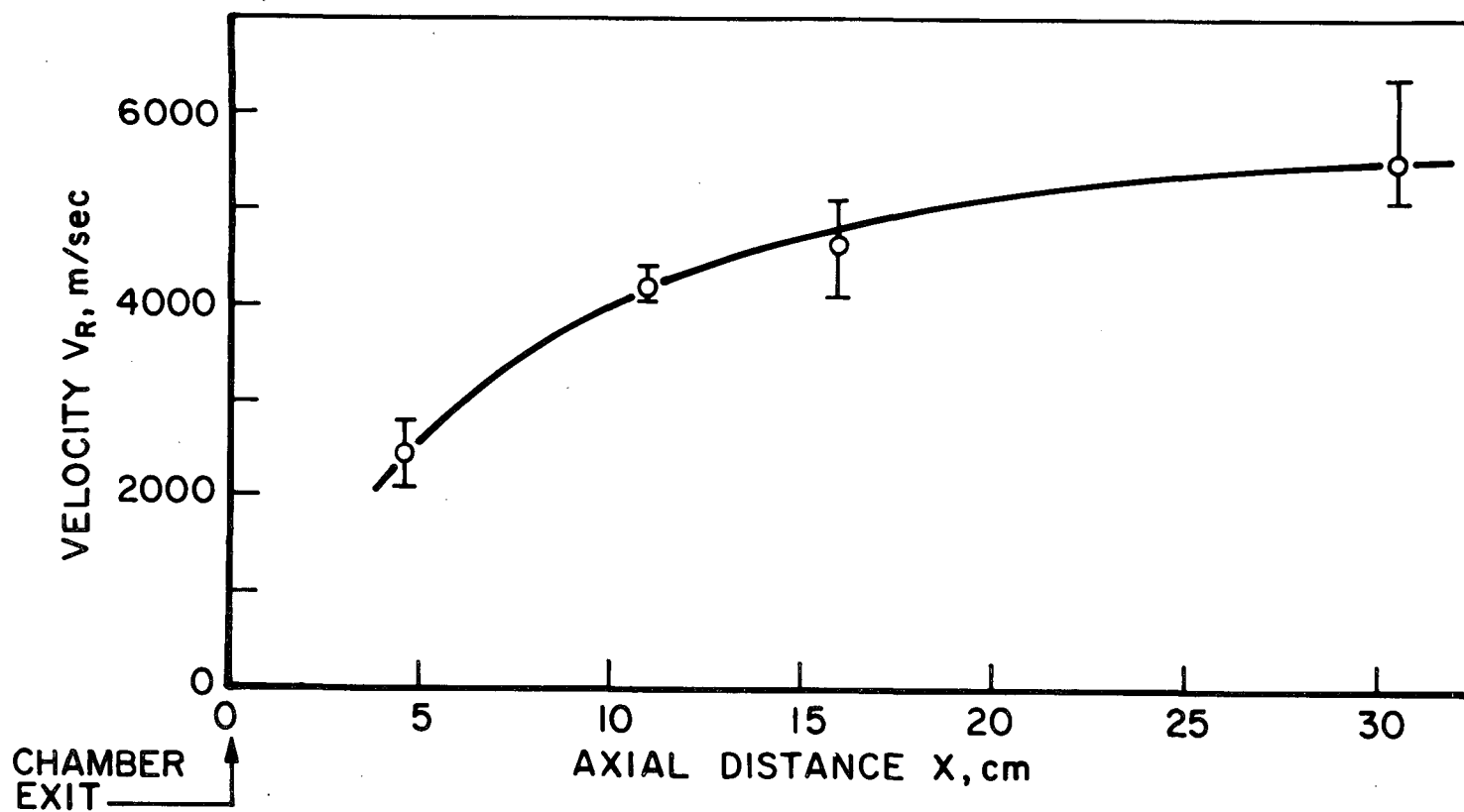
FIGURE 4-8
AP 25·4806

DEVELOPMENT OF A II RADIAL VELOCITY

I·6872

a) Y = 0 cm

I·6956

b) Y = 1.55 cm

I·6972

c) Y = 3.10 cm

I·6984

d) Y = 4.72 cm

I·6997

e) Y = 6.42 cm

I·7002

f) Y = 8.12 cm

I·7005
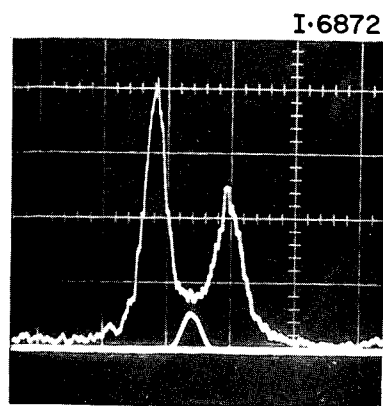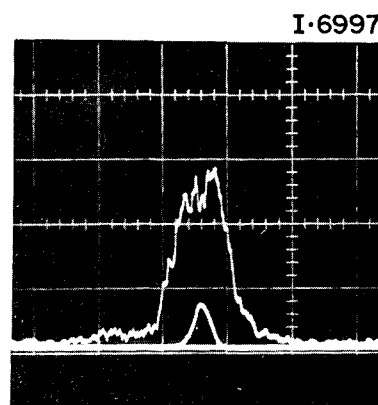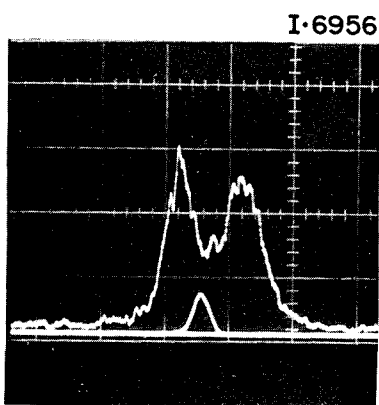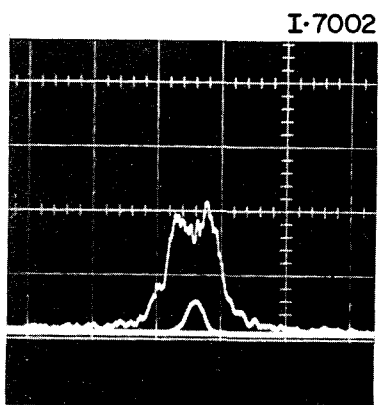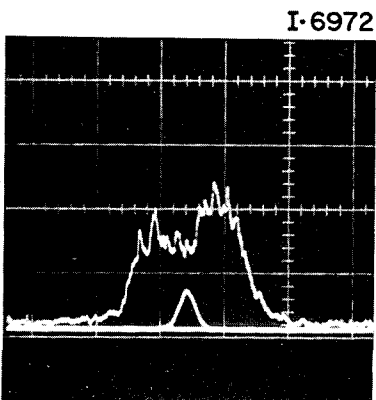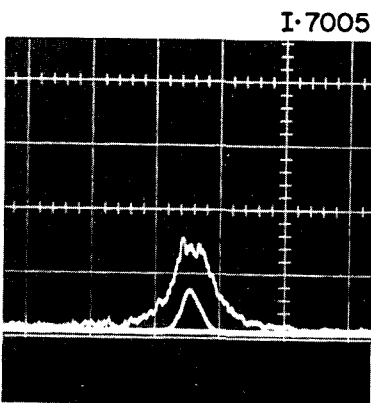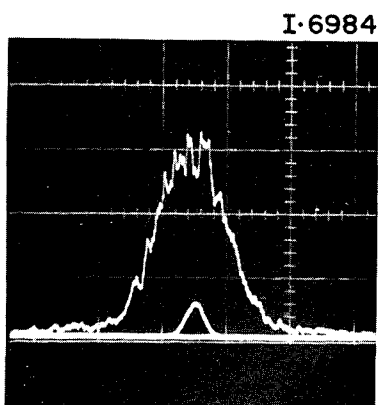
g) Y = 9.83 cm

0 .1 .2 Å

WAVELENGTH SCALE

VARIATION OF 4880Å AII
LINE SHAPE WITH HEIGHT
OF LINE OF SIGHT ABOVE
DISCHARGE AXIS AT X = 15.9 cm

FIGURE 4-9
AP 25 · P · 474

edges of the exhaust plume. This behaviour is typical of that observed at the other three axial stations and indicates the expected decrease in the components of radial velocity projected along the line of sight. There is also a noticeable decrease in line intensity at the larger radii.

Radial and Axial Intensity Profiles

If the plasma is optically thin, the intensity $I(\lambda)$ within a small wavelength interval $d\lambda$ of a spectral line is proportional to the number of particles within the volume sampled by the line of sight which radiate in this wavelength interval.[40] Thus the total line intensity $I_T = \int_0^\infty I(\lambda)\,d\lambda$, which is simply the area under the line profile, is proportional to the total number of particles undergoing the spectral transition giving rise to the spectral line in question. The areas under the Doppler-split line profiles of Figs. 4-6 and 4-7 should consequently be proportional to the sum of the total number of particles in the sampled volume radiating at the nominal wavelength of 4880 $\overset{o}{A}$ in each of the two argon jets intersected by the line of sight, if the jets are optically thin to this radiation.

Experiments were done at the lines of sight 4.6 and 10.9 cm from the anode plane to determine whether the Doppler-split 4880 $\overset{o}{A}$ line is indeed optically thin. The technique consisted of placing a concave mirror at twice its focal length from the discharge axis in the extension of the optical path and measuring the increase in intensity. Figure 4-10 shows a schematic of this arrangement. If no losses occur at the mirrors or the tank windows the observed intensity with the concave mirror in place should be double that without the mirror. In actual fact there are absorption and reflection losses at the mirrors and windows, and these must be corrected for. These losses were measured experimentally with the argon laser and a silicon photodiode and found to amount to 36%. The MPD arc was fired several times, alternately with and without the concave mirror in place. The observed sets of line intensities were averaged
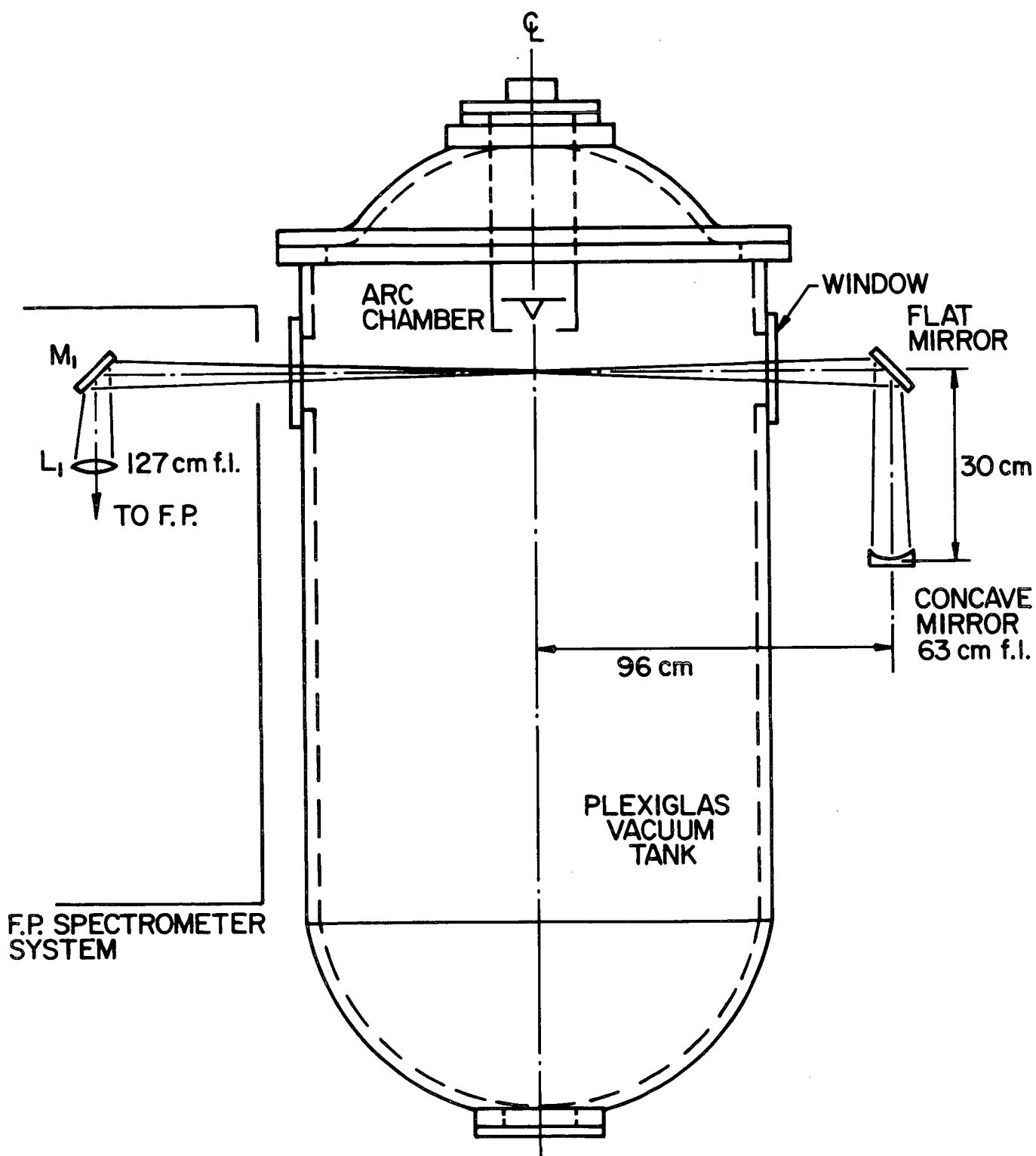
SET-UP FOR OPTICAL THICKNESS TEST

FIGURE 4-10

AP25·4848

and compared. The experimental results agreed with the predicted increase in intensity within a few percent, well within the experimental error, thus confirming that the 4880 $\overset{\text{o}}{\text{A}}$ line is optically thin.

To obtain radial relative intensity profiles the area under each spectral line profile obtained in the radial surveys was measured (with corrections for background continuum) and the results at each distinct line of sight were averaged and normalized to the maximum value observed. Figure 4-11 shows the variation of the relative 4880 $\overset{\text{o}}{\text{A}}$ line intensity with vertical distance above and below the discharge axis at the four axial planes investigated. The off-center maxima correspond to the upper and lower pairs of argon jets visible in Figs. 3-9a and 3-9b. The central peak corresponds to the middle pair of argon jets. A plot of the loci of the off-center maxima, suitably corrected for the $30°$ azimuthal inclinations of the upper and lower argon jets with respect to the vertical axial plane, is shown in Fig. 4-12. In effect, these loci, which turn out to be straight lines inclined at $15°$ to the discharge axis with a virtual origin at the cathode tip, are reasonable approximations to the average flow direction in each argon jet. The axial variation of the relative 4880 $\overset{\text{o}}{\text{A}}$ line intensity in an individual jet is displayed in Fig. 4-13. The dependence of intensity on distance from the anode plane appears to follow an inverse square law. Because the jets appear to expand laterally in a linear fashion the integrated path length through the jets increases linearly with increasing axial distance. Thus, if the radiating particle density were to vary as the inverse square of the distance from the chamber orifice, such as in source flow-like free expansions, one would expect an integrated intensity which decreases only inversely with distance. That the intensity decreases faster is an indication that the radiating particle density falls off more steeply than the inverse square of distance. Since the radiating particle density is a strong function of electron temperature,[25-26] the above results signify that the electron temperature decreases with increasing distance from the chamber exit. Further discussion of the electron temperature is given in section 4-4.

FIGURE 4-11
AP 25·4807
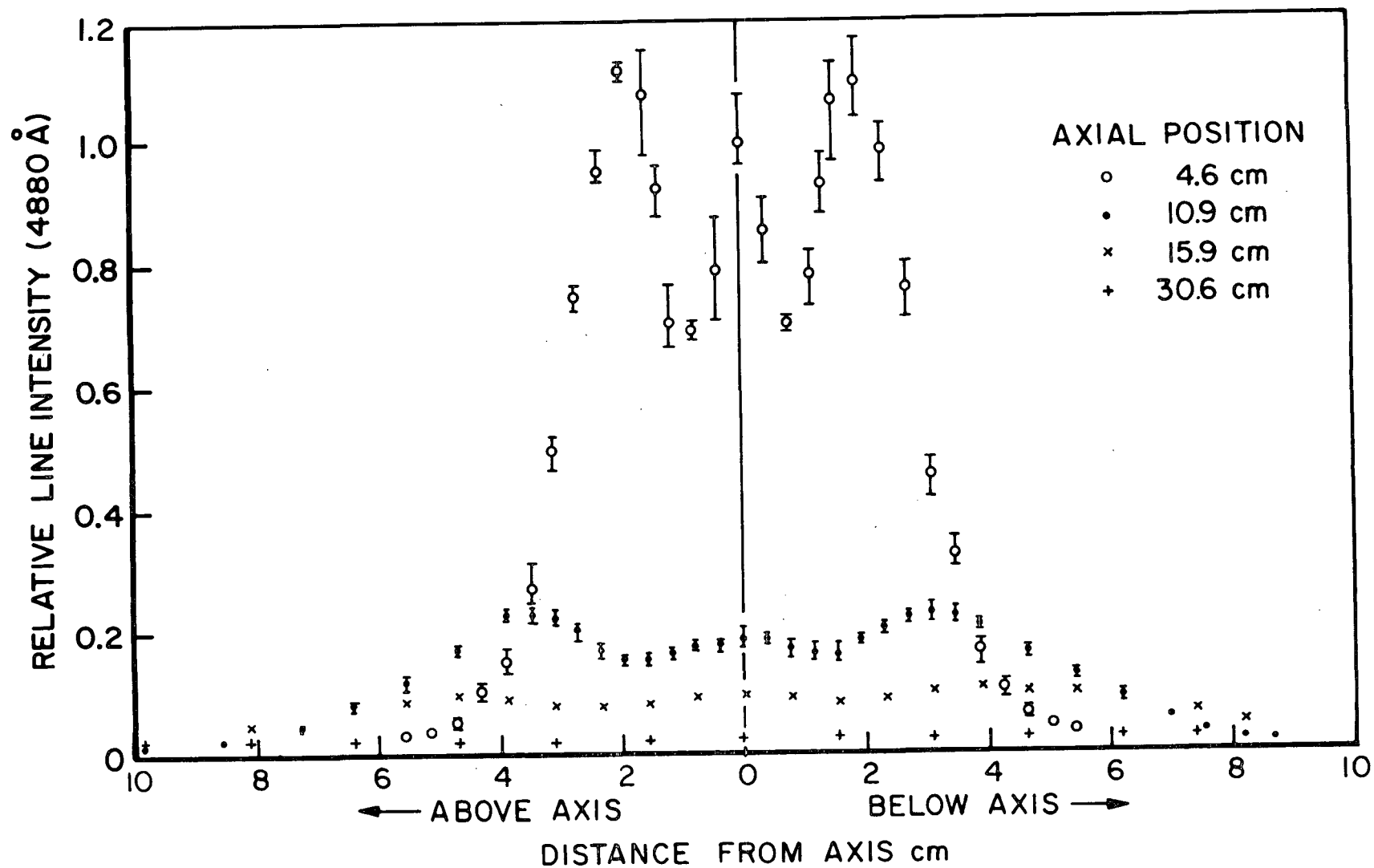
RADIAL INTENSITY PROFILES

FIGURE 4-12
AP25·4808

ARC CHAMBER

AXIAL DISTANCE X, cm

DISTANCE OFF AXIS Y, cm

77
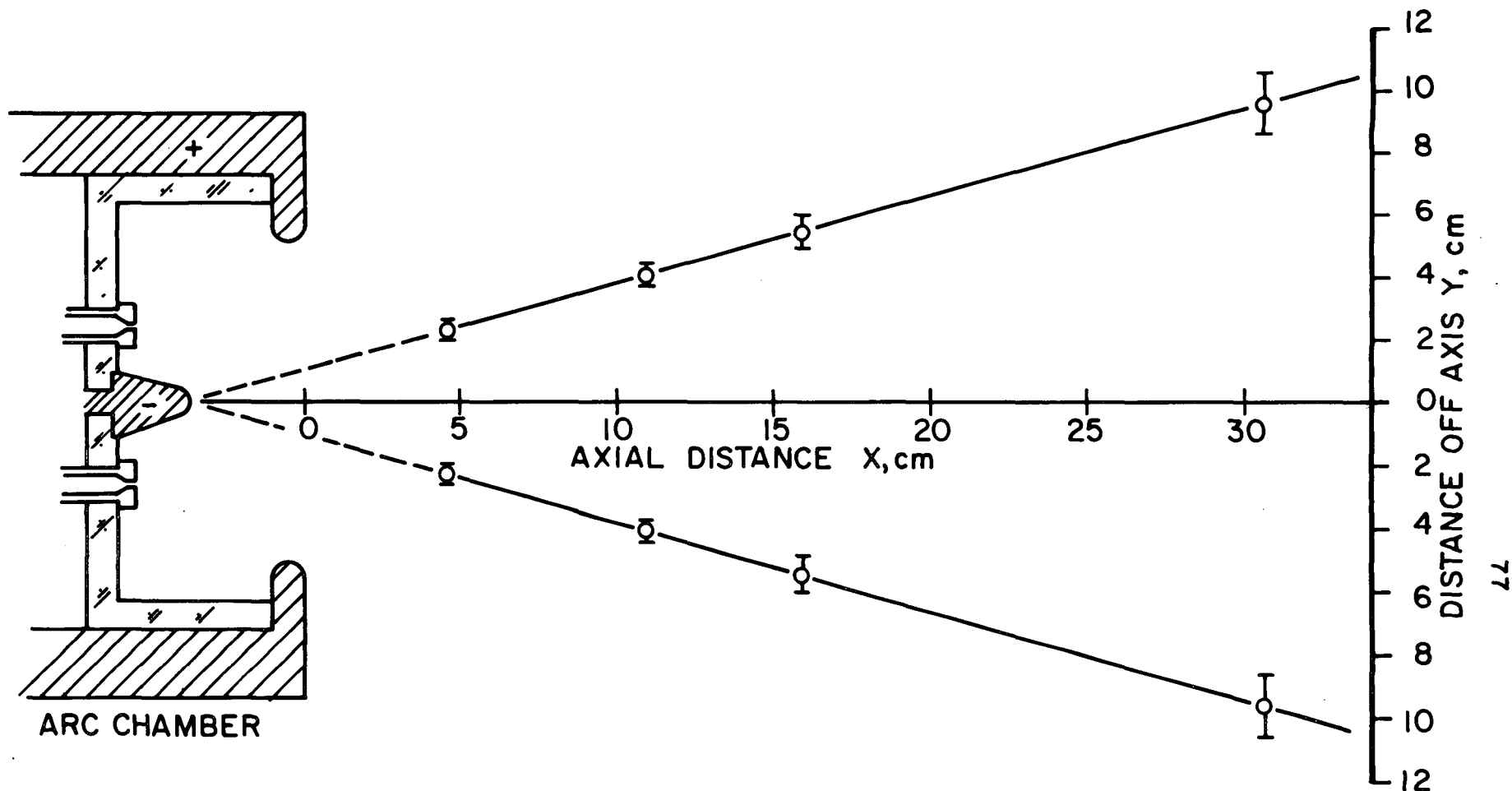
LOCI OF MAXIMUM 4880 Å LINE INTENSITY IN AⅡ JET
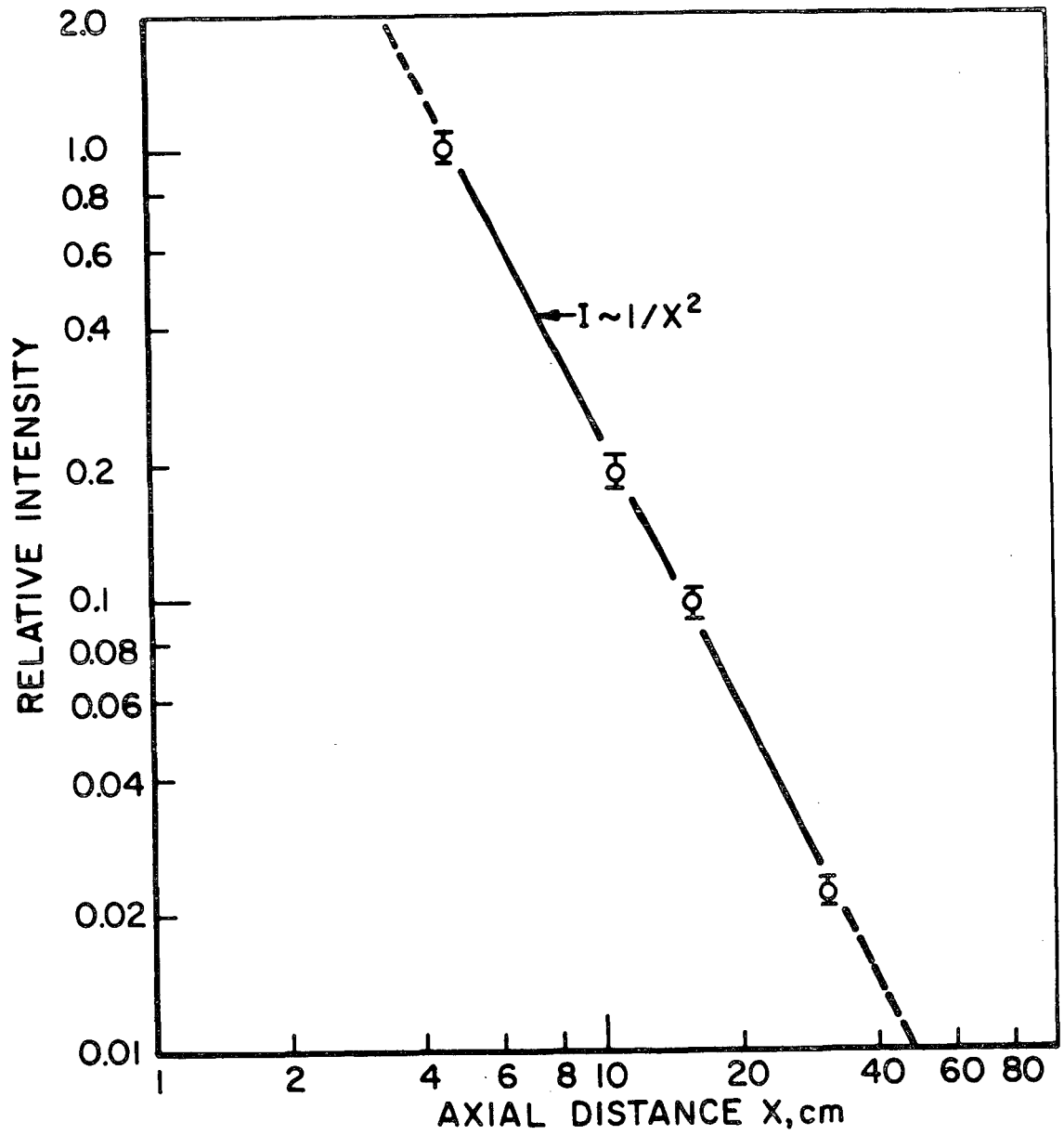
DEVELOPMENT OF 4880Å LINE INTENSITY IN AⅡ JET

FIGURE 4-13
AP25·4809

Survey at 75° Lines of Sight

A series of Doppler-shift velocity measurements was done at five axial positions with the line of sight at an angle of 75° to the discharge axis, passing through the two diametrically opposed argon jets in the horizontal plane, as shown in Fig. 4-14. Assuming as a first approximation, from the results of the previous section, that the average jet flow angle is 15° with respect to the axis, these lines of sight are perpendicular to the far jet and intersect the near jet at an angle of 60°. The observed line profile should therefore have a shifted and an unshifted component. This is almost the case, as can be seen in Fig. 4-15, obtained at a line of sight which crosses the axis 16.8 cm from the chamber exit plane (Line of sight "c" in Fig. 4-14). The upper trace in each oscillogram corresponds to the discharge current history, while the lower traces exhibit line profiles scanned by the Fabry-Perot interferometer. In each case two successive scans of the line were recorded; the comments here apply to the first scans on the left. Figure 4-15a shows the relative Doppler shift between the near and far jets. The "unshifted" component on the left corresponds to the far jet, intersected at ∼ 90°, while the blue-shifted component to its right corresponds to the near jet intersected at ∼ 60°. Figure 4-15b displays the absolute Doppler shift between the line component from the near jet and the simultaneously recorded 4879.9 Å reference laser line. (The laser intensity was made as large as possible relative to the discharge intensity to minimize distortion of the laser line by the "unshifted" component of the 4880 Å line from the far jet. This is the reason for the different intensity scale in Fig. 4-15b). The shift between the near jet line component and the laser reference is somewhat less than that between the line components of the near and far jets, indicating that the true mass-averaged velocity vector of the argon in the jets makes an angle somewhat greater than 15° with the discharge axis.
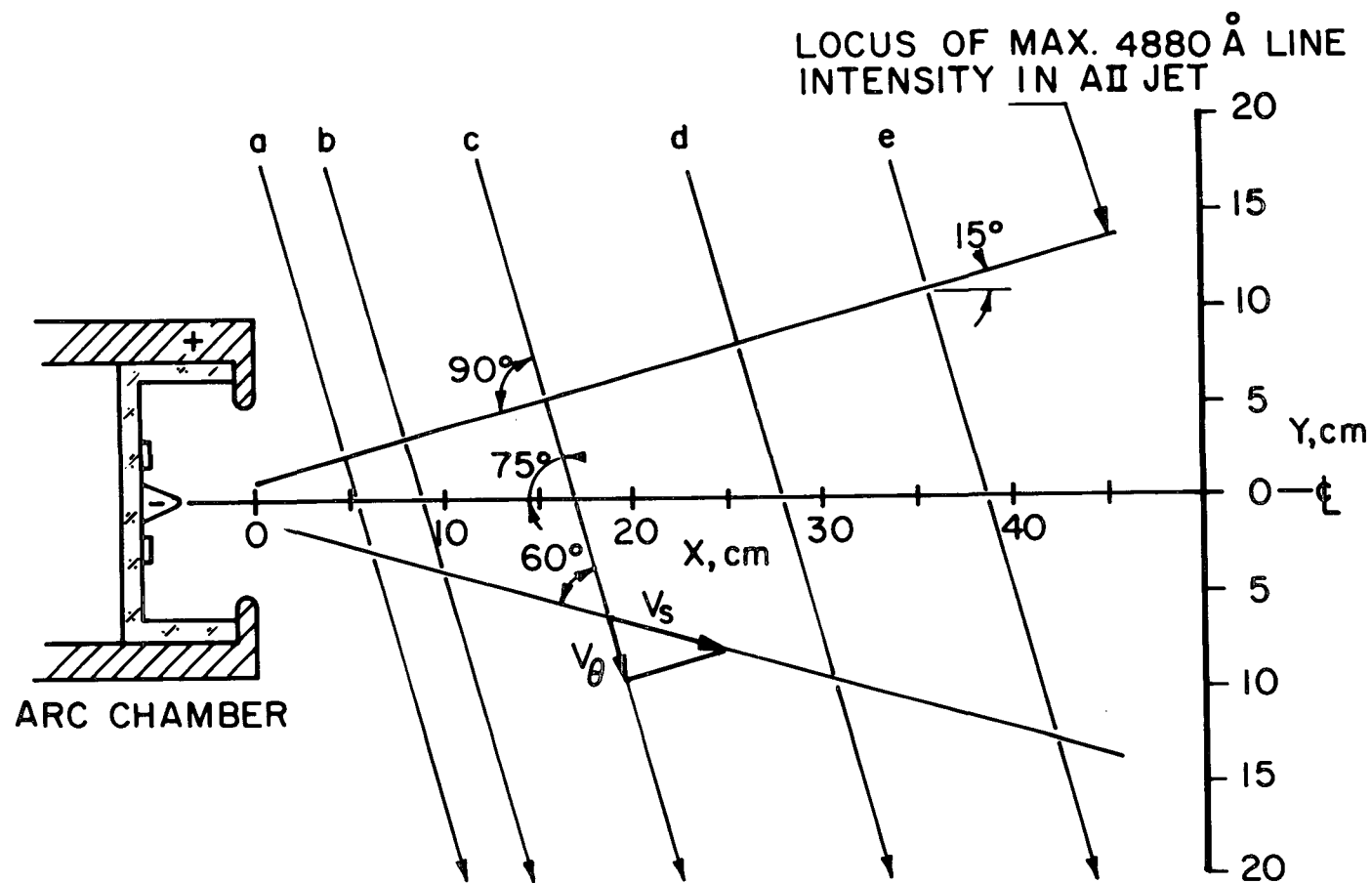
LINES OF SIGHT USED IN VELOCITY MEASUREMENTS

FIGURE 4-14
AP 25·4810

80
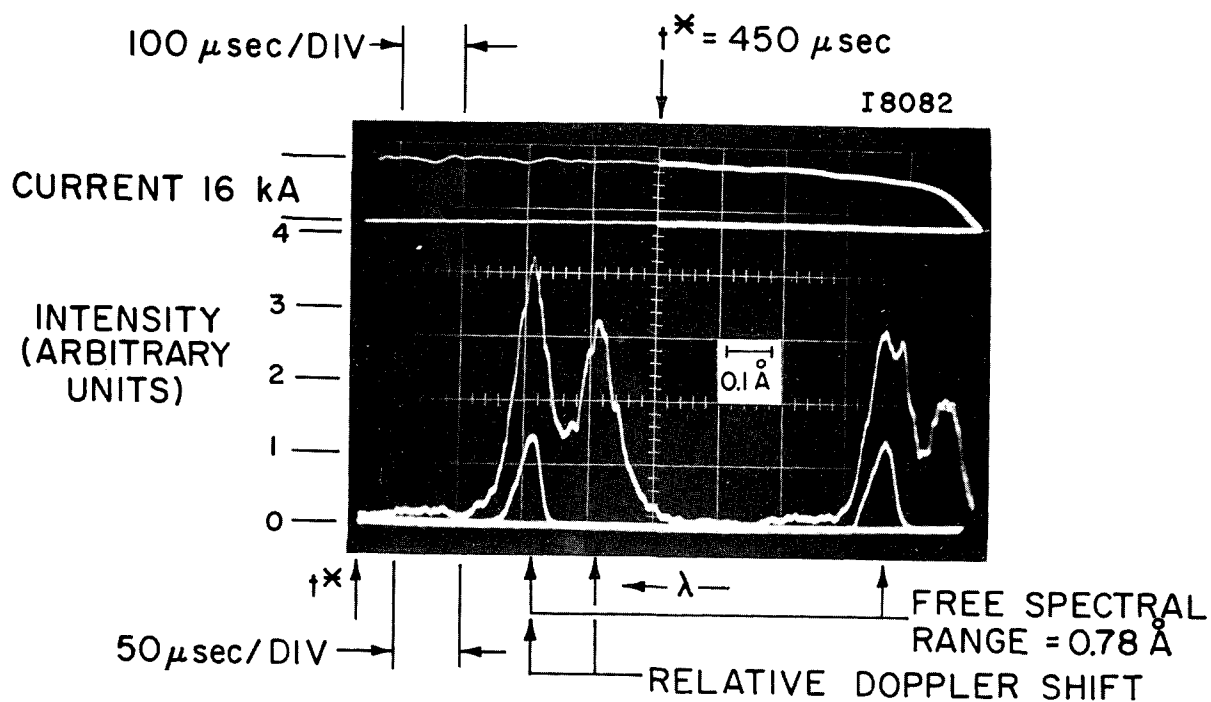
a) LIGHT FROM ARGON JETS ONLY
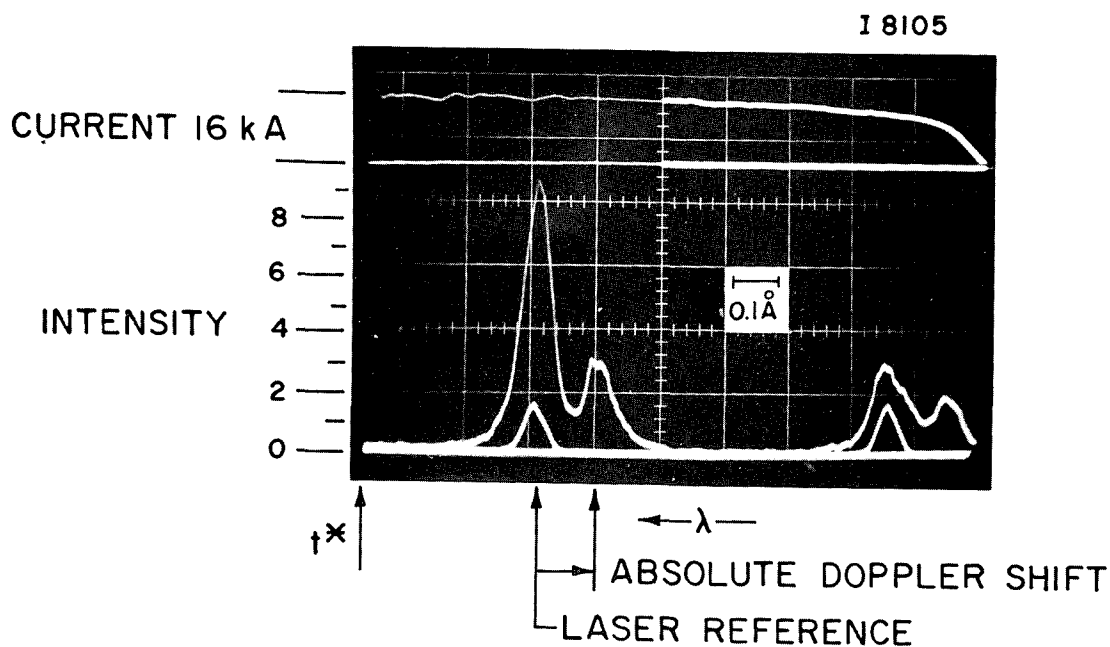
b) LASER REFERENCE SUPERIMPOSED

PROFILES AND DOPPLER SHIFTS OF 4880 Å
AII LINE ON LINE OF SIGHT CROSSING AXIS
AT X = 16.8 cm

FIGURE 4-15

AP25·P438

In Fig. 4-16 are shown typical absolute Doppler shifts between the near jet line component and the laser reference line, obtained at the four other 75° lines of sight. The vertical intensity scale in each case is different but this does not affect the wavelength calibration. At least ten such profiles were recorded at each line of sight and the respective Doppler shifts averaged. The line profiles in Fig. 4-16 appear broader than the ones obtained at the 90° lines of sight (Fig. 4-7) because of the failure of one of the fine-adjust piezoelectric transducers on the stationary interferometer plate mounting. This caused considerable difficulty in the adjustment of plate parallelism in the interferometer, and the overall instrumental finesse decreased from 25 to about 12 as a result. Fortunately, the loss of resolution is not serious.

Calculation of Jet Velocity and Flow Angle

Once the velocity components at 75° and at 90° to the discharge axis are known at various positions along the argon jets, it is relatively straightforward to deduce both the magnitude and the direction of the average velocity vectors in the argon jets as functions of axial distance from the chamber exit plane. An initial estimate of jet flow angle and locus is required in order to obtain the approximate positions along the near jet at which the 75° lines of sight intersect. It has already been shown that the peak luminous intensity in each jet follows a straight line inclined at 15° to the axis with a virtual origin at the tip of the cathode (Fig. 4-12). This locus will be used initially to define the position of the argon jets. It will turn out that this approximation is good enough that no further refinements will be required for the calculations outlined below.

The calculation procedure is as follows: choose, for example, the 75° line of sight labeled "c" in Fig. 4-14, which intersects the discharge axis 16.8 cm from the chamber exit plane. From the figure it can be seen that it also intersects

a) X = 5.3 cm

b) X = 8.8 cm

LASER REFERENCE

SHIFTED LINE

I·8194

I·8183

50μsec/DIV

O .1 .2 .3 .4 Å
WAVELENGTH SCALE

I·8130

I·8161

c) X = 27.8 cm

d) X = 38.6 cm
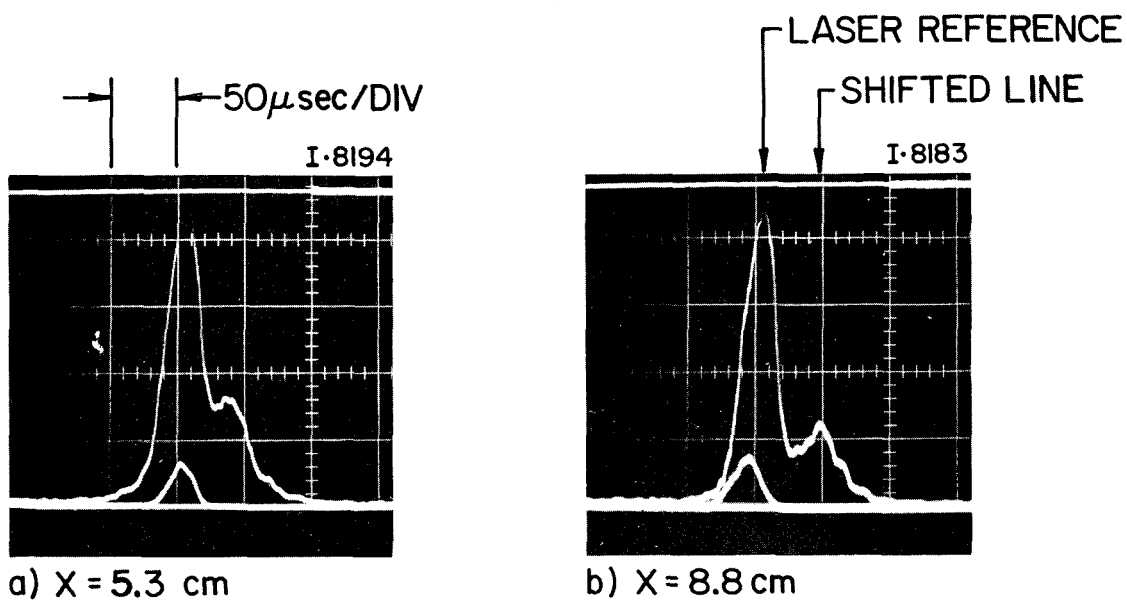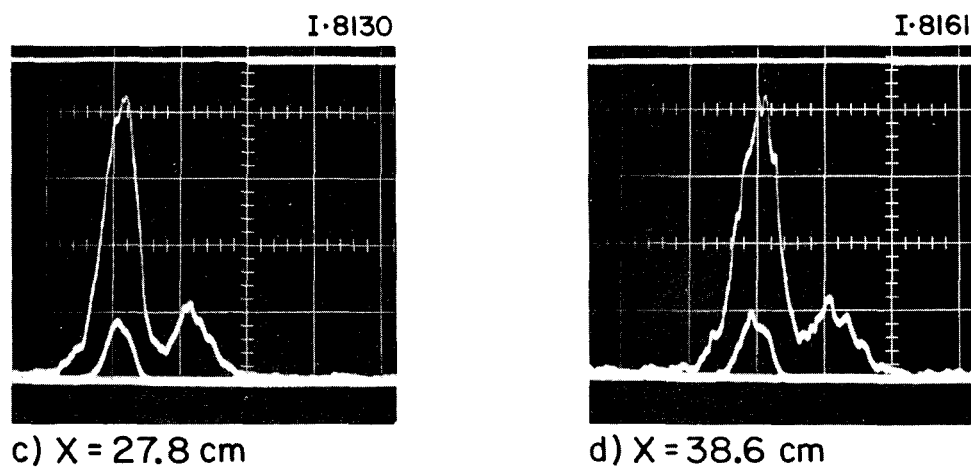
(INTENSITY SCALES ARBITRARY)

ABSOLUTE DOPPLER SHIFTS OF 4880 Å
A II LINE ON 75° LINES OF SIGHT

FIGURE 4-16
AP25· P·475

the near-jet locus at a point 18.5 cm from the chamber exit
and 6.2 cm from the axis. Figure 4-8 reveals that the average
radial component of velocity V_R is 5.0×10^3 m/sec at this
point. The measured Doppler shift along the chosen 75° line
of sight yields an average velocity $V_\theta = 8.4 \times 10^3$ m/sec. The
average velocity V_S along the jet and the average flow angle
$\propto$ can be obtained from the following simple relations:

$$V_\theta = V_S \cos \left(75^\circ - \propto \right)$$

$$V_R \approx V_S \cos \left(90^\circ - \propto \right)$$

Solving for $\propto$:

$$\propto = \cot^{-1} \left[3.86 \left(\frac{V_\theta}{V_R} - 0.965 \right) \right]$$

Thus

$$V_S = \frac{V_R}{\sin \propto} = \frac{V_\theta}{\cos \left(75^\circ - \propto \right)}$$

A simple graphical construction, as shown in Fig. 4-17, can
also be used. For the example chosen the results are
$V_S = 1.47 \times 10^4$ m/sec, $\propto = 20^\circ$. Because of the relatively flat
radial velocity profile (Fig. 4-8) the discrepancy between the
assumed and calculated flow angles does not warrant recalcula-
tion of the velocity V_S with a better approximation of $\propto$. The
errors in V_S arising from the original assumption of $\propto$ are
well within the experimental uncertainties.

The results of the velocity and flow angle calculations
are displayed in Figs. 4-18 and 4-19. Figure 4-18 shows a
plot of jet velocity V_S versus axial distance, x , from the
chamber exit. The circular data points were obtained from
$V_S = V_\theta / \cos (75^\circ - \propto)$ while the triangular data points were calcu-
lated from $V_S = V_R / \sin \propto$, where V_R was obtained from the data
at the four lines of sight used in the perpendicular surveys.
(Fig. 4-8) The vertical error bars represent the degree of
uncertainty arising from the spread of the experimental data,
while the horizontal error bars encompass the probable error

Y = 6.2 cm

$\vec{V}_X$ 13.8 × 10³ m/sec

x = 18.5 cm →

α = 20°

90°

75°

$\vec{V}_S$ 14.7 × 10³ m/sec

$\vec{V}_R$

5.0 × 10³
m/sec

$\vec{V}_\theta$
8.4 × 10³ m/sec

$\vec{V}_R$, $\vec{V}_\theta$ MEASURED EXPERIMENTALLY

$\vec{V}_S$, $\vec{V}_X$ DETERMINED GRAPHICALLY

FIGURE 4-17
AP25·4811

85
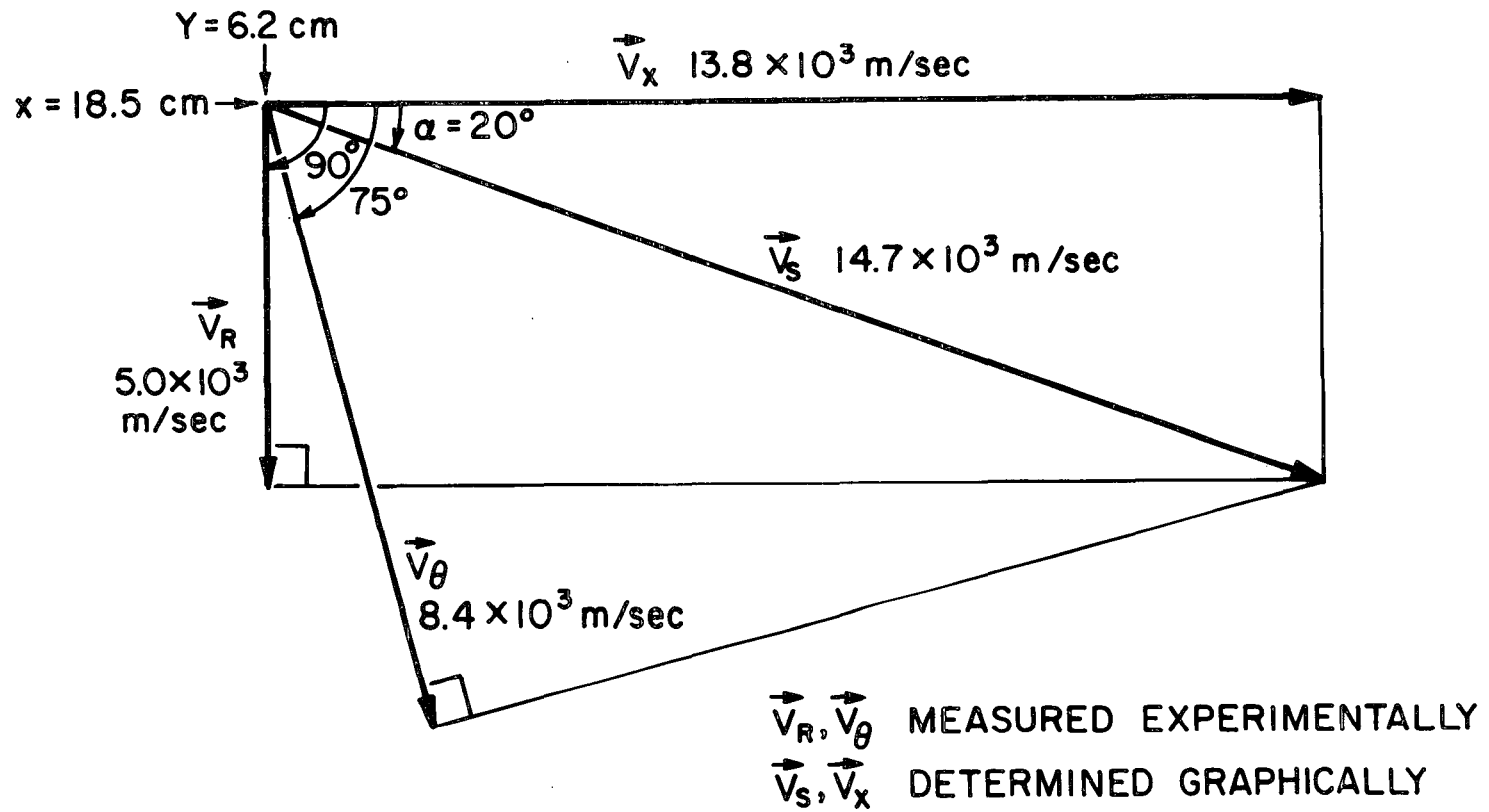
GRAPHICAL DETERMINATION OF A II JET VELOCITY

DEVELOPMENT OF ARGON ION JET VELOCITY

FIGURE 4-18
AP25·4812

FIGURE 4-19
AP25·4849
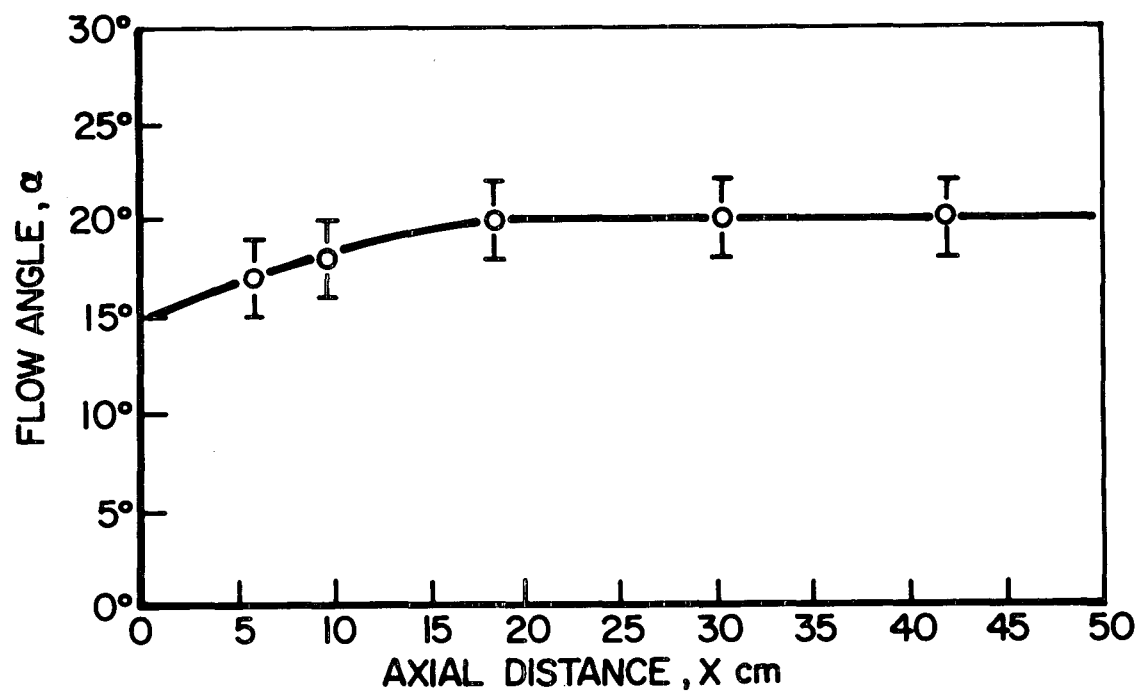
DEVELOPMENT OF AVERAGE FLOW ANGLE OF ARGON JETS

in axial position resulting from the original assumption of 15° flow angle. The average velocity along each jet is seen to increase from ~8300 m/sec 4.6 cm from the chamber exit to a plateau of ~16,500 m/sec 40 cm downstream. The bulk of the acceleration occurs over a distance of the order of an anode orifice diameter. It is interesting to note that the observed final velocity is nearly twice the so-called Alfvén critical velocity for argon (8700 m/sec),[2,30] which has been recently claimed by Malliaris et al.[30] The present result indicates that specific impulses as high as about 1600 sec may be attainable using argon as a propellant, contrary to the limiting 850 sec suggested by Malliaris[30] A discussion of possible acceleration mechanisms which may be responsible for the high argon velocities observed here is presented in Chapter 5.

Figure 4-19 shows the variation of average jet flow angle, α, with distance from the chamber exit. α increases from about 17° at x = 6 cm to about 20° at x = 18 cm and remains constant at about 20° thereafter. This is a somewhat different result from that anticipated from the locus of maximum jet intensity and is a result of line of sight integration effects. In actual fact, the 15° locus is an accurate representation of the local flow angle rather than the average flow angle which is weighted to larger values by the higher flow angles present at the larger radii.

4-4 TEMPERATURE MEASUREMENTS

In order to determine whether the high flow velocities observed in the argon jets are a result of electrothermal conversion via the downstream expansion permitted by the MPD accelerator geometry,[13] it is necessary to measure the axial profiles of ion and electron temperature in the argon jets. Kinetic atom and ion temperatures in plasmas of 1-100 eV are generally determinable from measurements of half-widths of Doppler-broadened spectral lines, the technique that is used here. Electron temperatures can be measured spectroscopically by the ratio of line intensities, but only in plasmas which are either in full or local thermodynamic equilibrium.[25,40] Such conditions do not in general exist in the plasma flows produced by MPD arcs[2] and electron temperatures thus are

usually measured by means of electrostatic probes.[2,8,28] This section discusses in detail the measurement of argon ion temperatures with the scanning Fabry-Perot spectrometer, and presents electron temperature data obtained by other investigators on the same accelerator.[8,28]

Doppler Width Measurements of Ion Temperature

The motion of a radiating particle toward or away from an observer leads to a Doppler shift in the wavelength of the emitted line. In a plasma the random thermal motions of the radiating particles cause a Doppler broadening of the lines as the overall result. If the velocity component of a particle parallel to the direction of observation is v_p, then the wavelength shift is

$$\Delta\lambda = \pm \frac{v_p}{c} \lambda_o$$

where λ_o is the unshifted wavelength and c is the speed of light. If the motion of the plasma particles is purely thermal the velocity distribution of the emitters is Maxwellian. Thus, the fraction of particles moving in the line of sight with velocity components between v_p and $v_p + dv_p$ is given by[47]

$$\frac{dn}{n} = \left(\frac{m}{2\pi k T}\right)^{1/2} exp\left(-\frac{m v_p^2}{2 k T}\right) dv_p$$

where T is the temperature of the particles, m is the atomic mass and k is Boltzmann's constant. By substituting $\Delta\lambda$ for v_p according to the Doppler shift relation one obtains

$$\frac{dn}{n} = \left(\frac{m c^2}{2\pi k T \lambda_o^2}\right)^{1/2} exp\left[-\frac{mc^2}{2 k T}\left(\frac{\Delta\lambda}{\lambda_o}\right)^2\right] d(\Delta\lambda)$$

If the lines are optically thin, the intensities I are proportional to the concentration of radiating particles n; and, in

particular, the intensity emmitted in the interval d($\Delta\lambda$),
namely I($\Delta\lambda$)d($\Delta\lambda$) is proportional to the fraction of par-
ticles dn. Thus, for a purely Doppler-broadened line one
obtains a Gaussian shape for the intensity distribution:[40]

$$I(\Delta\lambda) = I_T \left(\frac{mc^2}{2\pi kT\lambda_o^2}\right)^{1/2} exp\left[-\frac{mc^2}{2kT}\left(\frac{\Delta\lambda}{\lambda_o}\right)^2\right]$$

where I_T is the total line intensity and $\Delta\lambda$ is the devia-
tion from line center λ_o. The intensity reaches one-half
its maximum value when the exponent has the value 1/2. The
full half-width, which is the width between the two half-
maximum intensity points follows as:

$$\Delta\lambda_D = \left(\frac{2kT\ln 2}{mc^2}\right)^{1/2}\lambda_o$$

$$= 7.16 \times 10^{-7}\lambda_o\left(\frac{T}{M}\right)^{1/2}$$

where $\Delta\lambda_D$ is obtained in $\overset{o}{A}$ if λ_o is in $\overset{o}{A}$ and T is in ^oK,
and M is the atomic weight. It is evident that thermal Doppler
broadening is most pronounced for lines of light elements at
high temperatures. In the case of the 4880 $\overset{o}{A}$ line of ionized
argon temperatures in the range of 10^4 to 10^5 ^oK result in half-
widths of 0.06 to 0.19 $\overset{o}{A}$.

Doppler broadening is not the only important line broaden-
ing mechanism found in plasmas. A variety of other mechanisms
such as Stark broadening, Zeeman splitting, and non-thermal
motions such as gross mass motion and microturbulence will
broaden spectral lines to a degree which depends on the pre-
vailing conditions.[25,40,48,49] Other effects which act to
distort line profiles are self-absorption, if the spectral line

is not optically thin,[40] and instrumental broadening due
to the finite resolution of the recording spectrometer.[40]
It is therefore essential to ascertain experimentally or
theoretically that either these broadening effects are in-
significant or that they can be accurately accounted for
in the data reduction. The importance of each of the above
mentioned broadening mechanisms will now be examined.

Stark Broadening:

Stark broadening of lines emitted by atoms or ions in
a plasma is a result of the interaction of the radiating par-
ticles with electric fields originating in the surrounding
ions and electrons, and is a direct function of the electron
density.[25,40] The quantum mechanical calculations which
are used to determine the relation between the broadening and
the electron density for a variety of atomic species are dis-
cussed in detail in Refs. 25 and 40. Recent experimental
measurements of the Stark broadening of several lines of
ionized argon[50] show that for the 4880 Å line the Stark
half-width amounts to ~ 0.05 Å at an electron density of
10^{16} cm^{-3}. Measurements of the electron density in the ex-
haust of the MPD arc reveal densities of the order of 10^{15} cm^{-3}
and less in the regions of the plume downstream of about 5 cm
from the chamber exit.[15] Since the Stark width is directly
proportional to the electron density for heavy atoms and
ions[25,40,50] it is expected that the Stark width of the
4880 Å line of AII will be less than 0.005 Å in those regions
of the argon jets of interest here. This width is more than
an order of magnitude less than the estimated thermal Doppler
widths and may thus be neglected with little resulting error.

Zeeman Splitting:

The presence of strong magnetic fields will cause a
Zeeman splitting of spectral lines and thus alter the line
profiles. The order of magnitude of the splitting of a line
of argon of wavelength λ (Å) is given by[48]

$$\Delta \lambda_z \approx 10^{-9} \lambda^2 B$$

where B is the magnetic field strength in Weber/m^2. The highest field strengths found in the MPD accelerator occur in the vicinity of the cathode and have a magnitude of about 0.3 Weber/m^2 (see Chapter 5, Fig. 5-1) leading to a Zeeman split of the 4880 $\overset{\text{o}}{\text{A}}$ line of ~ 0.007 $\overset{\text{o}}{\text{A}}$ in those locations. However, 2 cm downstream of the chamber exit B is down to 0.01 Weber/m^2 and the Zeeman splitting is thus only about 2×10^{-4} $\overset{\text{o}}{\text{A}}$, a negligible amount. Further downstream it is even less.

Microturbulence:

There is abundant evidence that strong ion turbulence is often present in magnetically confined plasmas.[25,48,49] Although the exhaust flow of the MPD arc is not in the strict sense magnetically confined (except in the vicinity of the cathode tip) there is evidence of turbulence. For example Langmuir probes and double electrostatic probes display random fluctuations of ion saturation currents which are usually ascribed to turbulent fluctuations convected past the probes. These may, of course, be manifestations of wave propagation effects but this is not yet clear. Turbulence can be so fine grained that the velocity distribution is closely Maxwellian on a macroscopic scale while quite large deviations could occur on a microscopic scale. If the turbulent motion is Maxwellian on the macroscopic scale its contribution to line width is determined by[25]

$$\Delta \lambda_t = \lambda_o \left[\left\langle \left(\frac{v_r}{c} \right)^2 \right\rangle_{AV.} \ell n \, 2 \right]^{\frac{1}{2}}$$

where v_r describes the relative macroscopic velocity component along the line of sight of the various volume elements of the emitting plasma and λ_o and c have their usual definitions. Unfortunately there are no data available on average random turbulent velocities in the exhaust of the MPD arc, and

until quantitative measurements can be made it will be
assumed that microturbulent line broading is not signifi-
cant.*

Gross Mass Motion:

Gross mass motion will contribute to line broadening
if there is a distribution in the velocities of macroscopic
volume elements of the plasma along the line of sight.
Clearly, this effect occurs within the argon jets in the
MPD exhaust, inasmuch as there is a spread in the radial
velocity components across the jets. The shape of the line
broadening function arising from this effect depends on the
radial profile of velocity and local line intensity across
each jet. These are difficult to evaluate accurately be-
cause the azimuthal non-uniformity of the exhaust does not
permit reduction of the spectroscopic measurements to purely
local values. For present purposes it will be assumed that
to a first approximation the flow velocity is constant across
a jet and equal to the average measured velocity, V_s. Further-
more, it will be assumed that the 4880 $\overset{o}{A}$ local intensity pro-
file across each jet has a Gaussian shape. This assumption
is reasonable because the integrated intensity distributions
across the upper and lower jets (Fig. 4-11) appear approximately
Gaussian. This being the case, the broadening function due to
the distribution of radial velocities in each argon jet will
also be Gaussian. It remains to determine the radial angular
spread of the jets at their half-intensity points. From the
photographs of Figs. 3-9 and 3-10 and the intensity profiles
of Fig. 4-11 the jets are estimated to have a 10° radial
divergence angle about the 15° jet locus. With this informa-
tion and the measured average jet velocities, V_s, the com-
ponents of radial velocity at the inner and outer half-intensity
points of the jets can be estimated. The difference between

---

*One method of determining the importance of microturbulence
is to measure the widths of lines from radiating species of dif-
ferent charge to mass ratio.[48] If turbulence is significant a
different temperature will be obtained with each specie. Un-
fortunately, due to the species separations present in the MPD
exhaust and the opaqueness of the Fabry-Perot plates to ultra-
violet radiation from AIII, it has not been possible to carry out
such an experiment.

these two values at a given axial position gives rise to a
Doppler shift which provides a reasonable estimate of the
line broadening due to the gross mass motion. For example
at x = 30 cm such a calculation yields a broadening of
~ 0.04 Å which is of the same order of magnitude as the ex-
pected thermal Doppler widths.

Line Reversal:

Distortions to the line profile due to finite optical
depth of the plasma will also result in a broadening of the
spectral line. In the present case however, this effect is
non-existent, since the plasma has been verified to be optically
thin at 4880 Å. (Section 4-3)

Instrumental Broadening:

The Fabry-Perot interferometer, like all other spectrometric
instruments, has a finite resolving power and consequently
leads to a further broadening of the spectral lines. [42,43,45]
The broadening mechanisms in the Fabry-Perot spectrometer are
well known (Appendix B) and in general result in an instru-
mental function which very closely approximates a Gaussian
shape. This is fortuitous as it simplifies the unfolding of
the instrumental function from the Gaussian Doppler profile.
The folding of two Gaussian shapes results in a Gaussian pro-
file with half-width equal to the square root of the sum of
the squares of the individual half-widths. [51,52] The half-width
of the Fabry-Perot can be easily calculated from its total
finesse F_T and its free spectral range $\Delta\lambda_f$. As used in the
experiments described here, the interferometer has a finesse
of 25 and a free spectral range of 0.78 Å. Therefore the in-
strumental half-width is given by $\Delta\lambda_i = \Delta\lambda_f/F_T = 0.031$ Å.

Experimental Results

The 4880 Å spectral line profiles of AII obtained in the
90° line of sight survey were used to calculate the argon ion
temperature from line widths. Only the data obtained at the
lines of sight level with the axis, intersecting the two argon

jets in the horizontal plane, were used in order to obtain maximum separation of the two Doppler shifted line components. The estimates of other line broadening effects discussed in the previous sub-section have shown that Stark, Zeeman and line reversal effects can be neglected compared to expected Doppler widths. Microturbulence broadening could not be evaluated because of lack of pertinent data. However, the broadening caused by the spread of radial velocities across each jet and the instrumental broadening were shown to be significant and thus were taken into account in the reduction of line widths.

The observed profile of each line component is a convolution of the Doppler profile of half-width $\Delta\lambda_D$, the velocity spread function of half-width $\Delta\lambda_v$, and the instrumental function of half-width $\Delta\lambda_i$. Since the latter two are here assumed to be Gaussian and the Doppler profile is Gaussian, the total measured half-width is simply:[51,52]

$$\Delta\lambda_T = \left(\Delta\lambda_D^2 + \Delta\lambda_v^2 + \Delta\lambda_i^2\right)^{1/2}$$

Thus the true Doppler width is:

$$\Delta\lambda_D = \left(\Delta\lambda_T^2 - \Delta\lambda_v^2 - \Delta\lambda_i^2\right)^{1/2}$$

and the argon ion temperature is given by

$$T = 7.8 \times 10^{13}\left(\frac{\Delta\lambda_D}{\lambda_o}\right)^2 \quad {}^\circ K$$

which for $\lambda_o = 4880 \ \overset{\circ}{A}$ becomes

$$T = 3.28 \times 10^6 \ \Delta\lambda_D^2 \quad {}^\circ K$$

$$= 2.83 \times 10^2 \ \Delta\lambda_D^2 \quad eV$$

where $\Delta\lambda_D$ is in $\overset{\circ}{A}$. It must of course be emphasized that due to the line of sight integration effects the temperature so calculated is only an average across the width of the jet.

The results are shown in Fig. 4-20 with the ion temperature T_i in the argon jets plotted against axial distance from the chamber exit plane. The circled points are the averages obtained from all the line widths measured at each line of sight and the error bars encompass the spread in measured total widths and the uncertainty in the radial velocity distribution at each line of sight. It should be mentioned here that even under ideal conditions it is difficult to obtain an accuracy in the measured temperatures that is substantially better than 20% because the line widths themselves are difficult to read to an accuracy better than 10%. In the present case, the lack of knowledge of the true radial velocity distribution function and the neglect of microturbulence effects increases the uncertainty. In general, however, since most processes tend to increase the line width rather than decrease it, the results shown in Fig. 4-20 may be considered at worst to be upper limits of the ion temperature.

The best line drawn through the circled points indicates that the ion temperature follows an inverse power law, $T_i \sim x^{-3/4}$, decreasing from ~ 1.8 eV at $x = 4.6$ cm to ~ 0.5 eV at $x = 30.6$ cm. Extropolation back towards the chamber predicts values of 5-6 eV in the vicinity of the chamber exit. The observed ion temperatures are significantly lower than had been estimated previously on the basis of spectrographic[18] and Langmuir probe data.[8] The overestimate in the previous spectrographic experiments[18] is now known to have been a result of neglecting the Doppler split in the spectral lines due to the discrete argon jet structure in the exhaust plume. (It is interesting to note that if it is assumed that the exhaust flow behaves as a free isentropic expansion so that $\rho \sim x^{-2}$ and $T \sim \rho^{\gamma-1}$, where ρ is the mass density and γ is the ratio of specific heats, the fact that $T_i \sim x^{-3/4}$ predicts $\gamma \approx 1.38$ which agrees with values deduced by other means in similar environments.[13]) The decrease in ion temperature down the plume simultaneously with the increase in flow velocity suggests that
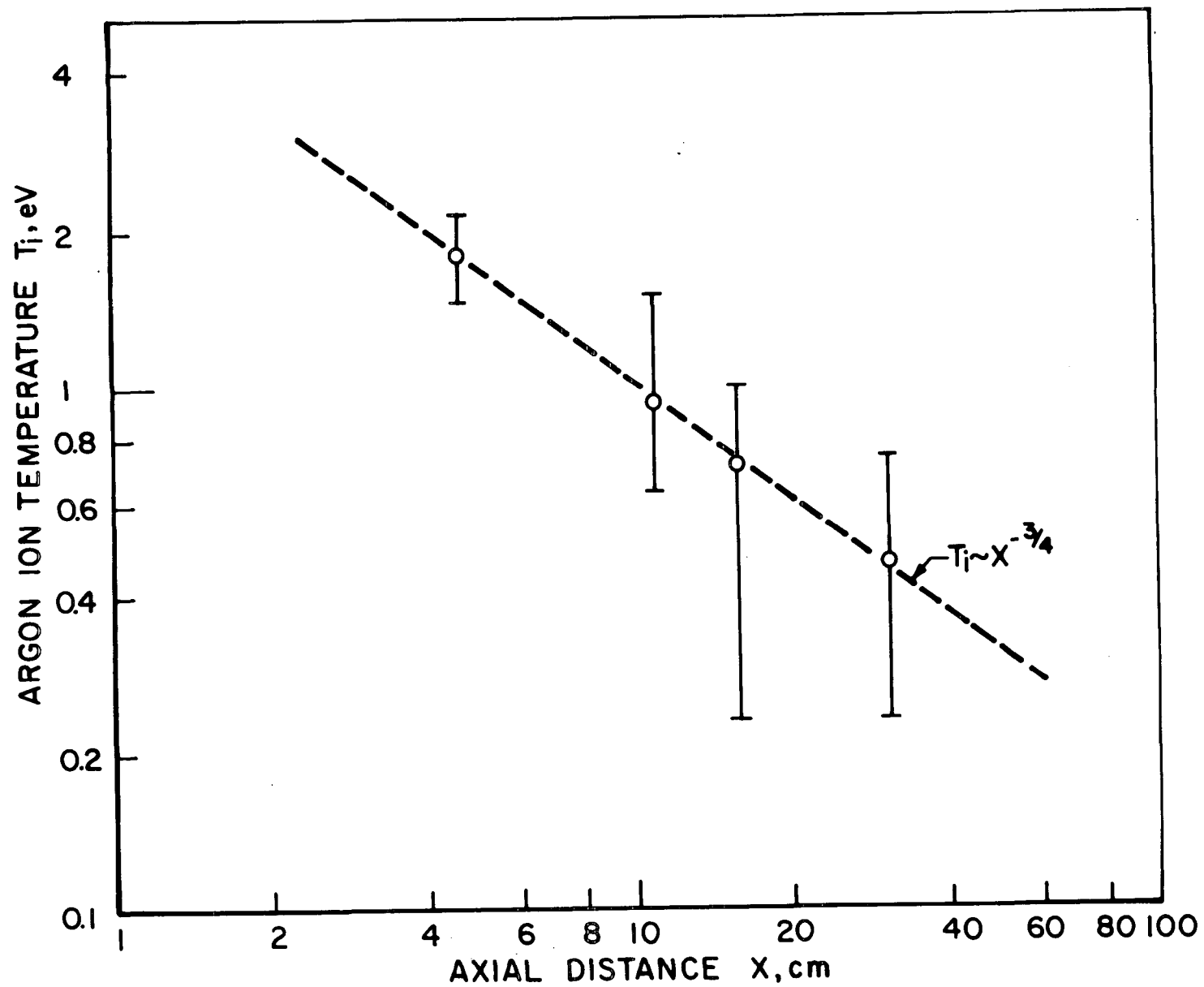
FIGURE 4-20
AP25.4813

97

DEVELOPMENT OF ION TEMPERATURE IN ARGON JETS

directed kinetic energy is being recovered from random thermal energy. Whether the change in ion temperature is sufficient to explain the observed increase in velocity will be examined in Chapter 5.

Electron Temperatures

Very few data on electron temperature profiles in the exhaust plume exist at this time. Turchi[8,9] has measured electron temperatures with Langmuir probes at several locations inside the arc chamber and just outside the exit plane. His results indicate that the electron temperature is essentially constant throughout the regions investigated and has a value between 1.5 and 2 eV. Using double electrostatic probes Boyle[28] has recently measured the electron temperature on the locus of maximum luminous intensity in one of the argon jets, 25.4 cm from the chamber exit, and found a value of about 0.8 eV. Comprehensive radial and axial surveys have not yet been made, but indications are that the electron temperature on the axis, at least at $x = 25.4$ cm, is about the same as in the argon jets, and that it increases axially towards the exit plane.[53] It would thus appear that the electron temperature is radially quite uniform everywhere and that it decreases slowly with increasing distance from the chamber.

4-5   IMPURITY VELOCITIES AND TEMPERATURES

Unfortunately, a spectroscopic measurement of the velocities and temperatures of the products of ablation (CII, NII, OII, HI) in the core of the exhaust and in the gaps between the argon jets has not proved feasible with the Fabry-Perot system. This is because of the lack of suitable isolated spectral lines of these impurities within the useful spectral range of the reflective coatings on the Fabry-Perot plates. The impurity lines tend to crowd together at separations of the

order of the free spectral range or less and would thus be impossible to identify in the Fabry-Perot scan. Attempts at measuring impurity velocities have been made by using the Steinheil spectrograph,[18] but the dispersion of this instrument is not high enough even in the blue end of the spectrum to yield accurate quantitative results. However, the results of that investigation do indicate that the velocities in the core flow are considerably higher than in the argon jets, possibly as high as $4 - 5 \times 10^4$ m/sec.

CHAPTER 5

ARGON ACCELERATION MECHANISMS

5-1 INTRODUCTION

The experimental velocity measurements described in the preceding chapter indicate that almost half the final argon exhaust velocity of 1.65×10^4 m/sec is achieved in an acceleration region downstream of the arc chamber exit. It has variously been suggested that acceleration in the exhaust downstream of the chamber may be a result of fringing electromagnetic fields[10] or of recovery of directed kinetic energy from thermal energy via gasdynamic flow expansion.[13] A momentum exchange between the core flow of ablation products and the argon jets is also a possibility.

The flow dynamics of the MPD exhaust plume would be very complicated even without the complex species structure the exhaust is now known to have. Highly non-equilibrium conditions characterize the entire flowfield, and species in various stages of ionization are present. Close to the chamber exit are found regions of significant current conduction and self-magnetic fields. The exhaust flow, once outside the arc chamber, is unbounded and far enough downstream is expected to exhibit behaviour typical of free jet expansions. Theoretical investigations of the flow of high enthalpy plasmas into a vacuum have been carried out by some investigators, but usually with many simplifying assumptions.[54] In the present case there is the added complication of the radial and azimuthal species inhomogeneity and resulting non-uniformity in the atomic weight of the particles in the flow-field. A complete theoretical analysis of the MPD exhaust flow is not within the context of this dissertation. Instead simple arguments are developed for the evaluation of the relative roles of the three possible argon acceleration mechanisms pointed out above.

5-2 FRINGING ELECTROMAGNETIC FIELDS

An estimate of the role of the $\vec{j} \times \vec{B}$ body forces in
the flow acceleration downstream of the anode plane can
be obtained from a simple comparison of the magnetic, gas-
kinetic, and dynamic pressures in the acceleration region,
which lies approximately between $x \approx 5$ cm and $x \approx 15$ cm.

Magnetic Pressure

Clark[4] has obtained maps of the magnetic field strength
in and around the discharge chamber of the MPD accelerator.
Figure 5-1 displays the contours of self-induced magnetic
fields obtained at a current of 16 kA and an argon mass
flow of 6 g/sec. The actual field is, of course, azimuthal.
Superimposed on these contours is the approximate location
of an argon jet. It can be seen that at $x \approx 5$ cm in the jet
$B \approx 3 \times 10^{-3}$ Weber/m^2, which is about two orders of magni-
tude less than in the vicinity of the cathode. The magnetic
pressure at this axial location in the jet is thus[14]

$$ p_m = \frac{B^2}{2\mu_o} \approx 4 \text{ Ntn/m}^2 $$

where $\mu_o = 4\pi \times 10^{-7}$ henry/m is the magnetic permeability
of free space. Downstream of this location B decays rapidly
and thus so does p_m — at $x = 6$ cm p_m is nearly an order of
magnitude smaller than at $x = 5$ cm.

Gaskinetic Pressure

To estimate the gaskinetic (static) pressure it will
be assumed that the electron and ion temperatures at $x = 5$ cm
are equal and have a value of ~1.7 eV (2×10^4 °K) as
measured for the argon ions. (Chapter 4, Sect. 4-4).
Particle densities are estimated on the basis of electron
density measurements obtained from Stark width measurements
of the H_β line.[15] Figure 5-2 reproduces a map of electron
density contours obtained at 16 kA and 6 g/sec. The approx-
imate location of an argon jet is superimposed. At $x = 5$ cm

FIGURE 5-1
AP25-4860

(+)

APPROXIMATE LOCATION
OF ARGON JET

r, cm

5

$B_\theta = .001 \, w/m^2$

.05

.02

.10

.01

.003

.002

.20

(−)

0

X, cm

5

10

0

102
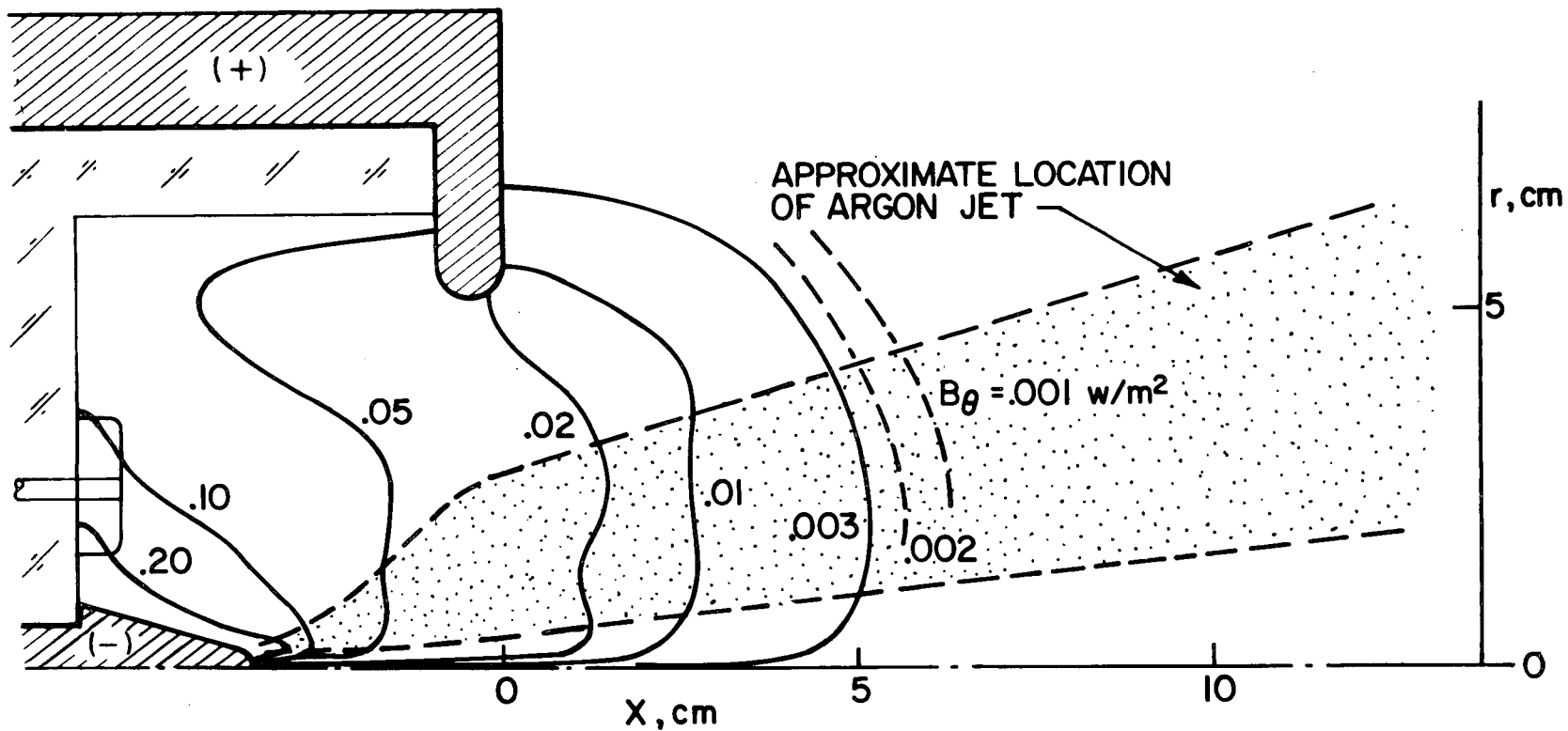
MAGNETIC FIELD STRENGTHS IN MPD ARC

APPROXIMATE LOCATION OF ARGON JET

$n_e = 1.0 \times 10^{15} \, cm^{-3}$

ELECTRON DENSITY CONTOURS
$J = 16 \, kA$, $\dot{m} = 6$ g/sec

FIGURE 5-2
AP25·4861

103
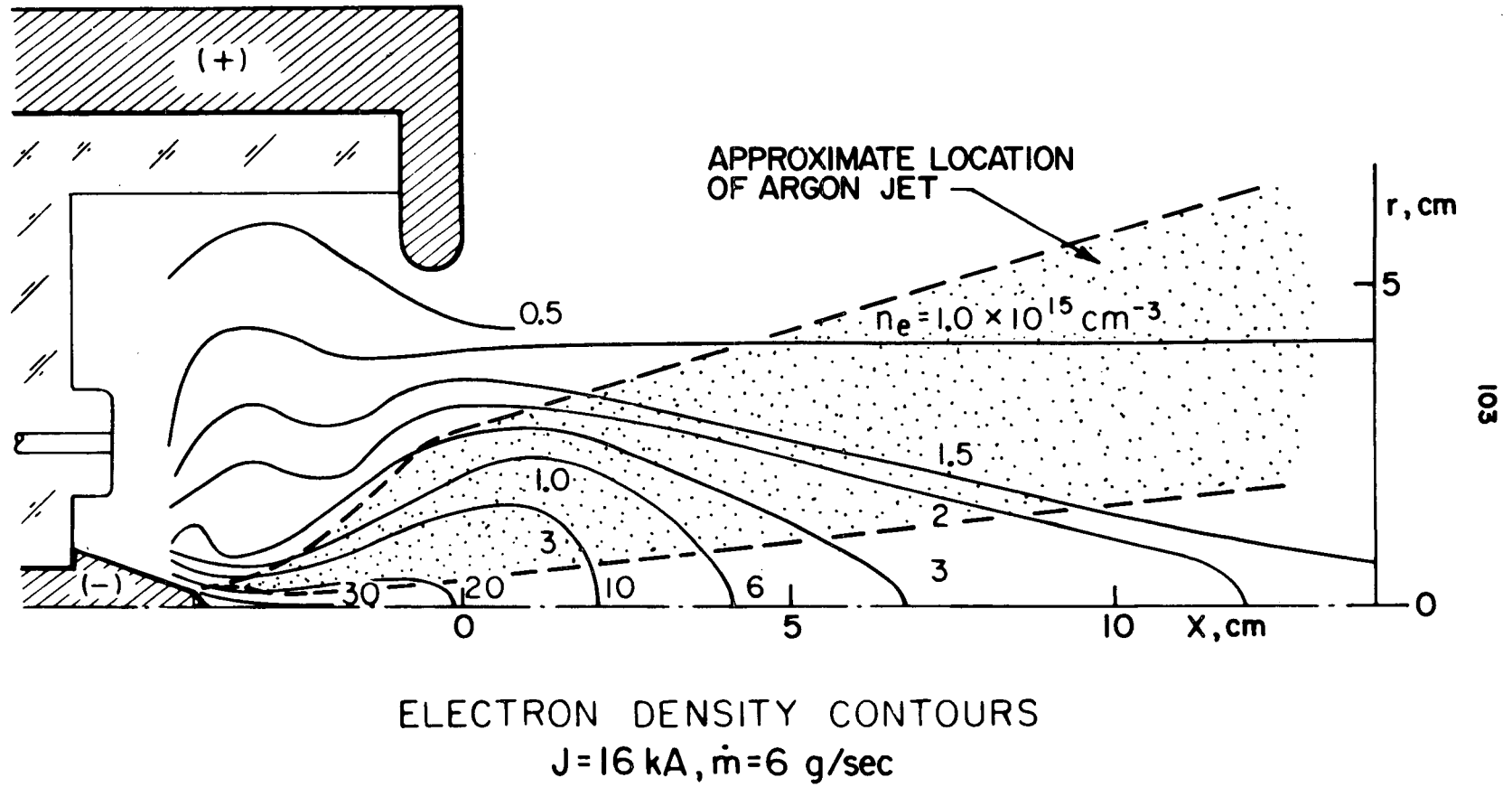
the electron density n_e has an average value of about 2×10^{15} cm^{-3} in the argon jet. Although nonequilibrium conditions generally prevail throughout the flow-field, in order to approximate the heavy particle number density it will be assumed that Saha equilibrium exists at this location in the jet. At the conditions of $T \approx 2 \times 10^4$ $^{\circ}$K and $n_e \approx 2 \times 10^{15}$cm^{-3}, equilibrium thermodynamic tables[55] indicate that the density, n_i, of singly ionized argon is $\sim 7 \times 10^{14}$ cm^{-3} and the density, n_{ii}, of doubly ionized argon is $\sim 8 \times 10^{14}$ cm^{-3}. The number densities of neutral atoms and triply ionized atoms are negligible.

The static pressure, p_s, is calculated from the ideal gas law:

$$p_s = \left(n_i + n_{ii} + n_e \right) kT$$
$$\approx 10^3 \text{ Ntn/m}^2$$

where k is Boltzmann's constant, 1.38×10^{-23} joules/$^{\circ}$K.

Dynamic Pressure

Although experimentally measured radial profiles of impact pressure at several axial stations are available,[10] there are no data at x = 5 cm. The dynamic pressure can be obtained by interpolating between existing profiles and subtracting the calculated static pressure; however, both the axial and radial impact pressure profiles are steep near x = 5 cm making interpolation difficult and inaccurate. A simple way to calculate the dynamic pressure, p_d, is through the relation $p_d = \rho u^2$, where $\rho = m_i (n_i + n_{ii})$ is the mass density, m_i is the atomic mass of argon, and u is the flow velocity. Using the measured average argon velocity – 8.5×10^3 m/sec – at x = 5 cm and the previously calculated particle densities at this location one obtains

$$p_d \approx 10^4 \text{ Ntn/m}^2$$

Comparison of Pressure Components

The preceding calculations show that the magnetic
pressure is more than two orders of magnitude less than the
gaskinetic pressure and three orders of magnitude less than
the dynamic pressure at x = 5 cm, i.e:

$$p_m \ll p_s \ll p_d$$

It can be shown that with increasing x, p_m decreases faster
than p_s or p_d, so that this relation remains valid for x > 5 cm.
The smallness of the magnetic pressure term in comparison
with the other pressure components clearly indicates that
electromagnetic body forces play a negligible role in the
acceleration of the argon plasma in the exhaust in the region
of interest.

5-3 ELECTROTHERMAL CONVERSION

It is conceivable that the observed acceleration in the
argon jets is a result of the conversion of thermal energy to
directed kinetic energy via the free flow expansion processes.
In the preceding chapter it was ascertained that both the ion
and electron temperatures decrease with increasing distance
from the arc chamber exit. The ion temperature, T_i, was shown
to have a functional dependence on distance, x, of the form
$T_i \sim x^{-3/4}$. The exact functional behaviour of the electron
temperature, T_e, is not known at this time. Therefore a simple
approximation will be used: the known value of $T_e \approx 0.8$ eV at
x = 25.4 cm and the assumed value of $T_e \approx 1.7$ eV (based on the
results of Turchi[8]) at x = 5 cm are plotted on full logarith-
mic graph paper and the function is approximated by a straight
line between the two points. The slope of this line turns out
to be very nearly -1/2, and thus the approximate dependence of
electron temperature on distance is $T_e \sim x^{-\frac{1}{2}}$, with $T_e \approx T_i$ at
x = 5 cm.

A simple stream tube model can be used to estimate whether
the decrease in T_i and T_e beyond x = 5 cm is sufficient to
account for the increase in flow velocity along the argon jets.

It is assumed that the flow in each argon jet is one-dimensional, i.e: that each argon jet is a stream tube with uniform average flow properties at any cross section. Interactions with the adjacent flow of ablation products are neglected as are radiation and conduction effects. In addition, it is assumed, as was done previously, that the flow is in Saha equilibrium at x = 5 cm. No assumptions about its state downstream of this location need be made at this time. Considering the true complex nature of the flow-field the foregoing assumptions are admittedly crude; however, enough of the essential physics is retained that the results will be meaningful in an approximate sense.

The one-dimensional energy equation for continuum adiabatic flow in an argon jet, under the above assumptions is[56]

$$h_T = h + \frac{u^2}{2} = const.$$

where h_T is the total enthalpy, h is the static enthalpy, and u is the flow velocity at a given cross section of the jet.

Energy Inventory

The static enthalpy of a gas is given by $h = e + p/\rho$ where e is the internal energy, p is the static pressure, and ρ is the mass density. The internal energy consists of the random thrmal energy of translation, e_{tr}, of the ions and electrons, the enrgy of excitation, e_e, of the atoms and ions, and the energy, e_i, of ionization of the atoms and ions. Thus,

$$h = e_{tr} + e_e + e_i + \frac{p}{\rho}$$

Using the experimental data under the assumption of Saha equilibrium the components of h are easily calculated with the help of tables of thermodynamic properties of argon[55]. At x = 5cm the results are as follows, expressed in units of electron volts per heavy particle:

Translational energy: $e_{tr} \approx 6.6$ eV

Excitation energy: $e_e \approx 0.9$ eV

Ionization energy: $e_i \approx 31$ eV

Flow work: $p/\rho \approx 4.3$ eV

Thus the static enthalpy per heavy particle at x = 5 cm is

$$h \approx 43 \text{ eV}$$

At this location $u \approx 8.5 \times 10^3$ m/sec, and the directed kinetic energy, $\frac{1}{2} m_i u^2$, per argon ion is ~15 eV. Consequently, the total enthalpy per argon ion at x = 5 cm is

$$h_T = h + \frac{m_i u^2}{2} \approx 58 \text{ eV}$$

The final exhaust velocity of the argon jets is 1.65×10^4 m/sec, which corresponds to a kinetic energy per heavy particle of 57 eV. It is apparent, therefore, that in the absence of other acceleration processes the entire thermal energy content of the flow in the argon jets present at x = 5 cm must be recovered as directed kinetic energy to produce the observed final argon exhaust velocity.

This, however, does not appear to be the case. Discharge spectra obtained at several axial locations in the exhaust plume (Chapter 3, Section 3-3) reveal no evidence of neutral argon, whose spectral lines should be visible if there is significant recombination of the singly ionized argon, AII. Furthermore, AII radiation persists far downstream. These facts immediately imply that 15.8 eV (the first ionization potential of argon) per heavy particle are not available for conversion to directed kinetic energy. If only this energy of first ionization is non-recoverable as streaming energy, and if all the other components of the enthalpy are, it turns out that the available enthalpy at x = 5 cm would lead to a final argon velocity of ~1.4×10^4 m/sec, which is within 15% of the measured value, a tolerable discrepancy in view of the rather drastic assumptions made in the analysis so far. If this result is to hold it must

first be determined whether the energy of second ionization
is recoverable.

Recombination of AIII to AII

Although there is no evidence of AII recombination,
indications are that there may be some recombination of AIII
to AII. For example, the 4880 $\overset{o}{A}$ AII line intensity mea-
surements in Chapter 4 reveal a line of sight integrated
intensity which varies as x^{-2} along each argon jet. Because
of the axial decrease in electron temperature as $x^{-\frac{1}{2}}$ and
the exponential dependence of excitation on this temperature,
the line intensity would decrease much faster than x^{-2}
unless the upper level of the 4880 $\overset{o}{A}$ spectral transition
were populated by cascading transitions from higher energy
levels of AII. Such cascading would be a natural consequence
of three-body recombination from the next higher level of
ionization, namely AIII.

Under the conditions of temperature and particle density
prevailing in the exhaust plume of the MPD arc the dominant
recombination mechanism is indeed that of three-body
electron-electron-ion collisions.[57-69] The energy re-
leased by the recombination of an ion of AIII to an ion of
AII is simply equal to the second ionization energy of
argon. Some fraction of this energy is emitted as radiation
and the rest is transferred to the electron gas via super-
elastic electron-ion collisions. The relative magnitude of
the two effects depends largely on whether or not the plasma
is optically thin to the emitted radiation.[59-63,68-71]
Because the treatment of even one-dimensional recombining
flows with only one ionic specie present is a matter of con-
siderable complexity, a full analytical solution of the prob-
lem has not been attempted. Instead, a semi-empirical ap-
proach based on the available experimental data has been
used to estimate the fraction of recombination of AIII to
AII whithin the acceleration region in the argon jets. The
details of the calculation are discussed in Appendix C.

The results of the calculations indicate that only about 7% of the second ions present at x = 5 cm recombine downstream. If the entire energy of this fractional recombination were recovered as random thermal energy of the electrons and ions, and subsequently as streaming energy, only about 1 eV per heavy particle would be regained - an insignificant amount. Actually, under the conditions prevalent in the argon jets, more than half the recombination energy is lost as radiation, as can be ascertained through calculations similar to those of Fraser et al.[73]

It is clear, therefore, that neither the energy of first or second ionization is recovered in the flow expansion, so that frozen flow conditions prevail in the argon jets, and very likely in the entire exhaust plume. Only the enthalpy of the random thermal motions of the electrons and ions is available. The total velocity increment resulting from the complete conversion of this enthalpy ($\sim$11 eV) into streaming motion downstream of x = 5 cm is $\sim 2.7 \times 10^3$ m/sec, which is less than 35% of the observed increment of $\sim 8 \times 10^3$ m/sec.

One factor which has not been taken into account in the calculations above is the contamination of the argon jets by the ablated impurities. In Chapter 3 it was seen that while the heavy impurities such as carbon, oxygen and nitrogen do not appear to penetrate the argon jets to a great extent, the hydrogen does as a result of its high mobility. The presence of hydrogen in the argon jets effectively lowers the average atomic weight of the plasma in the jets, allowing gasdynamic expansion of the flow to higher final velocities than pure argon can achieve. However even if there were a hydrogen atom or ion for every argon ion in the argon jets, thus lowering the average atomic weight from 40 to about 20, gasdynamic expansion would yield a velocity increment of 5×10^3 m/sec, which is still considerably short of the observed 8×10^3 m/sec. Such a concentration of hydrogen in the argon jets would require an ablation rate of more than one-third the injected mass flow rate of argon. In fact,

indications are that the ablation rate does not exceed about
15% of the input mass flow at the 16 kA, 6 g/sec operating
condition, implying that the average atomic weight in the
argon jets is closer to 30 than to 20. Thus the velocity
increment through electrothermal conversion is at most only
half the observed value.

5-4 MOMENTUM TRANSFER FROM THE ABLATED FLOW

A possible explanation for the large increase in velo-
city downstream of x = 5 cm in the argon jets can be found
in the centerline time-of flight velocity profile reported
in Ref. 11, which is shown here in Fig. 5-3. According to
the results of Chapter 3 this profile corresponds to the
velocities of the ablation products along the centerline,
since there is no argon in the core of the exhaust plume.
The velocity of the impurities on the centerline is consi-
derably higher than that of the argon in the jets, a conse-
quence, most likely, of the much lower average atomic weight
of the ablated products ($M_{abl} \approx 6.7$ vs. M = 40 for argon).
There is, of course, the possibility that an ion-acoustic
wave component is superimposed on the convective velocity
of the ablated flow. Unfortunately, as pointed out in
Chapter 4, a spectroscopic measurement of the centerline
velocity profile was not possible; however at this stage
it is not so much the exact magnitude of the centerline
velocity profile that is important, but rather the curious
dip in the profile in the region between about x = 5 cm
and x = 15 cm. It has been suggested that this may be a
result of the superposition of a decreasing wave velocity
profile and an increasing convective velocity profile.[74]
However, it is interesting to note that this pronounced
dip occurs over precisely that axial interval over which
the argon in the jets undergoes the bulk of its downstream
acceleration. It is tempting to conclude from this that there
is a transfer of axial momentum from the fast core flow of
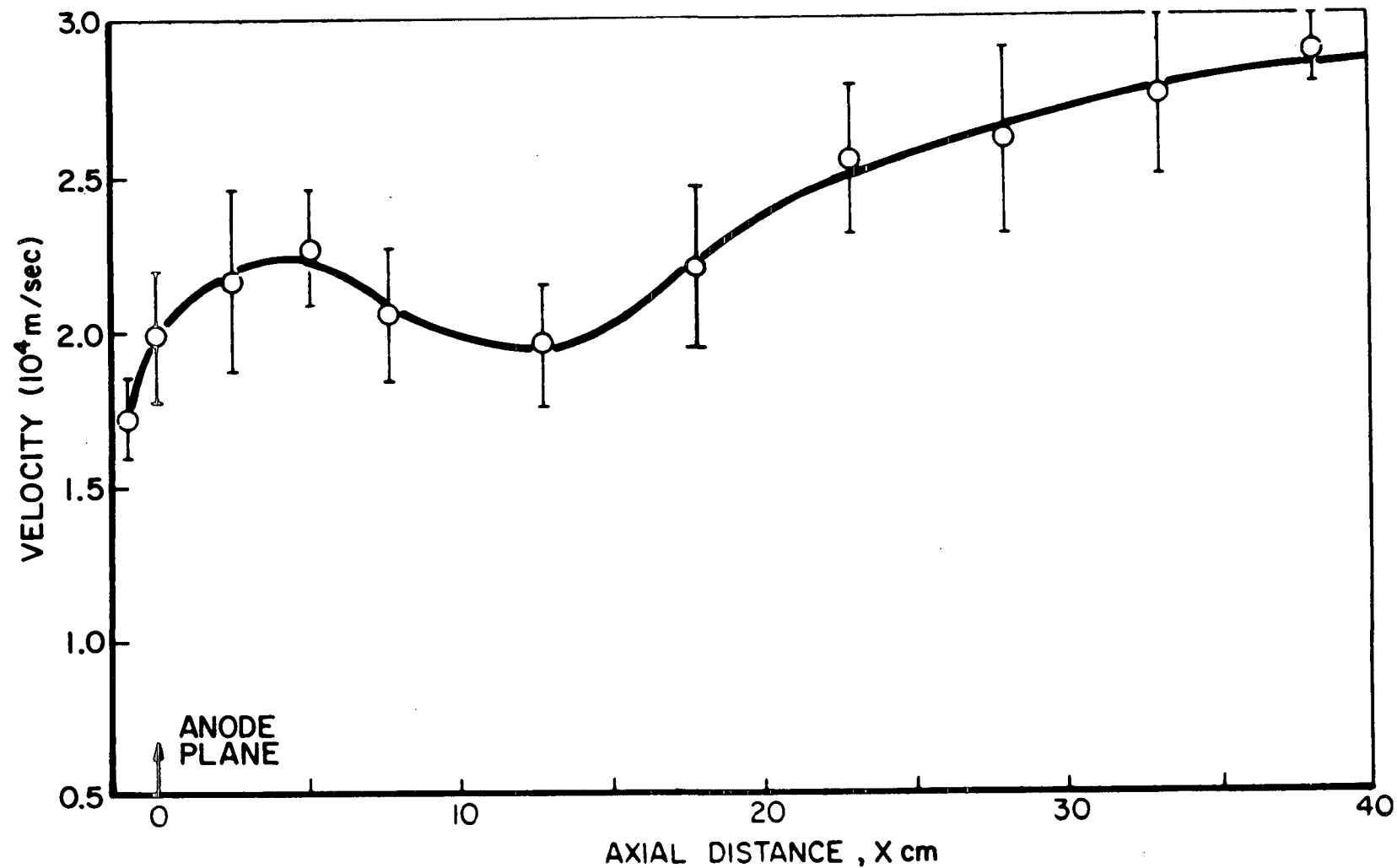
TIME - OF - FLIGHT VELOCITIES ALONG CENTERLINE

FIGURE 5-3
AP25.4862

ablation products to the slower argon jets in the axial interval where the centerline profile shows the velocity defect. The increase in centerline velocity beyond the dip could then be interpreted as due to an effective decoupling of the ablated and argon jet flows resulting from the rapid drop in particle number density caused by the free flow expansion. Once decoupled, the ablation products and the argon would continue to expand independently, attaining final velocities which are functions of their respective atomic weights.

Indications are that the flow in the exhaust plume is turbulent rather than laminar,[11,28] so that the momentum transfer mechanism may be turbulent shear stress between the impurity and argon jet flows. The analysis of the interaction of two concentric supersonic turbulent jets of different atomic weight is in itself formidable.[75] In the present case the problem is complicated by the azimuthal non-uniformity of the argon and impurity flows and the resulting non-uniformities in atomic weight and velocity profiles. The other complications accompanying freely expanding flows of high enthalpy plasmas, as discussed earlier, are also present. Furthermore, in the axial interval of interest there are no detailed experimental radial or azimuthal profiles of impurity and argon velocity and concentration available with which to compare theoretical predictions. It is pointless, therefore, to attempt a detailed analytical treatment at this time.

At present the momentum transfer hypothesis is at best speculative because of its reliance on the time-of-flight velocity measurements, which may not reflect the true streaming velocity of the ablated flow on the centerline. The proposed mechanism of argon acceleration must therefore remain purely conjectural until the problem of insulator ablation is eliminated. Spectroscopic velocity measurements on an uncontaminated argon exhaust should resolve whether the presently observed argon velocities are largely the result of interaction with the flow of ablation products, or of some other as yet unspecified acceleration mechanism.

CHAPTER 6

SUMMARY AND CONCLUSIONS

The photographic and spectroscopic investigations of the structure of the exhaust plume and of the exhaust velocities and temperatures of argon have provided important new information on some of the physical processes occurring in the quasi-steady MPD accelerator. A hitherto unsuspected azimuthal and radial structure in the spatial distribution of the injected argon has been found to exist in the discharge region and exhaust plume, under the standard operating conditions of 16 kA current and 6 g/sec argon mass flow. Singly ionized argon, the dominant radiating specie of the propellant, is distributed in six discrete jets which are azimuthally in line with the six mass injector ports and retain their identity for several anode orifice diameters downstream of the chamber exit. The gaps between the jets, which have been shown to be devoid of any specie of argon, are occupied by impurities - carbon, hydrogen, oxygen - ablated from the Plexiglas insulator end wall of the arc chamber. Operation of the arc at overfed conditions reduces the amount of the ablated material in the exhaust and causes the argon distribution to become more uniform. Operation at starved conditions substantially increases the erosion rate of the Plexiglas insulator and exacerbates the complex species structure in the exhaust.

The insulator ablation, which is responsible for the complex exhaust structure, occurs over regions of argon starvation between the injectors. Kerr-cell photographs of the early stages of the discharge indicate that the onset of ablation is a relatively slow process compared to current pattern stabilization, requiring about 150 μsec to achieve a steady state, as compared to 30 μsec for the

current. The species structure of the exhaust reflects this growth of ablation, and does not develop its full structure until about 150 μsec into the current pulse. Simple calculations indicate that the replacement of the Plexiglas insulator by a refractory material such as quartz will not entirely eliminate the erosion problem but will reduce it significantly and confine it to the immediate vicinity of the cathode base, where the radiative and conductive heat fluxes to the insulator are very high.

Extensive time-resolved spectroscopic measurements of the velocity and temperature of singly ionized argon in the jets have been carried out by means of a versatile scanning Fabry-Perot spectrometer system. The average argon ion velocity in the jets has been found to increase monotonically from $\sim 8.5 \times 10^3$ m/sec 5 cm from the chamber exit, to a plateau of $\sim 1.65 \times 10^4$ m/sec about 40 cm downstream. This final velocity is considerably in excess of the Alfvén critical speed for argon, indicating the possibility of attaining much higher specific impulses with this propellant than the limits claimed by other investigators.[30] Measurements of spectral line widths, suitably corrected for broadening mechanisms other than the thermal Doppler effect, have revealed an argon ion temperature profile in the jets which downstream of x = 5 cm scales as $x^{-3/4}$, where x is the distance from the chamber exit. Typical temperatures are 1.7 eV at x = 5 cm and 0.5 eV at x = 25 cm.

An evaluation of possible acceleration mechanisms, based on these and other data (such as magnetic field profiles and electron temperatures) has indicated that neither body forces from fringing electromagnetic fields nor simple electrothermal conversion of the random thermal energy of the argon plasma are sufficient to account for the high velocities attained by the argon in the jets. Calculations of the recombination rate of doubly ionized argon have revealed that less than 10% of the AIII present at x = 5 cm

recombines downstream, and the spectroscopic studies have
shown no evidence of recombination of the singly ionized
specie. These facts indicate that very little ionization
energy is recovered as streaming energy.

A comparison of a centerline time-of-flight velocity
profile[11] with the velocity profile in an argon jet
suggests that a transfer of momentum from the fast core
flow of ablation products to the slower argon jets may
be the principal argon acceleration mechanism. If this
is indeed the case it might be expected that in the absence
of the light impurities the argon exhaust velocity would
be lower than that observed in the present investigation.
However, it may well be that some other acceleration mecha-
nism not yet considered may be responsible for the high
observed argon exhaust velocity.

It is clear that the ablation of the insulator end
wall of the arc chamber must be eliminated or at least
drastically reduced as a prelude to further research and
development of the quasi-steady MPD accelerator. It has
been recently determined in this laboratory[28,81] that
this can be done through a suitable choice of injector
geometry and insulator material. The use of annular in-
jector slits, rather than discrete orifices, has been
found not only to significantly reduce the rate of abla-
tion but also to give rise to an azimuthally uniform dis-
tribution of the injected argon in the exhaust plume.
The latter is a fortuitous result, as it will permit the
reduction of future spectroscopic observations to local
properties via Abel inversion techniques[16] Velocity
and temperature measurements on an uncontaminated axially
symmetric exhaust plume should resolve the nature of the
argon acceleration processes present downstream of the
discharge chamber.

APPENDIX A

ABLATION PHENOMENA

A-1 INTRODUCTION

It is evident from the discussions in Chapter 3 that
the ablation of the Plexiglas end-wall of the arc chamber
has a profound effect on the structure of the exhaust plume
of the MPD arc. Time-resolved Kerr-cell photographs of the
arc chamber interior taken during the first 160 μsec of the
discharge at 16 kA and 6 g/sec, indicate that the onset of
the insulator ablation is a relatively slow process requiring
about 150 μsec for stabilization, compared to about 30 μsec
for current pattern stabilization. A sequence of such photo-
graphs obtained at 13,21,40,100, 132 and 150 μsec into the cur-
rent pulse is shown in Fig. A-1. Note the radial and axial
dimensions of the luminous layer of ablation products at the
surface of the end-wall. At 13 μsec the luminosity at the
wall is just visible near the cathode base. At 21 μsec it is
still within the radius of the injectors. At 40 μsec the
layer around the base of the cathode extends axially halfway
to its tip and radially to about the injector orifices. Be-
tween t = 40 μsec and t = 100 μsec the luminous layer grows con-
siderably, developing its characteristic star-shaped pattern.
The bright scalloped area surrounding the cathode is the "core"
of the star-shaped layer, while the fainter extensions are the
arms viewed side-on. (Cf. Fig. 3-12) As time increases, so
does the extent of this layer of ablation products. At 150
μsec the arms of the star reach the cylindrical side-wall and the
downstream "boundary" reaches the level of the cathode tip. The
layer maintains this visual configuration throughout the remainder
of the current pulse. This growth of ablation can be explained by
a simple qualitative physical model. After breakdown and current
stabilization the self-field body forces deplete argon from
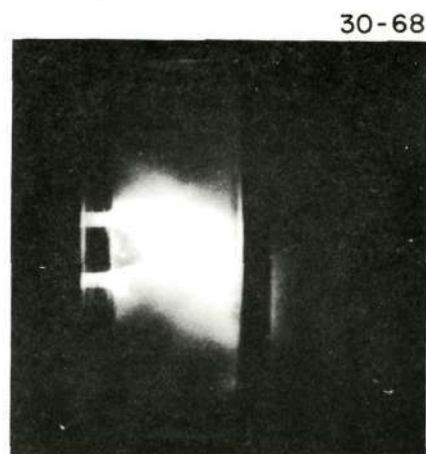
30-68

a) t = 13 μsec

30-69

b) t = 21 μsec

30-70

c) t = 40 μsec

30-73

d) t = 100 μsec

30-74

e) t = 132 μsec

30-75

f) t = 150 μsec

FIGURE A-1
AP25·P·476

117
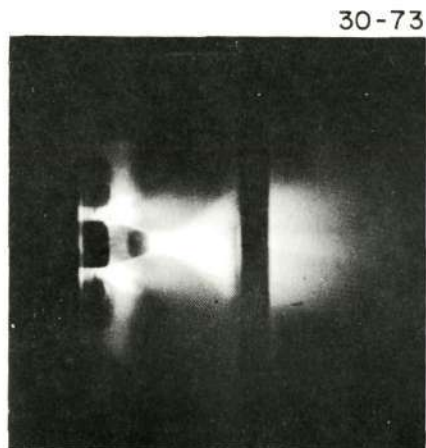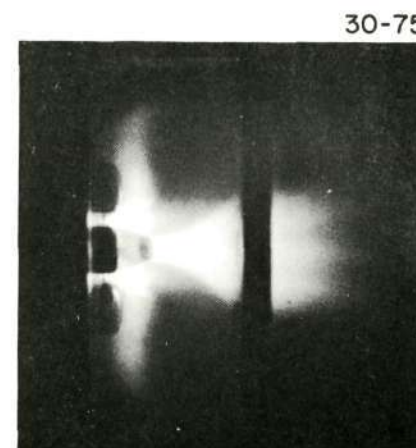
SEQUENCE OF KERR-CELL PHOTOGRAPHS OF DISCHARGE
(EXPOSURE TIME = 5 μsec)
J=16 kA, $\dot{m}$=6 g/sec

the regions between the injectors at the Plexiglas wall, forcing the current pattern near the surface to ablate the insulator material in order to satisfy the local mass flow requirements. Near the Plexiglas surface the current density is essentially radial, and hence inversely proportional to the radius. It is thus most intense at the cathode base. Consequently, the initial argon fill in the chamber is most quickly depleted in this region and ablation of the end-wall first begins at the cathode base. The radius of argon depletion increases with time, eventually reaching the side walls of the arc chamber. At this time, about 150 µsec into the discharge, the total ablation rate reaches a steady state. Because the argon enters the chamber through injectors extending 6 mm downstream of the Plexiglas insulator, very little of it reaches the surface between the injectors and consequently the discharge remains starved there. At the injectors, on the other hand, there is sufficient argon and ablation is much less severe.

A-2 POSSIBLE ABLATION PROCESSES

Insulator ablation phenomena similar to those reported here have been observed in a variety of different electric discharge devices such as Z-pinches and electromagnetic shock tubes.[76,77,78,79,80] Various heating mechanisms for the insulator walls have been proposed. Keck[76] working with a magnetic annular shock tube has suggested heavy particle heat conduction; Colgate[77], studying pinch discharges, has proposed electron heat conduction (taking the gas to be fully ionized right up to the wall); Ashby[78], also working with a pinch device, has felt that radiation would be the dominant heat transfer process; finally, Workman[79] in an investigation of ablation effects in a magnetic piston shock tube has suggested the possibility of electron-ion recombination at the insulator surface as an important heating mechanism. It is likely that all the above processes play some role in insulator ablation. The dominant mechanism probably depends on the nature and geometry of the discharge.

In the MPD arc under investigation here it is believed
that conductive heat transfer from a thin layer of resis-
tively heated plasma adjacent to the insulator surface plays
a significant role in the ablation process. The current
density at the surface is apparently much higher than any-
where downstream at a given radius. For example, Fig. A-2
shows the axial variation of the radial component of steady-
state current density at a radius equal to that of the cath-
ode base. These data were reduced from detailed current con-
tours similar to the ones shown in Fig. 2-6b.[18]. It can
be seen that there is an abrupt rise in the current density
to more than 2000 A/cm^2 within a layer about 2 mm thick next
to the end wall. At such current densities the power dis-
sipated by ohmic heating of the plasma in the thin layer is
considerable. It is known from plasma potential and current
conduction patterns that the current conduction near the
Plexiglas insulator is largely scalar[11], therefore the
plasma resistivity η can be calculated approximately
from[14]

$$\eta = 6.53 \times 10^3 \, \frac{\ln \Lambda}{T^{3/2}} \quad \text{ohm-cm}$$

where T is the plasma temperature and $\ln \Lambda$ is a weak func-
tion of density and temperature, equal to about 6 for
$T \sim 1$ eV and $n_e \sim 10^{15}$ cm^{-3}. For a temperature of about
1.5 eV[8], $\eta \approx 1.5 \times 10^2$ ohm-cm. Thus the power dissipated
at the base of the cathode, where $j \approx 2000$ A/cm^2, is

$$P = \eta j^2 \approx 6 \times 10^4 \quad \text{W/cm}^2$$

Because the current varies inversely with radius the ohmic
heating is proportional to the inverse square of the radius
in the thin layer at the wall, as shown in Fig. A-3, and is
thus down to about 9×10^3 W/cm^3 at the radius of the injectors.
Some fraction of the heat generated is convected downstream
by $\vec{j} \times \vec{B}$ body forces, and the rest is conducted into the wall
raising its temperature to the ablation point. The relative
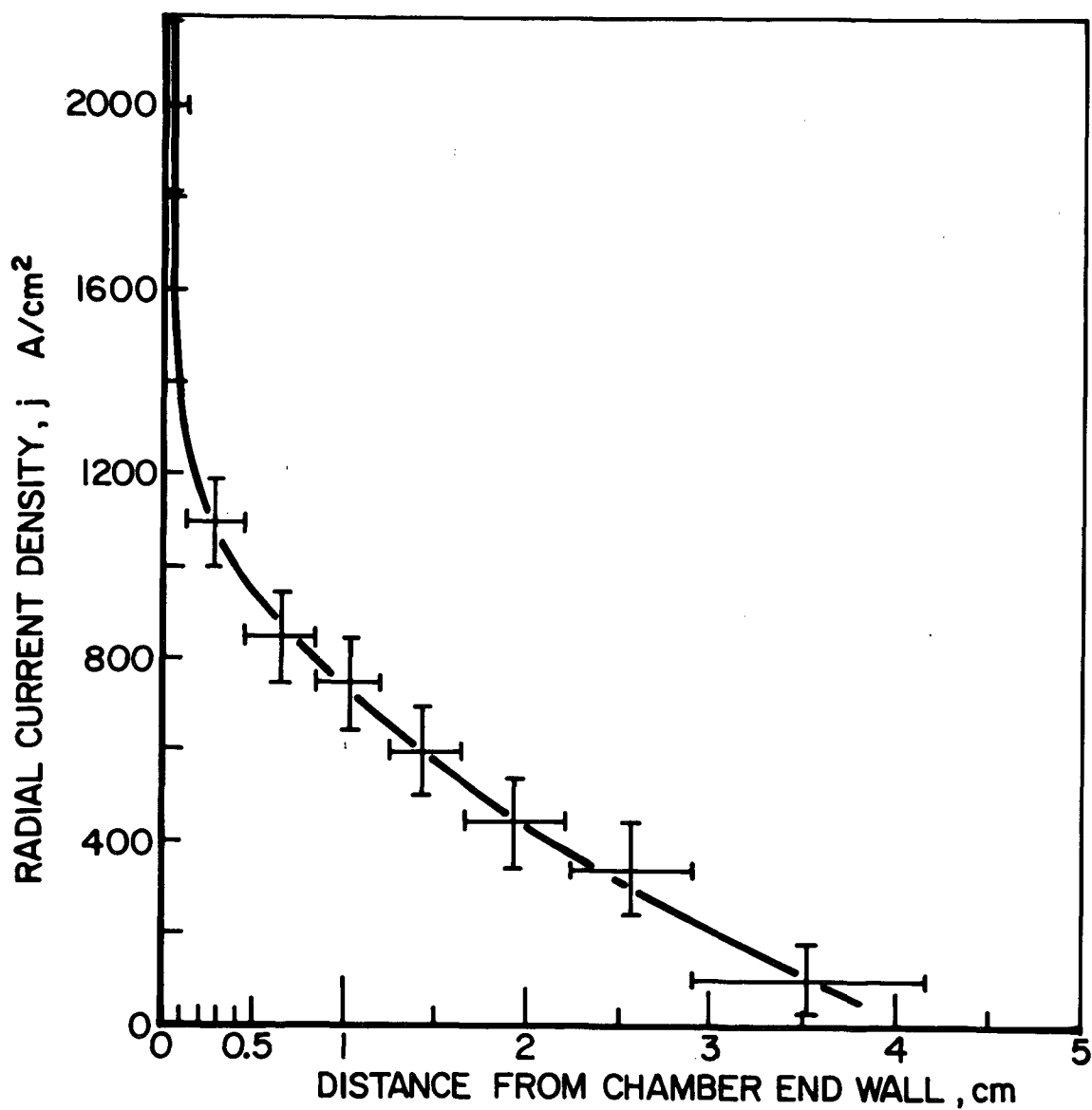
DEVELOPMENT OF RADIAL CURRENT DENSITY
IN THE CHAMBER AT r = 0.95 cm
J = 16 kA , ṁ = 6 g/sec

FIGURE A-2
AP 25·4850

j_c, P_c : CURRENT DENSITY AND OHMIC HEATING
AT RADIUS OF CATHODE BASE

RADIUS OF
PYREX CHAMBER WALL

$\dfrac{j}{j_c}$

RADIUS OF INJECTORS

APPROX. LIMIT OF $j \sim \dfrac{1}{r}$

$\dfrac{P}{P_c}$

CATHODE
RADIUS

RADIUS, r cm
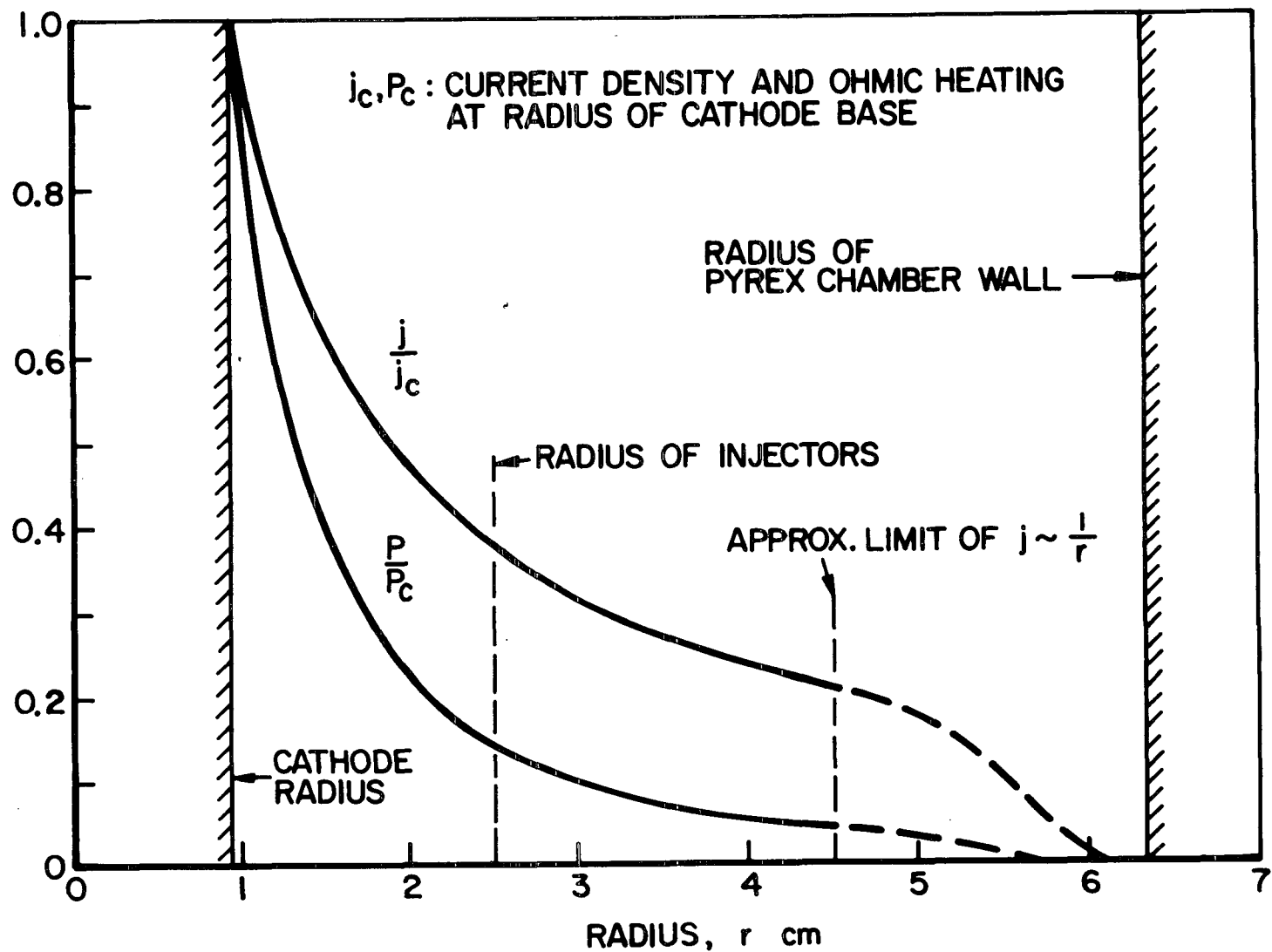
NORMALIZED CURRENT DENSITY
AND OHMIC HEATING PROFILES AT PLEXIGLAS END WALL

magnitudes of these fractions is not known at present. A complicating factor is that the intense radiation emanating from the small volume of continuum emission just downstream of the tip of the cathode appears also to play a significant role in the ablation of the Plexiglas. This can be seen in Fig. A-4 which shows a photograph of the Plexiglas plate removed from the chamber but with the cathode and the injectors still in place. Note the distinct light "shadows" on the surface around each injector on the sides farthest from the cathode. A small light bulb placed near the tip of the cathode, which simulates the intense continuum emission region, is found to cast shadows of the injectors which exactly fill these light areas. Examination of the surface in these "shadows" reveals only slight damage as compared to other areas of the Plexiglas plate. The injectors themselves show an erosion pattern which is also consistent with radiation heating from the intense source off the cathode tip. No detailed quantitative studies of the ablation process in the MPD arc have yet been made and consequently it is not possible to assess the relative roles of heat conduction and radiation. It is interesting to recall however, that there is residual ablation even when the discharge is highly overfed, which suggests that ablation under such conditions may be due to radiative effects exclusively.

A-3 EFFECTS OF INJECTION GEOMETRY AND INSULATOR MATERIAL

It appears from the foregoing discussions that the mass injection geometry has a strong influence on the insulator erosion, and that to minimize ablation the mass flow of argon should be matched locally to the current density everywhere on the surface of the Plexiglas end plate. Recent investigations lend support to this contention.[28,81] Various injection geometries are in the process of being investigated at the present time. In one, the propellant is injected radially from each injector head, to provide a film of argon over the entire surface of the insulator; ablation

"SHADOW" AREAS

CATHODE

SEVERE ABLATION

INJECTORS
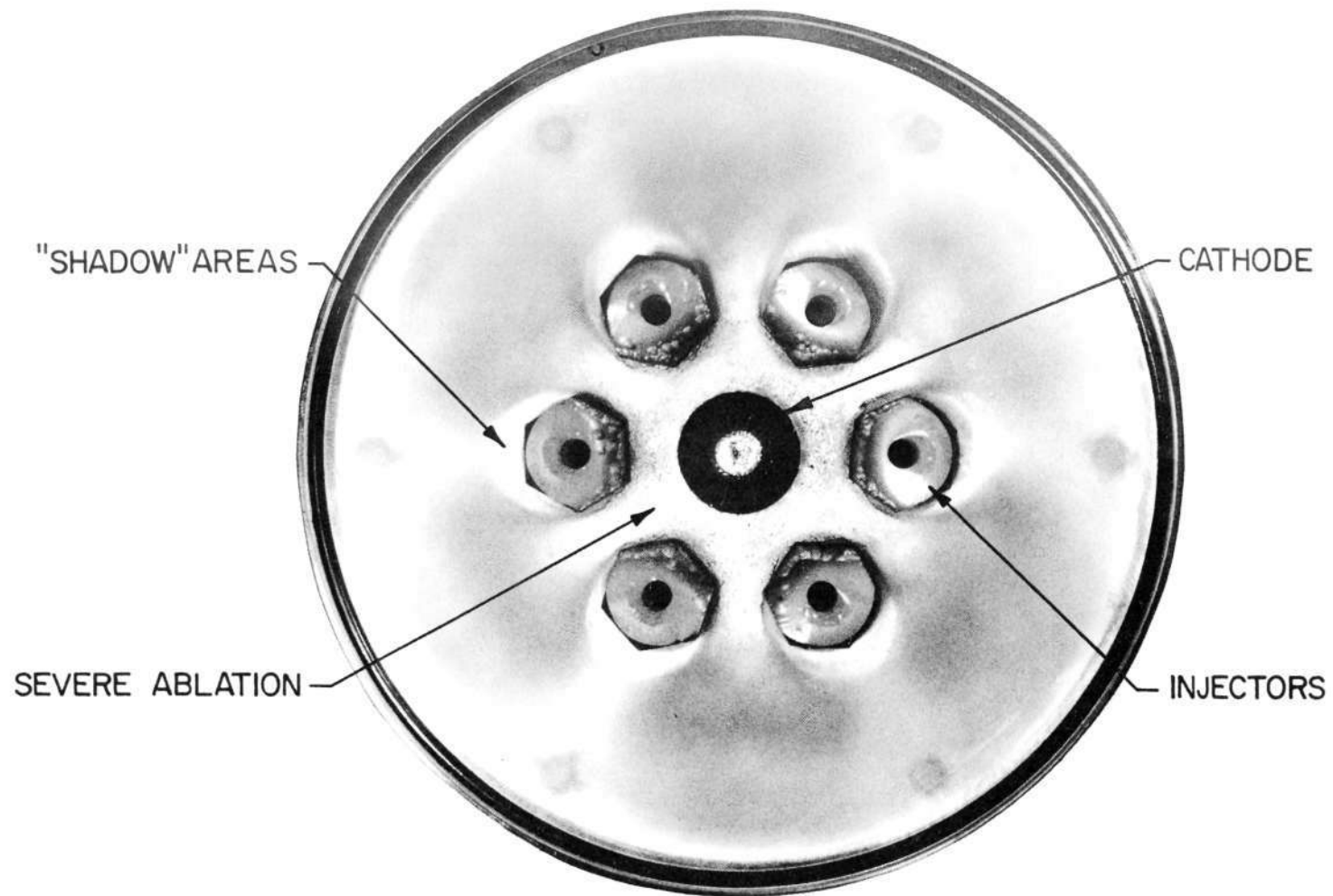
ABLATION PATTERN ON PLEXIGLAS END WALL

is noticeably reduced. Other injection geometries such as annular slits and radial injection from the base of the cathode meet with even greater success in reducing ablation.[81] A more sophisticated injection technique that may be useful is a porous end wall.

The use of other more durable insulator material is also being considered, however it does not appear that substitution of a refractory material for Plexiglas, without a change in mass injection geometry will completely alleviate the ablation problem. The thermal diffusivity and ablation temperature of a refractory such as quartz or boron nitride are much higher than of Plexiglas, which means that for a given heat flux it will take the surface of the refractory longer to reach its ablation temperature. Consider for example a semi-infinite slab of insulator at initial temperature T_i. At $t = 0$ let the surface be subjected to a flux of energy P_o W/cm^2 which thereafter remains constant in time. The surface temperature T, as a function of time t, is given by[82]

$$T - T_i = \frac{2 P_o t^{1/2}}{(\pi k \rho C_p)^{1/2}}$$

where k, ρ, and C_p are the thermal conductivity, density, and specific heat of the slab. If the ablation temperature T^* is reached at $t = t^*$ one can write

$$t^* = \frac{\pi k \rho C_p}{4 P_o^2} (T^* - T_i)^2$$

Thus the ratio of the times to ablation of two different materials is given by:

$$\frac{t_1^*}{t_2^*} = \frac{k_1 \rho_1 C_{p1}}{k_2 \rho_2 C_{p2}} \left(\frac{T_1^* - T_i}{T_2^* - T_i} \right)^2$$

where subscripts 1 and 2 identify the two different materials. Denote quartz by subscript 1 and Plexiglas by subscript 2. Then:

$k_1 = 7.96 \times 10^{-3}$ joules/sec cm$^{\circ}$C $k_2 = 1.88 \times 10^{-3}$ joules/sec cm$^{\circ}$C

$\rho_1 = 2.66$ g/cm^3 $\rho_2 = 1.2$ g/cm^3

$C_{p1} = 1.01$ joules/g $^{\circ}$C $C_{p2} = 1.47$ joules/g $^{\circ}$C

$T_1^* = 1600$ $^{\circ}$C [78] $T_2^* = 460$ $^{\circ}$C [83]

Thus $$\frac{t_1^*}{t_2^*} \approx 80$$

for $T_i = 25$ $^{\circ}$C. Kerr-cell photographs similar to those in Fig. A-1 indicate that ablation of the Plexiglas near the base of the cathode begins about 5-10 μsec into the current pulse. Thus, if quartz were used instead of Plexiglas, it would begin to ablate there sometime between 400 and 800 μsec after discharge initiation, all other conditions being equal. For the remainder of the current pulse the ablating surface area of the quartz would continue to grow, albeit more slowly than for the Plexiglas. It is not known, however, how the current density adjacent to the quartz insulator, and thus the rate of energy deposition to its surface would be affected by the lack of either argon or ablated material between the injectors during the transient heating time.

A-4 TRANSIENT EFFECTS ON SPECIES STRUCTURE

Since the species structure of the exhaust is a result of the ablation of the Plexiglas insulator, it follows that during the first 150 μsec of operation the structure will reflect the growth of the ablation rate. The Kerr-cell photographs of Fig. A-1 confirm this. At 40 μsec, just after stabilization of the current pattern, no structure is yet visible in the plume downstream of the anode or in the conical luminous region between cathode and anode. By 100 μsec, however, the familiar jet structure is clearly visible, and at 150 μsec it

exhibits its final steady configuration. The increase of ablated flow rate during this time effectively lowers the average molecular weight of the exhaust (the average molecular weight of the ablation products is about 6.6 as compared to 40 for argon), and, it is believed, leads to an increase in the average exhaust velocity. The latter can be justified on the basis of experimental results of Malliaris[34] who found that regardless of the propellant used, the kinetic energy of the exhaust of an MPD accelerator remains constant, so that the average exhaust velocity scales inversely as the square root of the average molecular weight. The increase in the average exhaust velocity should be detectable as an increase in the back emf of the arc. Terminal voltage measurements, Fig. A-5, confirm this. Figure A-5c, obtained at 16 kA and 6 g/sec shows a monotonic rise of about 32V during the first 150 μsec, after the drop from bank voltage (4KV). The other voltage signatures, obtained at different operating conditions, indicate that more pronounced voltage increases occur under starved conditions while flatter signatures result under overfed conditions. The observed transient voltage change at any condition is, however, not entirely due to the increase in back emf. Part is believed to correspond to the energy the discharge must expend in pyrolyzing and dissociating the material it ablates. For example, indications are that for the 16 kA, 6 g/sec case the rate of ablation is approximately 1 g/sec.[8] For Plexiglas the energy of surface depolymerization and gasification is about 27 kcal/mole,[83] while the energy of decomposition is 1470 kcal.[84] Thus an ablation rate of 1 g/sec requires a power expenditure of about 6×10^4 W, which at a current of 16 kA, corresponds to a voltage of approximately 4V, which is about 12% of the increase and only about 2% of the total steady state discharge voltage. Most of the voltage change during the first 150 μsec would thus appear to be a result of increased average exhaust velocity. Clearly, direct measurements of the ablation rate are necessary for a more accurate

200 μsec/DIV

	J (kA)	ṁ(g/sec)	$J^2/\dot{m}$
a) OVERFED	8	6	10
b) OVERFED	16	12	20
c) MATCHED	16	6	40
d) UNDERFED	16	3	80
e) UNDERFED	32	6	160
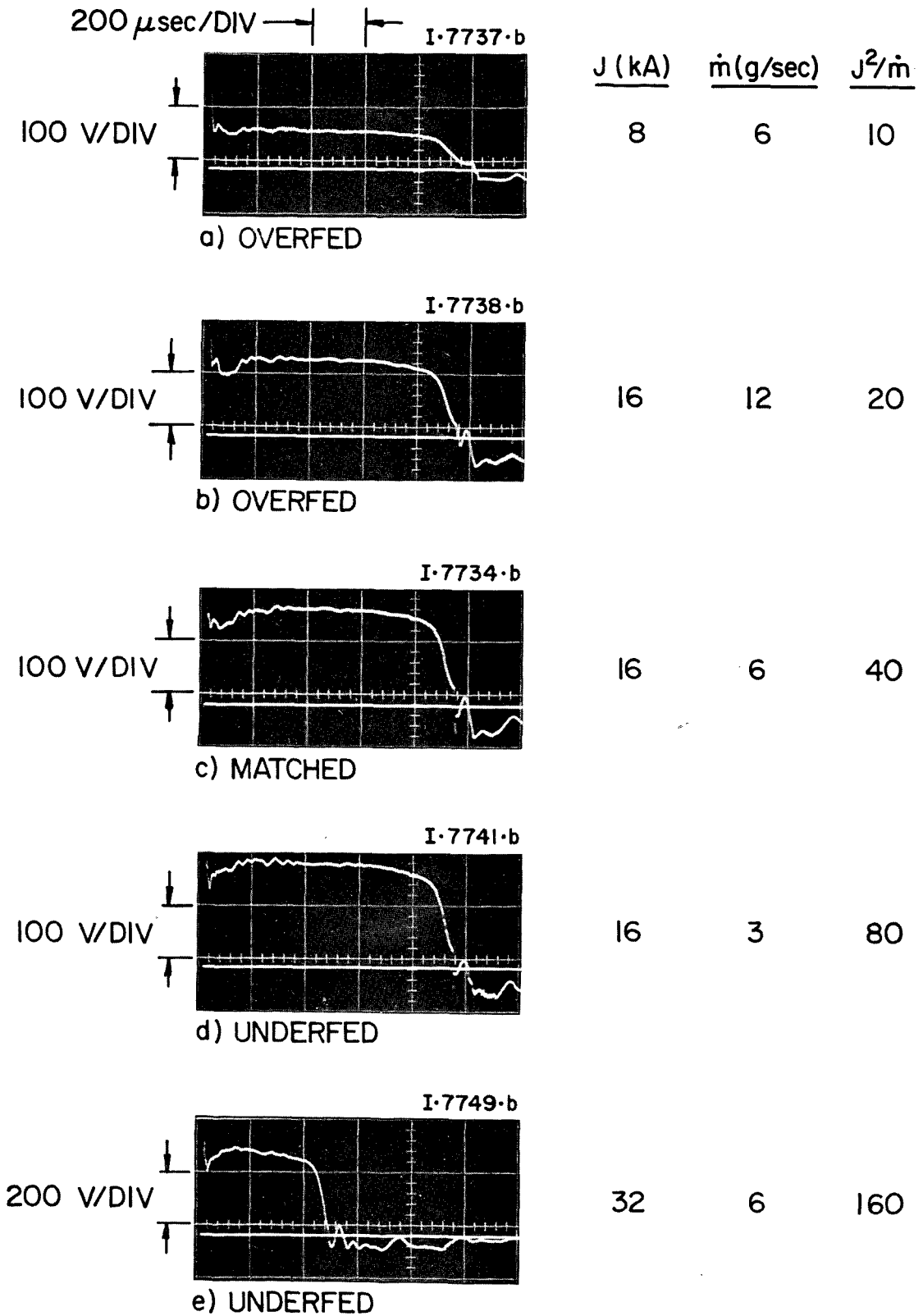
ARC VOLTAGE RECORDS AT VARIOUS
OPERATING CONDITIONS

FIGURE A-5
AP 25· P 437

assessement of the relative contributions of back emf and insulator ablation to the terminal voltage.

APPENDIX B

THEORY OF THE FABRY-PEROT INTERFEROMETER

B-1 INTRODUCTION

The Fabry-Perot interferometer, shown schematically in Fig. B-1, consists essentially of two transparent glass or quartz plates whose faces are in principle perfectly plane and parallel.[24] Each of these faces is covered by a reflecting coating of reflection coefficient R, transmission coefficient T, and coefficient of absorption $A = 1 - R - T$. If the plates are illuminated by a convergent (or divergent) beam of mono-chromatic light the multiple reflections off the inner plate surfaces give rise to a system of interference fringes at in-finity which when focused on a screen by a lens appear as a set of concentric luminous rings.

A ray of light incident on the plates at an angle Θ, gives rise through successive reflections to an infinite num-ber of parallel transmitted rays of decreasing amplitude. The path difference between any two successive transmitted rays is[24,41]

$$\delta = 2\ \mu d\ \cos\Theta$$

and thus the phase difference is:

$$\phi = 2\pi\frac{\delta}{\lambda} = 2\pi p$$

where μ is the refractive index of the gap between the plates, d is the plate separation, λ is the wavelength of the incident light, and $p = (2\mu d \cos\Theta)/\lambda$ is the order of inter-ference. If p is an integer, i.e.: the path difference between successive rays is an integral number of wavelengths, the transmitted rays interfere constructively and the incident ray is transmitted. If this condition is not exactly ful-filled the multiple rays interfere destructively, the con-structive interference of a great number of vibrations being
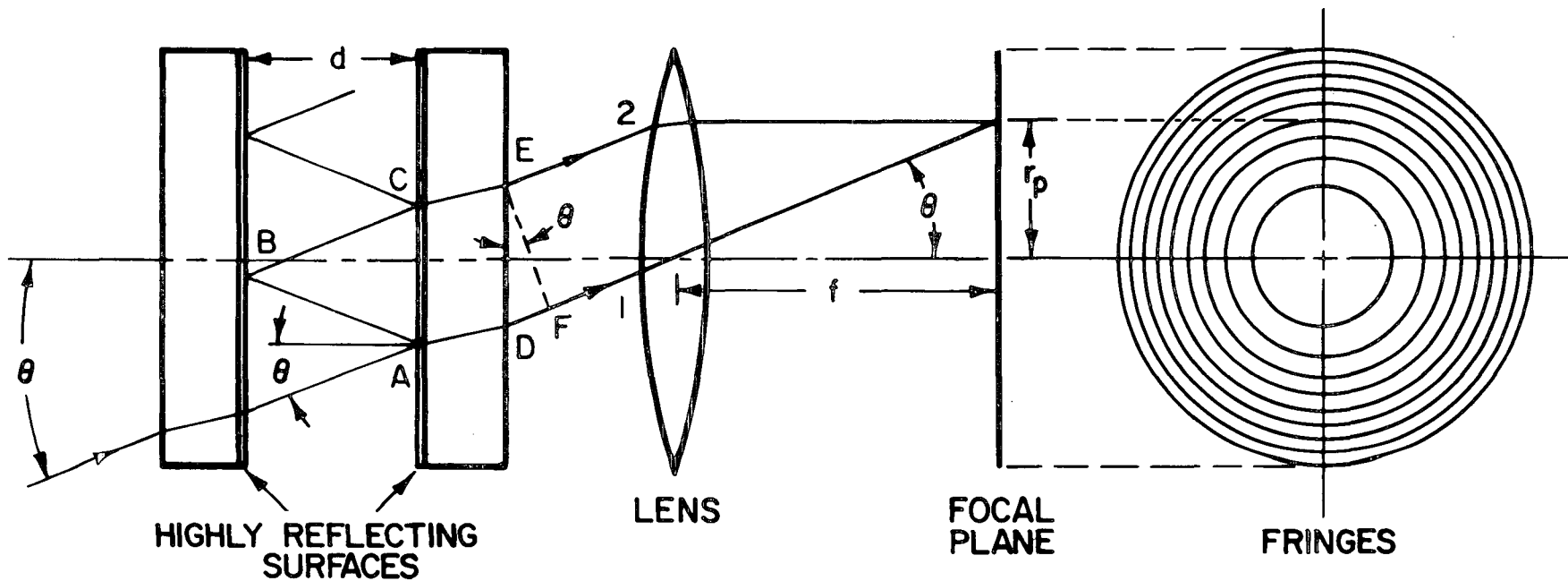
FABRY - PEROT INTERFEROMETER

very critical, and the incident energy is reflected back to the source.

If E_0 is the amplitude of the incident light the complex amplitudes of the transmitted rays are

$$E_0 T, \quad E_0 TR \, e^{-i\phi}, \quad \ldots E_0 TR^n \, e^{-in\phi} \ldots$$

which form a geometric progression with common factor $R \, e^{-i\phi}$. The sum of these amplitudes at the focal plane of the imaging lens is therefore

$$E_T = \frac{E_0 T}{1 - R e^{-i\phi}}$$

The intensity $I_T = |E_T|^2$ of the transmitted light is thus given by

$$I_T = \frac{I_0 T^2}{|1 - R e^{-i\phi}|^2}$$

$$= I_0 \frac{T^2}{(1-R)^2} \cdot \frac{1}{1 + \frac{4R}{(1-R)^2} \sin^2 \frac{\phi}{2}}$$

where $I_0 = |E_0|^2$ is the intensity of the incident beam.

The intensity thus varies with ϕ according to the periodic function:

$$A_1 = \frac{T^2}{(1-R)^2} \cdot \frac{1}{1 + \frac{4R}{(1-R)^2} \sin^2 \frac{\phi}{2}}$$

which is known as the Airy function.[24,41,42] Its general behaviour is shown in Fig. B-2, for various values of the reflectance R. If R is small the interference fringes are broad and indistinct, whereas if R is close to 1, the fringes are very sharp. This and other factors affecting fringe sharpness will be discussed in more detail in a later section.

Since ϕ is a function of incident angle θ, optical thickness μd and wavelength λ so is the function A_1. For a given μd, A_1 is a function only of θ and λ so that a

$$\phi = \frac{4\pi\mu d\cos\theta}{\lambda}$$
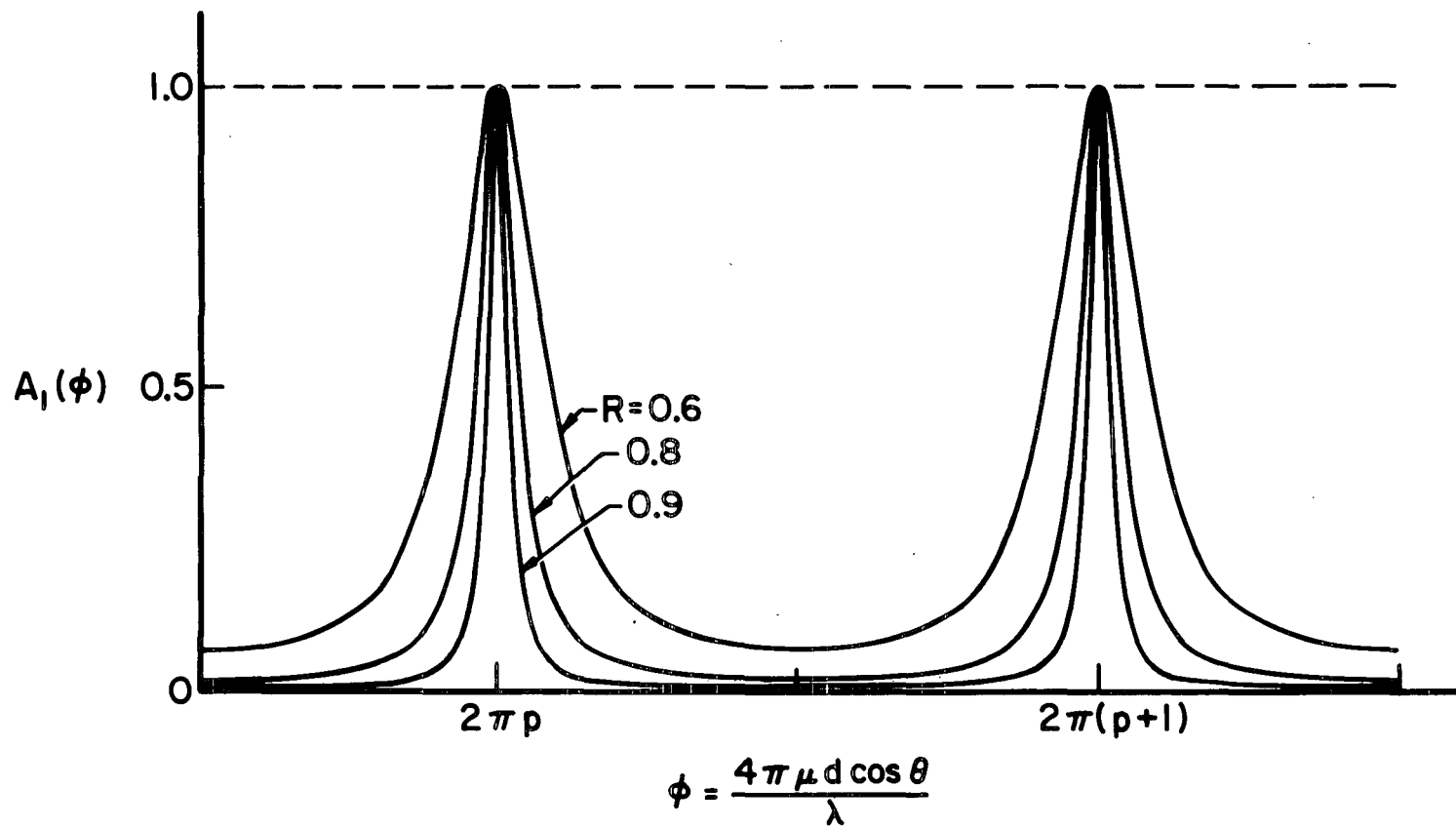
TRANSMISSION FUNCTION OF FABRY-PEROT INTERFEROMETER
(A=0, T=1-R)

monochromatic source of light gives rise to a unique system
of concentric interference fringes. When the light source is
not monochromatic the interferometer will produce a distinct
ring system for each different wavelength present. For a
given order of interference the diameter of the resulting
circular fringe will be a function of the wavelength. In ef-
fect then, the Fabry-Perot causes a spatial separation or dis-
persion of wavelengths.

B-2   DETECTION METHODS

Clearly, the simplest method of recording the interfer-
ence fringes is to place a photographic plate at the focal
plane of the fringe imaging lens. This method is generally
used with interferometers of fixed plate separation, better
known as etalons. A more versatile detection system which
lends itself readily to time-resolved spectroscopy, is one
which uses photoelectric detection, with the interferometer
operating in the so-called scanning mode.[42,44,45]   In
this technique the photographic plate is replaced by a dia-
phragm which isolates a region of points which receive rays
of the same wavelength. In principle this diaphragm should
be an annular slit, however a pinhole located at the center
of the fringe system is generally employed. The pinhole can
be considered as an annulus of zero inner radius. The inter-
ferometer and diaphragm together act as a filter or mono-
chromator. To make a spectrometer a photoelectric detector,
coupled to a recorder, is placed behind the isolating dia-
phragm, as shown in Fig. B-3. The transmitted wavelength
at the pinhole is varied continuously by varying the optical
thickness μd of the interferometer. One way of doing this
is to vary the plate separation d by means of a piezoelec-
tric transducer applied to one of the plates.[44,45]
If d is made to decrease, the fringe system contracts, each
fringe decreasing in radius until it disappears at the center.
If several discrete wavelengths are present their separate
ring systems are thus swept by the pinhole successively, so
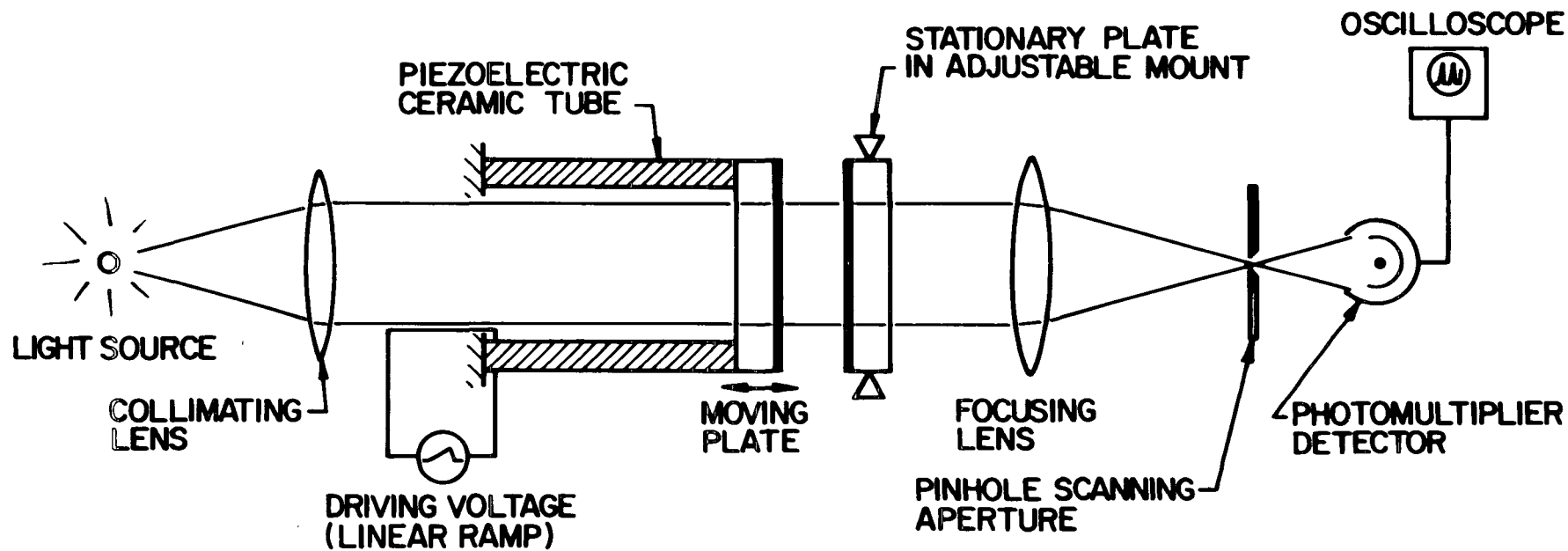
SCHEMATIC OF SCANNING FABRY-PEROT SPECTROMETER

OSCILLOSCOPE

STATIONARY PLATE
IN ADJUSTABLE MOUNT

PIEZOELECTRIC
CERAMIC TUBE

LIGHT SOURCE

COLLIMATING
LENS

DRIVING VOLTAGE
(LINEAR RAMP)

MOVING
PLATE

FOCUSING
LENS

PINHOLE SCANNING
APERTURE

PHOTOMULTIPLIER
DETECTOR

FIGURE B-3
AP 25·4853

134

that in effect the spectrum is scanned.

At the pinhole, which selects collimated light normal to the plates, the wavelength of maximum transmission is a linear function of the plate separation. However, for any given wavelength the device has an infinite number of transmission modes such that for each amount $\lambda/2$ that the plate separation changes, the given wavelength will again be transmitted (Fig. B-4) so that the transmitted intensity function as recorded by the detector will consist of an infinite number of equally spaced fringes, i.e: the Airy function.

Conversely, if the wavelength λ at which transmission occurs is changed at fixed plate spacing, the instrument will transmit again when λ has changed an amount $\Delta\lambda_f = \lambda^2/2\mu d$. [24,41] This is equivalent to the ring system changing size as λ changes until the p'th ring at wavelength $\lambda + \Delta\lambda_f$ overlaps the (p + 1)th ring of wavelength λ. This wavelength change is called the free spectral range. Any two wavelengths separated by an integral multiple of $\Delta\lambda_f$ will be transmitted at the same plate separation. (Fig. B-4) Consequently the wavelength range that may be examined unambiguously with the Fabry-Perot interferometer is limited to $\Delta\lambda_f$. (In terms of wavenumber $\sigma = 1/\lambda$, the free spectral range is given simply by $\Delta\sigma_f = 1/2\mu d$).

B-3 FACTORS INFLUENCING THE FABRY-PEROT SPECTROMETER

By definition, the instrumental function of a spectrometer is the curve which would be recorded if the instrument were illuminated by a perfectly monochromatic source. An infinitely thin spectral line is always rendered as one with finite width by any real spectrometer. The overall instrumental broadening function is a convolution of the various individual broadening functions present in the device. [42]

In a scanning Fabry-Perot spectrometer there are three distinct contributions to line broadening. In the first place, even if the instrument is otherwise perfect the interference
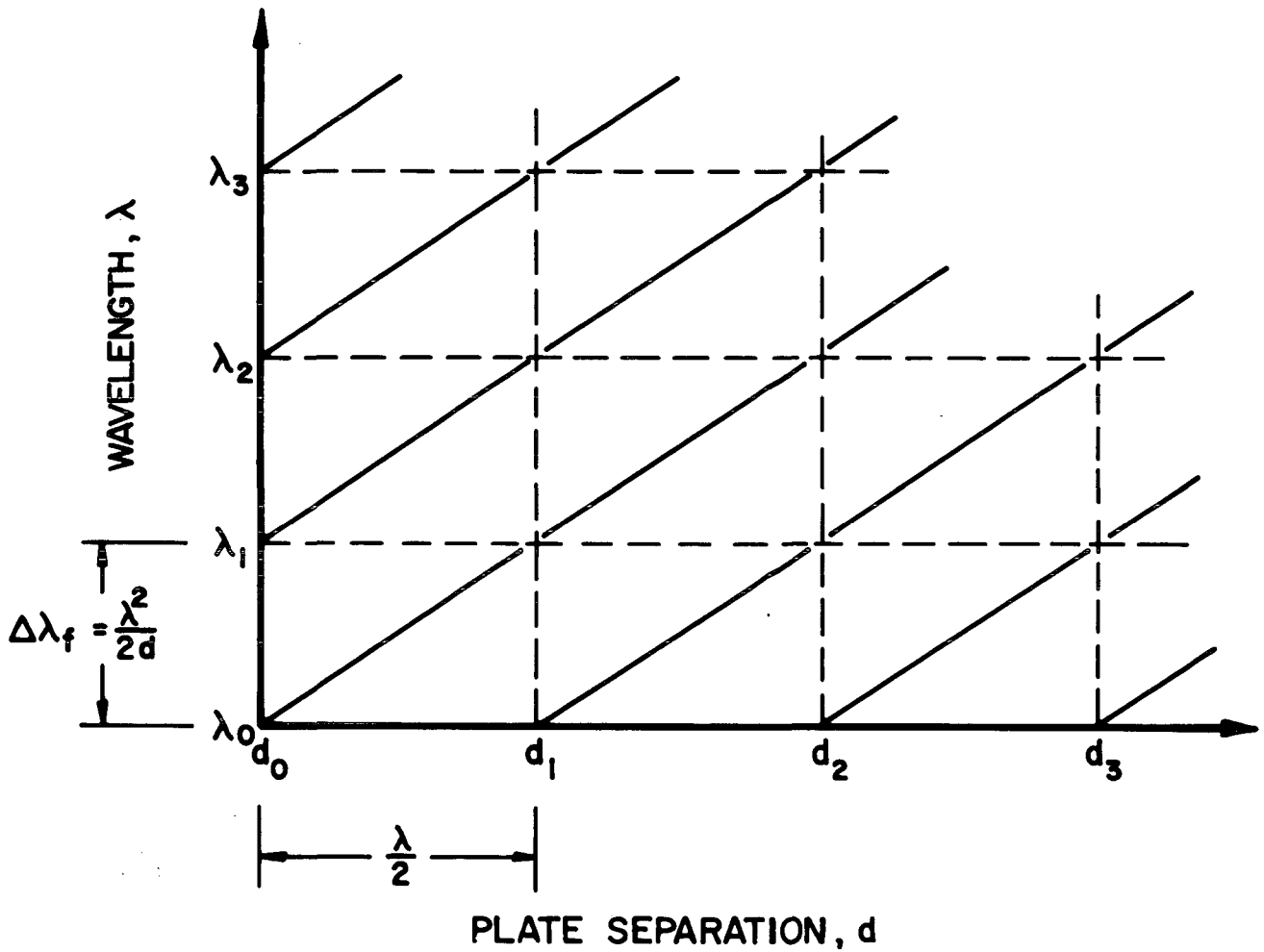
TRANSMITTED WAVELENGTH AS A FUNCTION
OF FABRY-PEROT PLATE SEPARATION

fringes will have a limiting finesse, that is, a finite width. The finesse is defined as the ratio of fringe separation to the width at half intensity of a fringe. This theoretical finesse depends only on the reflectivity R of the plates and is called the reflectivity finesse, F_R. In reality the effective finesse of the fringes is also limited by the unavoidable imperfections on the plate surfaces which cause the plate separation to not be strictly constant across the diameter of the plates. Furthermore, the necessarily finite size of the pinhole also causes a decrease of the finesse. The three effects just described can be characterized by three partial instrumental functions, A_1, A_2 and A_3, in that order. The resulting total instrumental function is a convolution of these three partial functions: $A_T = A_1 * A_2 * A_3$.

Effect of Plate Reflectivity

A Fabry-Perot interferometer with perfectly flat plates, illuminated by monochromatic radiation of wavenumber σ has a transmission function

$$A_1 = \frac{\tau_M}{1 + \frac{4R}{(1-R)^2} \sin^2 \pi \sigma \delta}$$

$$\text{where } \tau_M = \frac{T^2}{(1-R)^2}$$

as was shown previously. If the pinhole scanning aperture is infinitely small, the scan of the interferometer will register the above function. The ideal instrumental function A_1 is thus the Airy function, as shown in Fig. B-5, where it is plotted against wavenumber, σ. It consists of a series of maxima whose width at half height is $\Delta\sigma_1$, and which are separated by the interval $\Delta\sigma_f$. The latter is the free spectral range which in terms of the wavenumber is $1/2\mu d$. The half-width of the Airy fringes for values of R not less than about 0.8 is well approximated by[24,41,42]

$$\Delta\sigma_1 = \frac{1-R}{\pi\sqrt{R}} \Delta\sigma_f$$

FREE SPECTRAL RANGE
$\Delta\sigma_f$

$\tau_M = \dfrac{T^2}{(1-R)^2}$

$A_I(\sigma)$ $0.5\tau_M$

$\Delta\sigma_I = \dfrac{\Delta\sigma_f}{F_R}$

0

σ_p

σ_{p+1}

WAVENUMBER, σ
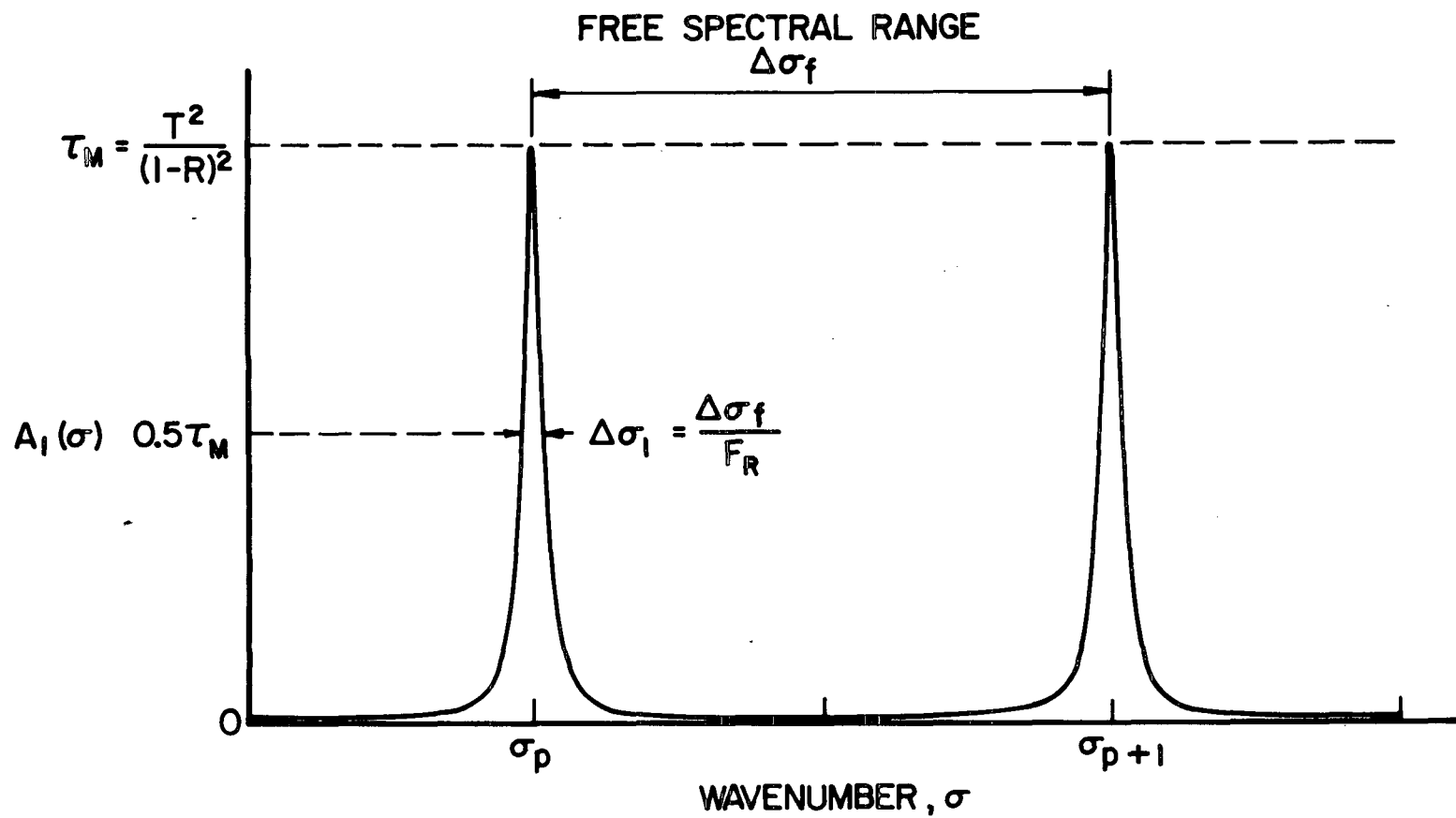
IDEAL INSTRUMENTAL FUNCTION, $A_I(\sigma)$

The ratio $\frac{\Delta\sigma_\ell}{\Delta\sigma_i} = \frac{\pi\sqrt{R}}{1-R} = F_R$ is the reflectivity limited finesse of an otherwise ideal instrument. It increases rapidly as R approaches 1. With plates of very high reflectivity a finesse of several hundred can in principle be attained. The maximum transmission factor is theoretically independent of R if the absorption coefficient A of the reflecting coatings is negligible:

i.e: $$\tau_M = \frac{T^2}{(1-R)^2} = 1 \qquad \text{if } A = 1 - T - R = 0$$

However, if $A \neq 0$, τ_M will decrease rapidly as R approaches 1. (Fig. B-6) It is desirable thus to use reflective coatings with as low an absorption coefficient as possible. Typical values obtained in practice with multilayer dielectric films lie in the range 0.05 - 0.2%.

It would seem, on the basis of the preceding arguments, that as high a reflectivity as possible should be used to maximize the instrumental finesse and thus its resolving power. However, the true finesse is always limited by departures from perfect surface flatness of the plates, and the reflectivity finesse F_R should not be greater than a certain value, which is determined by the quality of the plates.[43]

Influence of Surface Flatness

To evaluate the reflectivity limited instrumental function $A_1(\sigma)$ the interferometer plates were assumed to be perfectly plane and parallel, so that the plate separation was everywhere exactly equal to d. In actual fact however, it is impossible to manufacture plate surfaces which are flat enough that surface defects may be neglected. This is easily verified experimentally by illuminating the interferometer with a normal collimated monochromatic beam of light and adjusting the plate separation for maximum transmission. On a screen placed immediately behind the interferometer a uniform circle of light, with a diameter equal to that of the incoming beam or of the
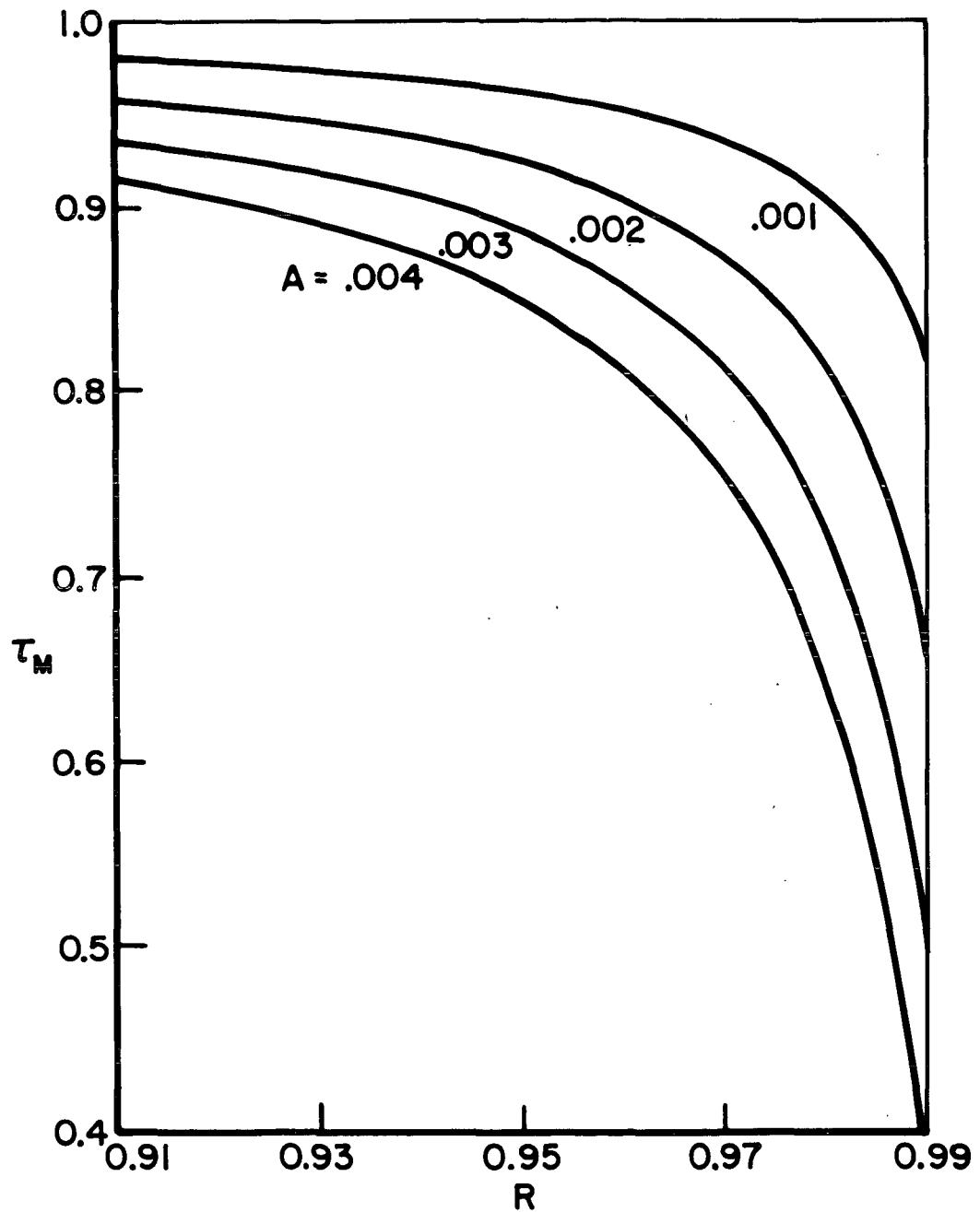
EFFECT OF FINITE ABSORPTION
ON FABRY-PEROT TRANSMISSION

FIGURE B - 6

clear plate aperture, whichever is smaller, should be seen
if the plate separation is constant everywhere. However, in
reality the circle of light will not be uniformly illuminated
but will consist, in general, of irregular regions of light
and darkness such as shown in Fig. B-7, which is observed with
the Fabry-Perot interferometer used in the experiments de-
scribed in Chapter 4. This proves that only over certain
areas of the plates is the separation exactly that required
to transmit the monochromatic beam of given wavelength. If
the wavelength is varied, or if the average plate separation
is changed, the luminous zones will change shape. These
variations characterize the surface flatness defects of the
interferometer plates.

The problem is usually analyzed by considering an imper-
fect interferometer to consist of a juxtaposition of small
interferometers of different plate separation, where the total
transmitted light flux is the sum of the individual fluxes
transmitted by the elementary interferometers. The exact
instrumental function $A_2(\sigma)$ for various plate defects can
be obtained analytically.[43] For example, if the
plates have a spherical surface the function is rectangular,
if the plates suffer random micro-defects the function is
Gaussian, and if one plate is tilted relative to the other
the function is parabolic. In actual fact the plate sur-
faces,and thus the plate separation,suffer from a combination
of such defects. It can be shown, however, that regardless of
the actual forms of the various defects, the instrumental func-
tion has a width that is related to the mean deviation from
flatness.[43] The flatness limited finesse is a simple func-
tion of this deviation and is given by:

$$F_D = \frac{1}{2\sigma\Delta\varepsilon} = \frac{\lambda}{2\Delta\varepsilon}$$

where $\Delta\varepsilon$ represents the mean deviation from flatness. For
example, if the plates are flat to $\lambda/100$, the flatness
limited finesse $F_D = 50$.

FABRY - PEROT PLATE

38 mm

TRANSMITTING AREA
FLAT TO $\approx \lambda/90$
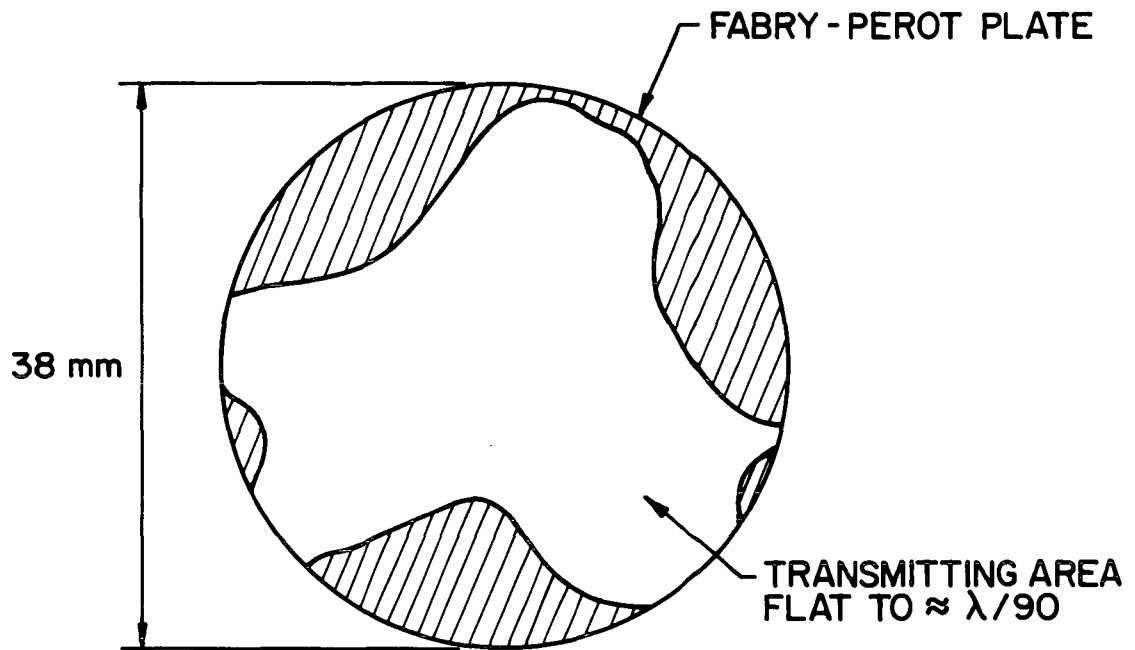
SURFACE FLATNESS OF INTERFEROMETER PLATES

FIGURE B-7
AP25·4857

Effect of Finite Pinhole Size

The apparatus function $A_3(\sigma)$ characterizing the influence of a pinhole of finite size is obviously of rectangular form. This can be understood by considering the pinhole in its more general form of an annulus, and assuming the fringes projected on the focal plane to be negligibly thin compared to the annular aperture. During a scan of the interferometer the flux transmitted by the aperture remains at a constant value as long as an interference fringe is moving within the annular slit, but goes to zero abruptly as soon as the fringe moves out of the annulus. The width $\Delta\sigma_3$ of the rectangular function $A_3(\sigma)$ can be easily related to the angular size of the pinhole: [42]

$$\Delta\sigma_3 = \frac{\alpha^2\sigma}{2}$$

where α is the angle subtended by the radius of the pinhole at the imaging lens, i.e: $\alpha = \frac{P}{2f}$, where P is the pinhole diameter and f is the focal length of the lens. The pinhole finesse is consequently

$$F_P = \frac{\Delta\sigma_f}{\Delta\sigma_3} = \frac{1}{\mu d\alpha^2\sigma}$$

Overall Instrument Function

The overall instrument function is the convolution of the three individual functions described above: [42]

$$A_T = A_1 * A_2 * A_3$$

This function is similar to A_1, to the extent that it consists of a series of equidistant maxima with half-width $\Delta\sigma_T$ and which are separated by the free spectral range $\Delta\sigma_f$ (Fig. B-8). The two important characteristics of $A_T(\sigma)$ are the ordinate $\mathcal{T}_T$ of the maxima and their width at half height, $\Delta\sigma_T$. The luminosity of the spectrometer is proportional to $\mathcal{T}_T$, while its effective resolution $\mathcal{R}$ varies inversely as $\Delta\sigma_T$, i.e.: $\mathcal{R} = \frac{\sigma}{\Delta\sigma_T}$. This resolution can in principle be increased without limit. That is, the width of each of the functions $A_1(\sigma)$ $A_2(\sigma)$ $A_3(\sigma)$ can be made as small as desired. This is

FIGURE B-8
AP25·4858

154
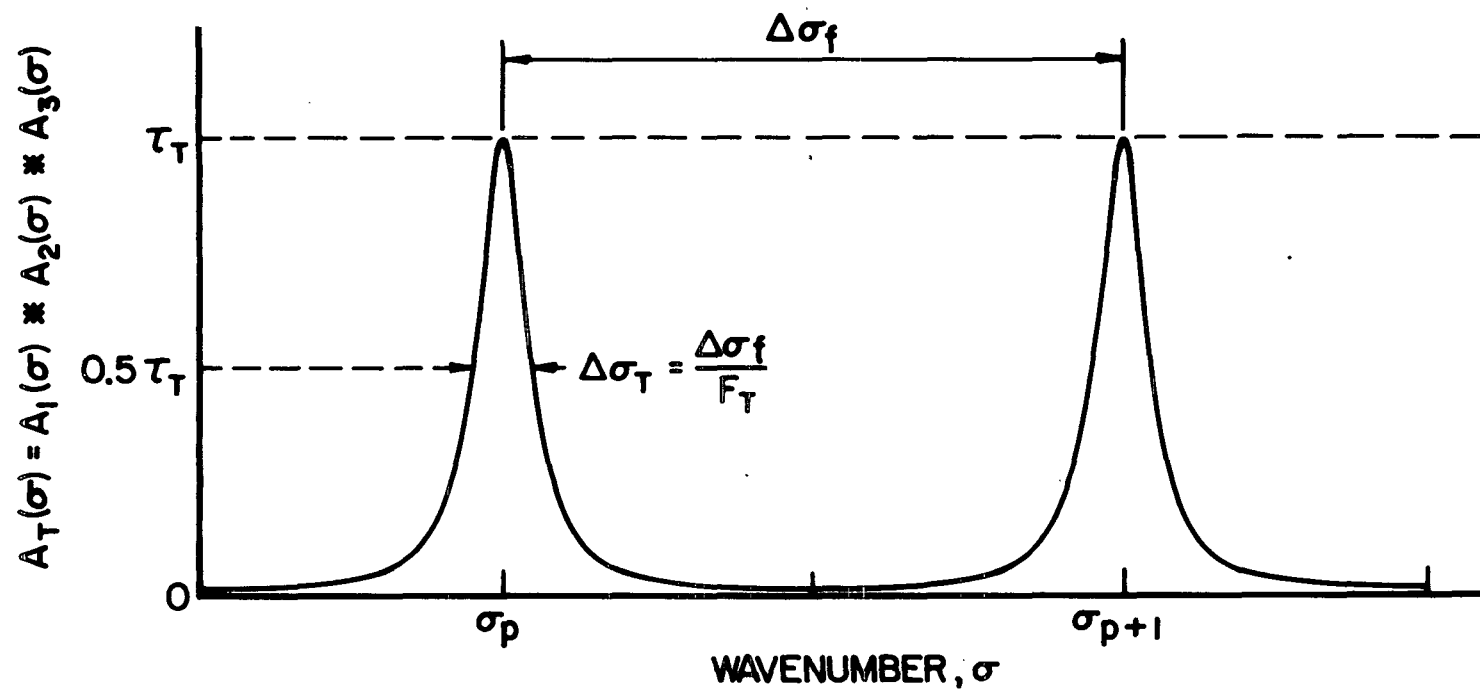
OVERALL INSTRUMENTAL FUNCTION, $A_T(\sigma)$

evident for A_3 which approaches zero width as the pinhole
diameter approaches zero. It is also true for A_1 and A_2,
because $\Delta\sigma_1 = \Delta\sigma_f/F_R$ and $\Delta\sigma_2 = \Delta\sigma_f/F_D$. Since the
free spectral range $\Delta\sigma_f = 1/2\mu d$. it is sufficient to in-
crease the plate separation d to decrease $\Delta\sigma_f$ and hence
$\Delta\sigma_1$ and $\Delta\sigma_2$ and consequently $\Delta\sigma_T$. In principle then, the
effective resolution $\mathfrak{R} = \sigma/\Delta\sigma_T$ can be easily increased
without limit. This is one of the primary advantages of the
Fabry-Perot interferometer.

A knowledge of the exact total instrumental function
$A_T(\sigma)$ requires knowledge of the three component functions
A_1, A_2, A_3. It is impossible to precisely determine the
function A_2 due to plate surface imperfections, nevertheless
its width $\Delta\sigma_2$ can be determined exactly. Fortunately, the
values of $\mathcal{L}_T$ and $\Delta\sigma_T$ depend much less on the exact form of [43]
$A_2(\sigma)$ than on its half-width $\Delta\sigma_2$. It is known that the
breadth of the resulting function $A_T(\sigma)$ is always greater
than the largest of the widths $\Delta\sigma_1$, $\Delta\sigma_2$, $\Delta\sigma_3$ of the com-
ponent functions, but less than their sum. To a first ap-
proximation one can write: [42]

$$\Delta\sigma_T^2 \approx \Delta\sigma_1^2 + \Delta\sigma_2^2 + \Delta\sigma_3^2$$

What remains to be done now is to choose the characteris-
tics of the interferometer in such a way as to maximize both
the resolution and luminosity.

Importance of Plate Flatness

Since the breadth $\Delta\sigma_T$ of the total instrument function
is always greater than the largest of $\Delta\sigma_1$, $\Delta\sigma_2$ and $\Delta\sigma_3$
it remains to determine which of the latter is the most im-
portant. It is evident that $\Delta\sigma_3$ can be chosen as small as
desired by decreasing the size of the pinhole sufficiently.
Furthermore, modern reflecting coatings made of multi-layer
dielectric films can be made to attain reflectivities very
close to unity without appreciable absorptivity (e.g. $R \approx 99.8\%$,
$A \approx 0.05\%$ in the red end of the spectrum). The reflectivity

finesse F_R thus can be made as large as desired, at least in the visible part of the spectrum, achieving values of the order of several hundred. On the other hand, it is virtually impossible to manufacture plates with defects smaller than $\lambda/200$.[46] Furthermore, the subsequent deposition of dielectric coatings cannot be made without degrading this figure to about $\lambda/100$.[46] As a result the flatness limited finesse cannot exceed a value of about 50 and consequently it is the function A_2 due to surface defects which is the broadest. (It should be noted at this point that in an instrument which is scanned very rapidly the moving plate may bow or vibrate, due to the acceleration at the beginning of the scan, to an extent which can markedly decrease its flatness figure, thus decreasing the limiting finesse F_D even further.[44])

Using the concept of finesse one can define for the spectrometer system an effective total finesse, defined by $F_T = \Delta\sigma_f/\Delta\sigma_T$ where $\Delta\sigma_f$ is the free spectral range and $\Delta\sigma_T$ the half-width of the function $A_T(\sigma)$. It follows, then, that the total finesse F_T is always less than the finesse F_D due to surface defects. It is obvious that the latter has the role of a limiting finesse which can only be approached.

Choice of Plate Reflectivity and Pinhole Size

It remains to choose the widths $\Delta\sigma_1$ and $\Delta\sigma_3$, that is the reflectivity finesse, F_R, and the pinhole finesse F_P in such a way as to optimize the function $A_T(\sigma)$ with respect to transmission, τ, and half-width $\Delta\sigma_T$ compatible with the limiting flatness finesse F_D.

Consider the partial function $A_{12} = A_1 * A_2$ which is the function of a real interferometer, accounting for plate flatness limitations, but neglecting for the moment the pinhole effects. Its form is analogous to those of A_1 and A_T (Fig. B-5 and B-8). The width $\Delta\sigma_{12}$ of its maxima can be characterized by a finesse $F_e = \Delta\sigma_f/\Delta\sigma_{12}$ which is simply the effective finesse of the interference fringes themselves. The ordinate

τ_e of the maxima of A_{12} represents the maximum transparency of the interferometer alone (i.e. minus the pinhole). It can be shown that $\Delta\sigma_{12}$ (or F_e) and τ_e are functions of $\Delta\sigma_1$, of the Airy function, i.e. are functions of the reflectivity finesse F_R. These functions are shown in Fig. B-9, plotted against the ratio of the reflectivity finesse to the flatness limited finesse, F_R/F_D.[(43)] The actual shape of these curves depends on the exact shape of the flatness function $A_2(\sigma)$; the curves of Fig. B-9 are average curves which do not deviate significantly from those obtained from specific functions A_2. The curves represent the behaviour of the ratio of effective finesse to flatness limited finesse, F_e/F_D, and the ratio of the maximum effective transmission τ_e to the maximum transmission $\tau_M = T^2/(1-R)^2$ of a perfect interferometer. It can be seen that as F_R/F_D increases from zero the ratio F_e/F_D increases rapidly at first, attaining a value of about 0.7 at $F_R/F_D = 1$. From there on the shape of the curve decreases rapidly and F_e/F_D approaches 1 asymptotically _for large values of the ratio_ F_R/F_D.

The maximum transmission τ_e of the real instrument, on the other hand, decreases monotonically as the reflectivity finesse increases. Equal to unity at $F_R/F_D = 0$, i.e. for the case of a perfect interferometer with $\Delta\sigma_2 = 0, (F_D \to \infty)$, the ratio τ_e/τ_M is less than unity for all non-zero values of F_R/F_D (i.e. of $\Delta\sigma_2$). This means that the transmission factor of a real interferometer is always less than that of one with perfect plates. This is so because due to surface defects only part of the plate area transmits light, as was discussed previously. It is evident from Fig. B-9 that there is nothing to be gained in using a reflectivity finesse F_R much greater than F_D because the effective finesse does not increase that much while the transmission factor decreases rapidly. Thus a ratio of F_R/F_D much greater than unity will lead to a large loss of luminosity without appreciably improving the resolution. The optimum value of F_R is then one close to the value of F_D.[(43)]
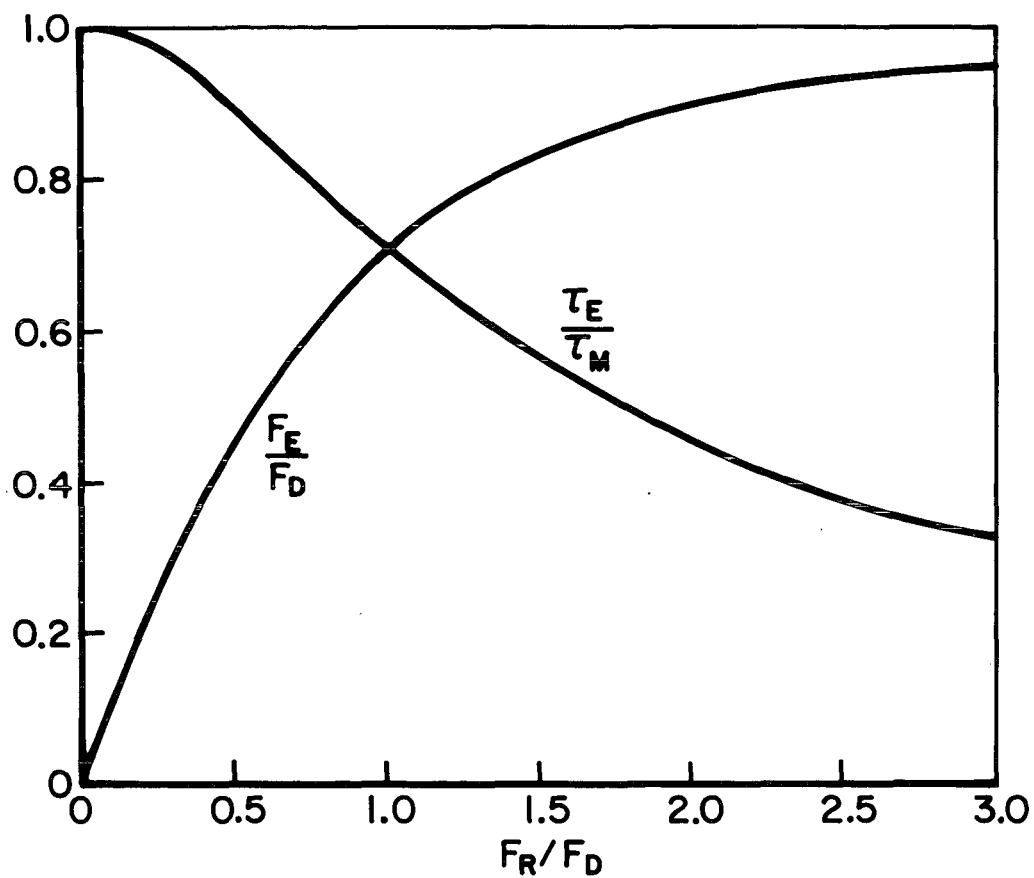
EFFECTIVE FINESSE AND TRANSMISSION FACTOR
AS FUNCTIONS OF FLATNESS FINESSE F_D

FIGURE B-9
AP 25·4859

A similar argument on the effects of pinhole size leads to much the same conclusions, i.e. the pinhole finesse should also be of the same magnitude as F_D. Thus the angular size of the pinhole radius should be:[42]

$$\alpha = \left(\frac{1}{\mu d F_D \sigma}\right)^{1/2}$$

Summarizing then, to obtain the largest possible luminosity for given resolution, the magnitudes of the individual finesses F_R, F_D, and F_P should be chosen of equal magnitude. Since the quality of the plate surfaces defines F_D, the choice of F_R and F_P is fixed. Thus the overall instrumental finesse is given by $F_T \approx 0.6\, F_D$ and the effective resolution is given by $\mathcal{R} \approx 0.6 \mathcal{R}_0$ where $\mathcal{R}_0$ is the resolution obtained if the functions A_1 and A_3 have zero width while the function A_2 has width $\Delta \sigma_2$. Finally, the maximum value τ_T of the function $A_T(\sigma)$, which determines the luminosity of the instrument, is given approximately by $\tau_T \approx 0.6 \tau_M$ where $\tau_M = T^2/(1-R)^2$ is the maximum of the Airy function A_1 of a perfect interferometer.

Luminosity of the Fabry-Perot

The luminosity $\mathcal{L}$ of the scanning Fabry-Perot interferometer is defined as the ratio of the luminous flux Φ transmitted by the pinhole to the luminance L of the light source:[42]

$$\mathcal{L} = \frac{\Phi}{L}$$

The luminous flux is given by:

$$\Phi = L \tau_T S \Omega$$

where τ_T is the total instrumental transmission factor, S is the useful area of the Fabry-Perot plates and Ω is the solid angle subtended by the pinhole at the focusing lens. For an

optimized interferometer system:

$$\tau_T \approx 0.6 \frac{T^2}{(1-R)^2}$$

$$\Omega \approx \pi \alpha^2 = \frac{2\pi}{\mathcal{R}_0}$$

whence:

$$\mathcal{L} = \tau_T S\Omega \approx 3.6 \frac{T^2}{(1-R)^2} \frac{S}{\mathcal{R}_0}$$

In terms of the effective resolution $\mathcal{R} \approx 0.6\,\mathcal{R}_0$:

$$\mathcal{L} \approx 2.2 \frac{T^2}{(1-R)^2} \frac{S}{\mathcal{R}}$$

With dielectric film reflective coatings $\frac{T^2}{(1-R)^2}$ usually lies in the range between 0.5 and 0.9 in the visible part of the spectrum. Assuming an average value of 0.7 leads to

$$\mathcal{L} \approx 1.5 \frac{S}{\mathcal{R}}$$

This result demonstrates that the luminosity of the Fabry-Perot spectrometer varies inversely with its resolution, as in any other spectrometer, and is directly proportional to the useful surface area of the interferometer plates. In practice it is the loss of luminosity which prevents increasing the resolution of the instrument without limit. For a given resolution, however, a Fabry-Perot spectrometer has a luminosity typically two orders of magnitude higher than that of a grating or prism spectrometer,[42] wherein lies its fundamental advantage.

APPENDIX C

RECOMBINATION OF AIII TO AII

C-1 INTRODUCTION

Under the conditions of temperature and particle num-
ber density found within the environment of the MPD exhaust
plume (i.e: $T_e < 2$ eV, $n_e \sim 10^{15}$ cm^{-3}) the dominant mechanism
for the recombination of AIII to AII is that of three-body
electron-electron-ion collisions, rather than two-body radi-
ative electron capture.[67,69] In a three-body recombination
event two electrons collide in the vicinity of an ion in such
a manner that one of the electrons loses sufficient kinetic
energy to be captured by one of the upper states of the ion.
Once bound in one of these upper levels, which are in thermal
equilibrium with the free electrons, the electron "diffuses"
downward toward the ground ionic or atomic state. Between
the upper states the probability is large that downward
transitions will occur via superelastic collisions with free
electrons. However, below a certain energy level (whose
identity depends largely on the free electron density and
temperature) the probability for radiative decay begins to
dominate. When the captured electron has reached the ground
state the recombination is considered completed.

The relevant chemical equation for the recombination of
AIII to AII is

$$A^{++} + e + e \longrightarrow A^{+} + e + E_R$$

where E_R is the energy released by the recombination and is
simply equal the second ionization energy of argon in this
case. Some fraction of E_R is transferred to the free elec-
trons via superelastic electron-ion collisions and the rest
is lost as radiation. The relative magnitudes of the two
effects depends largely on whether or not the plasma is
optically thin to the emitted radiation.[59-63, 68-71] It

is not within the scope of this investigation to discuss in detail the theoretical foundations of electronic recombination, and the interested reader is referred to the extensive literature on the subject.[57-69] The treatment of even one-dimensional recombining flows with only one ionic specie present is a matter of considerable complexity,[69-72] as it involves not only the usual fluid dynamic equations of mass, momentum and energy conservation but also species conservation equations, the recombination equation, an electron energy equation and considerations of radiative effects. Rather than attempt a full analytical treatment of the problem, a semi-empirical approach based on the available experimental data will be used to calculate the fraction of recombination of AIII to AII within the acceleration region, and estimate whether the energy released is sufficient to account for the flow acceleration.

C-2 THE RECOMBINATION EQUATIONS

The rate equation which determines the population n_{ii} of second ions is[69]

$$\frac{dn_{ii}}{dt} = -b\, n_{ii}\, n_e + \alpha\, n_i\, n_e$$

where $b\, n_{ii}\, n_e$ represents the number of recombination events per unit volume per unit time, and $\alpha\, n_i n_e$ the number of ionization events per unit volume per unit time. n_i, n_{ii}, and n_e are the number densities of first and second ions and electrons respectively. α is the ionization coefficient, which near equilibrium can be calculated from the Saha relation.[69] The quantity b is the recombination coefficient and is given by[65,69]

$$b = 8.75 \times 10^{-27} Z^3\, \frac{n_e}{T_e^{9/2}} \quad cm^3/sec$$

where Z is the ionic charge, and T_e is the electron temperature in eV.

At the temperatures present in the exhaust plume downstream of $x = 5$ cm (<u>i.e.</u> $T_e \leqslant 1.7$ eV) small changes in T_e can drastically affect the value of α, the ionization coefficient, because of its exponential dependence on temperature: $\alpha \sim e^{-E_i/kT_e}$, where E_i is the ionization energy.[69] For example, a decrease in T_e from 1.7 eV to 1.5 eV for $E_i = 27.6$ eV decreases α by nearly an order of magnitude. Thus, as the flow proceeds downstream of $x = 5$ cm the ionization rate of AII to AIII quickly becomes very small due to the decrease in T_e, and the ionization term in the rate equation can be dropped. The recombination term will also decrease with increasing x because of its dependence on the particle densities which decrease in the downstream direction; however, the recombination coefficient, b, is temperature sensitive ($b \sim T_e^{-9/2}$) so that the decrease in recombination rate due to the drop in density of the expanding plasma is compensated to an appreciable degree by an increase in the recombination rate coefficient due to cooling.

The rate equation with the ionization term dropped simplifies to:

$$\frac{d n_{ii}}{dt} = - b\, n_{ii}\, n_e$$

$$= -\beta\, \frac{n_{ii}\, n_e^2}{T_e^{9/2}}$$

where $B = 8.75 \times 10^{-27} \, z^3$ cm^6 eV$^{9/2}$ sec^{-1}. Since each recombination event results in the disappearance of one electron for each doubly ionized atom recombined, the rate of change of electron population is equal to the rate of change of second ion population, <u>i.e</u>: $\dfrac{d n_e}{dt} = \dfrac{d n_{ii}}{dt}$

Therefore,

$$\frac{d n_e}{dt} = - \beta\, \frac{n_{ii}\, n_e^2}{T_e^{9/2}}$$

In addition to this rate equation, the electron conservation and the global mass conservation equation are needed to take into account the flow expansion. Equations of momentum and energy conservation need not be considered because the axial temperature, velocity and density profiles along the argon jets are known from the experimental measurements.

Electron Conservation:

Consider one-dimensional flow through the control volume shown below, in which there is a source (or sink) of electrons:
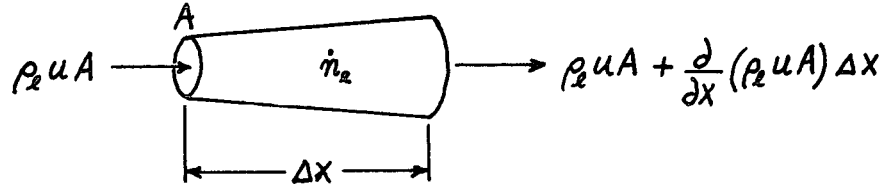
If electrons are created (or destroyed) at a rate $\dot{n}_e$, then the rate of electron mass addition (or depletion) within the volume is $m_e \dot{n}_e A \Delta x = \dot{\rho}_e A \Delta x$, where m_e is the electron mass, A the flow area, and ρ_e the mass density of the electron gas. The rate of increase of electron mass in the control volume is equal to the net inflow through conservation plus the source term. Thus, [56]

$$\frac{\partial}{\partial t}(\rho_e A) + \frac{\partial}{\partial x}(\rho_e u A) = \dot{\rho}_e A$$

For steady flow $\frac{\partial}{\partial t}(\rho_e A) = 0$ and therefore

$$\frac{\partial}{\partial x}(\rho_e u A) = \dot{\rho}_e A$$

Dividing through by the electron mass, m_e, one obtains

$$\frac{\partial}{\partial x}(n_e u A) = A \frac{dn_e}{dt}$$

For steady one-dimensional flow the global continuity equation is simply[56]

$$\frac{\partial}{\partial x}(\rho u A) = 0$$

where $\rho = n_o m_i$; n_o being the total number density of heavy particles and m_i their mass.

Now define an ionization fraction: $f = n_e/n_o$. Because all the argon atoms are either singly or doubly ionized, f will in general be greater than unity. Substitution of this expression in the electron conservation equation yields:

$$\frac{1}{m_i}\frac{\partial}{\partial x}\left(f n_o m_i A u\right) = A\frac{dn_e}{dt}$$

where the left hand side has been multiplied by $\frac{m_i}{m_i} = 1$. Since $\rho = n_o m_i$, this equation becomes

$$\frac{\rho u A}{m_i}\frac{\partial f}{\partial x} + \frac{f}{m_i}\frac{\partial}{\partial x}(\rho u A) = A\frac{dn_e}{dt}$$

The second term on the left vanishes as a result of the global continuity equation. Substituting for $\frac{dn_e}{dt}$ from the recombination equation, and using the fact that $n_e = n_o f$, so that $n_{ii} = (f-1)n_o$, one obtains, finally,

$$\frac{\partial f}{\partial x} = -\beta\frac{n_o^2 f^2 (f-1)}{u\, T_e^{9/2}}$$

A change of variables, $x = \zeta x_1$, where x_1 is a location where f is known, results in:

$$\frac{\partial f}{\partial \zeta} = -\beta\frac{x_1 n_o^2 f^2 (f-1)}{u\, T_e^{9/2}}$$

which can be integrated to yield the following expression:

$$\frac{1}{f} + \ln\left(\frac{f-1}{f}\right) = -\beta x_1 \int_1^\zeta \frac{n_o^2}{u\, T_e^{9/2}}\, d\zeta + K_1$$

where $K_1 = \frac{1}{f_1} + \ln\left(\frac{f_1 - 1}{f_1}\right)$ and f_1 is evaluated at $\xi = 1$.

The axial profiles of n_e, T_e and u are available from the experiments, and the right hand side of this equation can be integrated numerically. However, for the purposes at hand it is more convenient to approximate the experimental curves by simple power laws, i.e:

$$n_o = n_{o1}\,\xi^a$$

$$u = u_1\,\xi^b$$

$$T_e = T_{e1}\,\xi^c$$

Upon substitution of these relations in the equation above, and integration of the right hand side, the following result is obtained:

$$\frac{1}{f} + \ln\left(\frac{f-1}{f}\right) = \frac{C_1}{s+1}\left(\xi^{s+1} - 1\right) + K_1 \quad, \quad s \neq -1$$

where

$$C_1 = -\,8.75 \times 10^{-27}\,Z^3\,\frac{n_{o1}^2\,\chi_1}{u_1\,T_{e1}^{9/2}}$$

and

$$s = 2a - b - \frac{9}{2}c$$

This equation for f is transcendental and must be solved graphically.

The experimentally determined flow velocity profile in the argon jets, shown in Fig. 4-18 can be approximated reasonably well by $u \sim x^{\frac{1}{2}}$ in the interval from $x = 5$ cm to $x = 15$ cm, where the bulk of the acceleration outside the chamber occurs. Thus in $u = u_1\xi^b$, b takes on the value 1/2. It has already been argued that $T_e \sim x^{-\frac{1}{2}}$ is a good representation of the electron temperature profile; thus in $T_e = T_{e1}\xi^c$, c takes on the value $-1/2$. The profile of heavy particle density n_o presents more difficulties. The contours of n_e in Fig. 5-2, from which n_o can be estimated, are not very accurate downstream of $x = 5$ cm, and, actually, no contours exist for locations in the argon jet beyond

about x = 10 cm. In the interval $5 < x < 10$ cm it appears that $n_e \sim x^{-1}$, which is unusual, considering that the lateral dimensions of the argon jets appear to increase linearly with x and the velocity increases as $x^{\frac{1}{2}}$. Based on the continuity equation one would expect $n_e \sim x^{-2\frac{1}{2}}$, not accounting for recombination. The same behaviour is expected of the heavy particle number density, n_o, _i.e_: $n_o \sim x^{-2\frac{1}{2}}$, although no assumptions about recombination need be made in this case. These contradictory indications for the functional relationship between n_e and x are likely a result of large experimental errors in the electron density contours downstream of x = 5 cm. In the present case it will be assumed that $n_o \sim x^{-2\frac{1}{2}}$ is the correct functional dependence for $5 < x < 15$ cm and consequently the value of a in $n_o = n_{o1} \xi^a$ takes on the value $-2\frac{1}{2}$. Hence, $s = 2a - b - \frac{9}{2} c = -3.25$.

The conditions at $\xi = 1$ (x = 5 cm) are:

$$n_{o1} = 1.45 \times 10^{15} \text{ cm}^{-3}$$
$$u_1 = 8.5 \times 10^5 \text{ cm/sec}$$
$$T_{e1} = 1.7 \text{ eV}$$
$$Z = 2$$
$$n_e = 2.2 \times 10^{15} \text{ cm}^{-3}$$
$$f_1 = 1.54$$

Thus,

$$\frac{1}{f} + \ln\left(\frac{f-1}{f}\right) = 3.1 \times 10^{-2} \left(\xi^{-2.25} - 1 \right) - 0.40$$

The graphical solution for $\xi = 3$ (x = 15 cm) yields f = 1.5 . The fraction (f-1) of second ions thus drops from 0.54 at x = 5 cm to 0.50 at x = 15 cm. In other words about 7% of the second ions recombine in this axial interval. If the entire energy of recombination were recovered as random thermal energy and subsequently as streaming energy, only about 1 eV per heavy particle would be recovered - an insignificant amount. Actually under the conditions prevalent in the exhaust plume, more than half the recombination energy

would be lost in radiation, as can be ascertained through calculations similar to those of Fraser et al.[73] (It is interesting to note here that because of the dependence of the recombination coefficient on the cube of the ionic charge, the predicted recombination rate of AII to AI is nearly an order of magnitude less than that of AIII to AII, which is consistent with the spectroscopic observations.)

As a check on the sensitivity of the recombination calculations on the exact profiles of electron temperature and heavy particle density, two other sample cases were considered. In the first case the total ion density was assumed to have the profile used previously ($n_o \sim x^{-2\frac{1}{2}}$), while the electron temperature was assumed to have the following form: $T_e \sim x^{-1}$, but with T_e still equal to T_i at $x = 5$ cm. In the second case the $T_e \sim x^{-\frac{1}{2}}$ profile was retained, while the heavy particle density was taken to have the form $n_o \sim x^{-1}$, with the same conditions at $x = 5$ cm. The calculations reveal that in the first case 14% of the second ions present at $x = 5$ cm recombine downstream, while in the second case 25% of the second ions recombine. The energy recovered in either case is, however, not very significant because more than half the available recombination energy is lost in radiation.

REFERENCES

1. Jahn, R. G., _Physics of Electric Propulsion_, McGraw-Hill Book Co., New York, 1968.

2. Nerheim, N. M. and Kelly, A. J., "A Critical Review of the Magnetoplasmadynamic (MPD) Thruster for Space Applications," NASA Technical Report 32-1196, Jet Propulsion Laboratory, California Institute of Technology, Pasadena, Calif., Feb. 1968.

3. Clark, K. E. and Jahn, R. G., "The Magnetoplasmadynamic Arcjet," _Astronautica Acta_, Vol. 13, pp. 315-325, Pergamon Press, Ltd., 1967.

4. Clark, K. E., "Quasi-Steady Plasma Acceleration," Ph.D. Thesis, Aerospace and Mechanical Sciences Report 859, Princeton University, Princeton, N. J., May 1969.

5. Clark, K. E. and Jahn, R. G., "Quasi-Steady Plasma Acceleration," _AIAA Journal_, Vol. 8, No. 2, Feb. 1970, pp. 216-220.

6. Oberth, R. C., "Anode Phenomena in High Current Discharges," Ph.D. Thesis, Aerospace and Mechanical Sciences Report 961, Princeton University, Princeton, N. J., December 1970.

7. Oberth, R. C. and Jahn, R. G., "Anode Phenomena in High Current Accelerators," _AIAA Journal_, Vol. 10, No. 1, Jan. 1972, pp. 86-91.

8. Turchi, P. J., "The Cathode Region of a Quasi-Steady MPD Arcjet," Ph.D. Thesis, Aerospace and Mechanical Sciences Report 940, Princeton University, Princeton, N. J., September 1970.

9. Turchi, P. J., and Jahn, R. G., "Cathode Region of a Quasi-Steady MPD Arc Jet," _AIAA Journal_, Vol. 9, No. 7, July 1971, pp. 1372-1379.

10. Cory, J. S., "Mass, Momentum and Energy Flow from an MPD Accelerator," Ph.D. Thesis, Aerospace and Mechanical Sciences Report 999, Princeton, University, Princeton, N. J., September 1971.

11. Jahn, R. G., et al., "Acceleration Patterns in Quasi-Steady MPD Arcs," _AIAA Journal_, Vol. 9, No. 1, Jan. 1971, pp. 167-172.

12. Malliaris, A. C. and John, R. R., "Outstanding Problems Regarding the Feasibility of a Repetitively Pulsed MPD Propulsion System," AIAA Paper No. 70-1093, 8th Electric Propulsion Conference, Stanford, Calif., Aug.-Sept. 1970.

13. Di Capua, M. S., "Energy Deposition in Parallel-Plate Plasma Accelerators," Ph.D. Thesis, Aerospace and Mechanical Sciences Report 1015, Princeton University, Princeton, N. J., December 1971.

14. Spitzer, L., Physics of Fully Ionized Gases, Interscience Publishers, New York, 1962.

15. Clark, K. E., et al., "Quasi-Steady Magnetoplasmadynamic Arc Characteristics," AIAA Paper 70-1095, 8th Electric Propulsion Conference, Stanford, Calif., Aug.-Sept. 1970.

16. Bohn, W. L., et al., "On Spectroscopic Measurements of Velocity Profiles and Non-Equilibrium Radial Temperatures in an Argon Plasma Jet," J. Quant. Spectrosc. Radiat. Transfer, Vol. 7, 1967, pp. 661-676.

17. Jahn, R. G. et al., "Pulsed Electromagnetic Gas Acceleration," NASA NGL 31-001-005, Aerospace and Mechanical Sciences Report 634q, Princeton University, Princeton, N. J., July 1971.

18. Jahn, R. G. et al., "Pulsed Electromagnetic Gas Acceleration," NASA HGL 31-001-005, Aerospace and Mechanical Sciences Report 634p, Princeton University, Princeton, N. J., Jan. 1971.

19. Jahn, R. G., et al., "Gas Triggered Pinch Discharge Switch," Rev. Sci. Instr., Vol. 34, No. 12, 1963, pp. 1439-1440.

20. Jahn, R. G. and Clark, K. E., "A Large Dielectric Vacuum Facility," AIAA Journal, Vol. 4, No. 6, 1966, p. 1135.

21. von Jaskowsky, W., Department of Aerospace and Mechanical Sciences, Princeton University, Princeton, N. J., private communication, 1972.

22. Hixon, T. L. and von Jaskowsky, W., Department of Aerospace and Mechanical Sciences, Princeton University, Princeton, N. J., private communication, 1972.

23. Madorsky, S. L., Thermal Degradation of Organic Polymers, Interscience Publishers, New York, 1964.

24. Born, M. and Wolf, E., *Principles of Optics*, Pergamon Press, 1970.

25. Griem, H. R., *Plasma Spectroscopy*, McGraw-Hill Book Co., New York, 1964.

26. McWhirter, R. W. P., "Spectral Intensities," in *Plasma Diagnostic Techniques*, R. H. Huddlestone and S. L. Leonard, eds., Academic Press, New York, 1965.

27. *M.I.T. Wavelength Tables*, The Technology Press, John Wiley and Sons, Inc., New York, 1939.

28. Jahn, R. G. et al., "Pulsed Electromagnetic Gas Acceleration," NGL 31-001-005, Aerospace and Mechanical Sciences Report 634r, Princeton University, Princeton, N. J., Jan. 1972.

29. Fried, B. D. et al., "Ion Acoustic Waves in a Multi-Ion Plasma," *Phys. Fluids*, Vol. 14, No. 11, Nov. 1971, pp. 2388-2392.

30. Malliaris, A. C. et al., "Quasi-Steady MPD Propulsion at High Power," Final Technical Report AVSD-0146-71-RR, NASA CR111872, Feb. 1971.

31. Beth, M.-U. and Kling, M. G., "Spectroscopically Measured Velocity Profiles of an MPD Arc Jet," *AIAA Journal*, Vol. 7, No. 11, Nov. 1969, pp. 2181-2182.

32. Sovie, R. J. and Connolly, D. J., "A Study of the Axial Velocities in an Ammonia MPD Thruster," AIAA Journal, Vol. 7, No. 4, April 1969, pp. 723-725.

33. Sovie, R. J. and Connoly, D. J., "Effect of Background Pressure on Magnetoplasmadynamic Thruster Operation," *J. Spacecraft*, Vol. 7, No. 3, March 1970, pp. 255-258.

34. Malliaris, A. C. and Libby, D. R., "Velocities of Neutral and Ionic Species in an MPD Flow," AIAA Paper No. 69-109, 7th Aerospace Sciences Meeting, New York, N. Y., Jan. 20-22, 1969.

35. Malliaris, A. C. and Libby, D. R., "Spectroscopic Study of Ion-Neutral Coupling in Plasma Acceleration," *AIAA Journal*, Vol. 9, No. 1, Jan. 1971, pp. 160-167.

36. Connolly, D. J. and Sovie, R. J., "Comment on 'Spectroscopic Study of Ion-Neutral Coupling in Plasma Acceleration'," *AIAA Journal*, Vol. 9, No. 9, Sept. 1971, pp. 1885-1886.

37. Kogelschatz,U., "Doppler-Shift Measurements of Axial and Rotational Velocities in an MPD Arc," *AIAA Journal*, Vol. 8, No. 1, Jan. 1970, pp. 150-154.

38. Freeman, M. P. and Katz, S., "Determination of the Radial Distribution of Brightness in a Cylindrical Luminous Medium with Self-Absorption," *J. Opt. Soc. Am.*, Vol. 50, No. 8, Aug. 1960, pp. 826-830.

39. Feynman, R. P. et al., *The Feynman Lectures on Physics*, Addison-Wesley Publishing Co., Inc., 1963.

40. Wiese, W. L., "Line Broadening," in *Plasma Diagnostic Techniques*, R. H.Huddlestone and S. L. Leonard, eds., Academic Press, New York, 1965.

41. Meissner, K. W., "Interference Spectroscopy," *J. Opt. Soc. Am.*, Vol. 31, No. 6, June 1941, pp. 405-427.

42. Jacquinot, P., "New Developments in Interference Spectroscopy," *Reports on Progress in Physics*, Vol. XXII, 1960, pp. 267-312.

43. Chabbal, R., "Finesse Limite d'un Fabry-Perot Formé de Lames Imparfaites," *Le Journal de Physique et le Radium*, Vol. 19, March 1958, pp. 295-300.

44. Cooper, J. and Greig, J. R., "Rapid Scanning of Spectral Line Profiles Using an Oscillating Fabry-Perot Interferometer," *J. Sci. Instrum.*, Vol. 40, 1963, pp. 433-437.

45. Greig, J. R. and Cooper, J., "Rapid Scanning with the Fabry-Perot Etalon," *Applied Optics*, Vol.7, No. 11, Nov. 1968, pp. 2166-2170.

46. Houben, M., Perkin-Elmer Corp., private communication, Jan. 1971.

47. Vincenti, W. G. and Kruger, C. H., *Introduction to Physical Gas Dynamics*, John Wiley and Sons, Inc., New York, 1965.

48. Thonemann, P. C., "The Measurement of Ultra-High Temperatures," in *Optical Spectrometric Measurements of High Temperatures*, P. J. Dickerman, ed., University of Chicago Press, 1961.

49. Kaufman, A. S., "Analysis of the Velocity Field in Plasmas from the Doppler Broadening of Spectral Emission Lines," in Advances in Atomic and Molecular Physics, Vol. 6, D. R. Bates and I. Esterman, eds., Academic Press, New York, 1970.

50. Roberts, D. E., "Measurement of the Stark Broadening Parameters of Several AII Lines," J. Phys. B (Proc. Phys. Soc.), Ser. 2, Vol. 1, 1968, pp. 53-61.

51. van de Hulst, H. C. and Reesinck, J. J. M., "Line Breadths and Voigt Profiles," Astrophys. Journal, Vol. 106, 1947, pp. 121-127.

52. Tudor Davies, J. and Vaughan, J. M., "A New Tabulation of the Voigt Profile," Astrophys. Journal, Vol. 4, May 15, 1963, pp. 1302-1305.

53. Boyle, M. J., Department of Aerospace and Mechanical Sciences, Princeton University, private communication, 1972.

54. Chou, Y. S. and Talbot, L., "Source Flow Expansion of a Partially Ionized Gas into a Vacuum," AIAA Journal, Vol. 5, No. 12, pp. 2166-2172.

55. Drellishak, K. S., et al., "Tables of Thermodynamic Properties of Argon, Nitrogen, and Oxygen Plasmas," AEDC-TDR-64-12, Arnold Engineering Development Center, Air Force Systems Command, USAF, Jan. 1964.

56. Liepmann, H. W. and Roshko, A., Elements of Gasdynamics, John Wiley and Sons, Inc., New York, 1957.

57. D'Angelo, N., "Recombination of Ions and Electrons," Phys. Rev., Vol. 121, No. 2, Jan. 15, 1961, pp. 505-507.

58. D'Angelo, N., "Ion-Electron Recombination," Phys. Rev., Vol. 140, No. 5A, Nov. 29, 1965.

59. Hinnov, E. and Hirschberg, J. G., "Electron-Ion Recombination in Dense Plasmas," Phys. Rev., Vol. 125, No. 3, Feb. 1, 1962, pp. 795-801.

60. Bates, D. R. et al., "Recombination Between Electrons and Atomic Ions, I. Optically Thin Plasmas," Proc. Roy. Soc. (London), Vol. A267, May 1962, pp. 297-312.

61. Bates, D. R. et al., "Recombination of Electrons and Atomic Ions, II. Optically Thick Plasmas," Proc. Roy. Soc. (London), Vol. A270, Nov. 1962, pp. 155-167.

62. Bates, D. R. and Kingston, A. E., "Recombination and Energy Balance in a Decaying Plasma, I. H-H$^+$-e Plasma, II. He-He$^+$-e Plasma," Proc. Roy. Soc. (London), Vol. A279, 1964, pp. 10-38.

63. Byron, S. et al., "Electron-Ion Recombination by Collisional and Radiative Processes," Phys. Rev. Lett. Vol. 8, No. 9, May 1, 1962, pp. 376-379.

64. Robben, F. et al., "Spectroscopic Study of Electron Recombination with Monatomic Ions in a Helium Plasma," Phys. Rev., Vol. 132, No. 6, Dec. 15, 1963, pp. 2363-2371.

65. Gurevich, A. V. and Pitaevskii, L. P., "Recombination Coefficient in a Dense Low-Temperature Plasma," Soviet Phys. JETP, Vol. 19, No. 4, Oct. 1964, pp. 870-871.

66. Cooper, W. S. and Kunkel, W. B., "Recombination of Ions and Electrons in a Highly Ionized Hydrogen Plasma," Phys. Rev., Vol. 138, No. 4A, May 17, 1965, pp. A1022-A1027.

67. Hinnov, E., "Measurement of Recombination-Rate Coefficient of He^{++}," Phys. Rev., Vol. 147, No. 1, July 8, 1966, pp. 197-200.

68. Chen, C. J., "Partition of Recombination Energy in the Decaying Rare-Gas Plasmas," Phys. Rev., Vol. 163, No. 1, Nov. 5, 1967, pp. 1-7.

69. Zel'dovich, Ya.B. and Raizer, Yu.P., Physics of Shock Waves and High-Temperature Hydrodynamic Phenomena, Vol. I & II, Academic Press, New York, 1966.

70. Bray, K.N.C., "Electron-Ion Recombination in Argon Flowing Through a Supersonic Nozzle," in The High Temperature Aspects of Hypersonic Flow, W. C. Nelson, ed., AGARD-NATO, The Macmillan Co., New York, 1964.

71. Talbot, L. et al., "Expansion of a Partially-Ionized Gas Through a Supersonic Nozzle," Report No. AS-65-14, Institute of Engineering Research, University of California, Berkeley, California, Aug. 1965.

72. Bowen, S. W. and Park, C., "Computer Study of Nonequilibrium Excitation in Recombining Nitrogen Plasma Nozzle Flows," AIAA Journal, Vol. 9, No. 3, March, 1971, pp. 493-499.

73. Fraser, R. B. et al., "Flow Properties of a Partially Ionized Free Jet Expansion," Phys. Fluids, Vol. 14, No. 11, Nov. 1971, pp. 2317-2327.

74. Clark, K. E., Department of Aerospace and Mechanical Sciences, Princeton University, Princeton, N. J., private communication, 1972.

75. Pai, S. I., Fluid Dynamics of Jets, D. van Nostrand Co., Inc., New York, 1954.

76. Keck, J., "Current Speed in a Magnetic Annular Shock Tube," Phys. Fluids, Vol. 7, No. 11, Nov. 1964 (Supplement), pp. S16-S27.

77. Colgate, S. A., "Initial Conditions for the Dynamic Pinch," UCRL-4895, University of California, Radiation Laboratory, Livermore, Calif., May 1957.

78. Ashby, D.E.T.F., "A Simple Theory of Wall Evaporation in a Pulsed Gas Discharge," Plasma Physics (Journal of Nuclear Energy, Part C), Vol. 5, 1963, pp. 83-87.

79. Workman, J. B., "Insulator Ablation in Magnetic Piston Shock Tubes," Phys. Fluids, Vol. 8, No. 12, Dec. 1965, pp. 2162-2168.

80. Lie, T. N. et al., "Diagnostics of Accelerating Plasmas," NASA NGR-09-005-025, Report No. 68-005, Department of Space Science and Applied Physics, The Catholic University of America, Washington, D. C., March 1968.

81. Villani, D. D., Department of Aerospace and Mechanical Sciences, Princeton University, Princeton, N. J., private communication, 1972.

82. Carslaw, H. S. and Jaeger, J. C., Conduction of Heat in Solids, Oxford University Press, London, 1959.

83. Tkachenko, E. V. et al., "Linear Pyrolysis of Polymethyl Methacrylate," Combustion Explosion and Shock Waves, Vol. 5, No. 1, 1969, pp. 11-16

84. Fineman, S., "Some Analytical Considerations of the Hybrid Rocket Combustion Problem," MSE Thesis, Department of Aerospace and Mechanical Sciences, Princeton University, Princeton, N. J., 1962.